MOLTEN-SALT SYNTHESIZED PYROCHLORE NANOPARTICLES FOR MULTIFUNCTIONAL APPLICATIONS

A Thesis

by

JOSE P. ZUNIGA

Submitted to the Graduate College of
The University of Texas Rio Grande Valley
In partial fulfillment of the requirements for the degree of

MASTER OF SCIENCE

May 2019

Major Subject: Chemistry

MOLTEN-SALT SYNTHESIZED PYROCHLORE NANOPARTICLES FOR MULTIFUNCTIONAL APPLICATIONS

A Thesis
by
JOSE P. ZUNIGA

COMMITTEE MEMBERS

Dr. Yuanbing Mao
Chair of Committee

Dr. Karen Martirosyan
Committee Member

Dr. Tulay Atesin
Committee Member

Dr. Javier Macossay Torres
Committee Member

May 2019

ABSTRACT

Zuniga, Jose P., Molten-Salt Synthesized Pyrochlore Nanoparticles for Multifunctional Applications. Master of Science (MS), May, 2019,152 pp., 14 tables, 64 figures, references, 204 titles.

There is a need in the scientific world to design and develop high quality nanomaterials with multifunctional applications. In this work, we explore the molten-salt method (MSS) as a new green method for the synthesis of complex metal oxides. We adjusted all synthesis parameters such as time, temperature and pH to generate an optimum $La_2Hf_2O_7$ nanoparticle with a well define shape and surface. Activator ions such as Eu^{3+}, Tb^{3+}, Dy^{3+}, Bi^{3+} and uranium ion (U^{4+}, U^{6+}) were used to monitor its structural and optical behavior effect when doped.

Our results showed effective quantum yield, thermal, pressure stability, near to white light color coordinate as determined by the International Commission on Illumination (CIE) with low color coordinate temperature (CCT) for white light emitting diode (WLEDs) applications. In addition, we explore the effectiveness of our material as a scintillator for radiation detection, bio-imaging and as a nuclear waste host. All results indicate that our host material shows potential as an efficient multifunctional nanomaterial for a wide range of applications.

DEDICATION

This thesis dissertation is dedicated to my whole family and friends. My wife Magda and my daughter Alexa for all the emotional support and for being my motivation to better myself in life. I love both immensely and I don't know in what dark place I'll be if it wasn't for the love and encouragement you provide to me. Magda, I'm extremely grateful for you being in my life and filling me with all your compassion, beauty and perfection. I love you with all my soul and I'm looking forward to spending the rest of my life with you.

To my mother, thank you for providing with the strength to keep going no matter how hard a task might be. For all your understanding and love you give me as your son. Thank you, mother for believing in me even when I was at my worst. Thank you for raising me and teaching me how the world works. I love you mom.

To my friend and mentor Dr. Santosh K. Gupta, for teaching me the right path in my career and mentoring me. Thank you for all your patience and for having my back at several occasions. You have become part of my family in a very short time and the trust that we have for each other is something that I will treasure for a lifetime. Thank you for teaching how things work. Thank you for having faith in me even at times I didn't have faith in myself.

It because of all this amazing people I stand here today and for this reason I have dedicated this work to them in Honor of what they have done for me and how they impact my life. "A dream without a goal is just a wish" - Antoine de Saint-Exupéry

ACKNOWLEDGEMENTS

I will always be grateful to Dr. Yuanbing Mao, the chair of my dissertation committee for guiding and mentoring me throughout my career as a master student. Thank you for always pushing me to do more and for all your understanding and patience. Thank you to all the MAO group for all the support and encouragement.

The author thanks the financial support by the National Science Foundation under CHE (award #1710160) and DMR (grant #1523577) and the USDA National Institute of Food and Agriculture (award #2015-38422-24059, for the Integrating Food Science/Engineering and Education Network (IFSEEN) program). The Department of Chemistry at the University of Texas Rio Grande Valley is grateful for the generous support provided by a Departmental Grant from the Robert A. Welch Foundation (Grant No. BX-0048).

TABLE OF CONTENTS

Page

LIST OF TABLES

Page

LIST OF FIGURES

Page

CHAPTER I

PYROCHLORE AND DEFECT FLOURITE PHASE NANOMATERIAL

1.1.1 $A_2B_2O_7$ Structure as Nanomaterial:

Materials with $A_2B_2O_7$-type composition fall into a special class of structure called pyrochlore where A represents a trivalent rare earth (RE) ion and B represents a tetravalent transition metal ion such as Sn^{4+}, Ti^{4+}, Zr^{4+}, and Hf^{4+}. Recently, they have gained a significant interest as ceramics due to their unique properties such as high radiation stability, ability to accommodate actinides and lanthanides at both A^{III} and B^{IV} sites,(Gupta et al. 2017b) and ability to dissipate excess radiation energy by forming anti-site defects, etc. For the same reason, they have been used for immobilization of high level nuclear waste.(Martel et al. 2017) Other than nuclear energy applications, these materials have also found to be an excellent host for lanthanide doped phosphor materials because of their other favorable properties, such as suitable refractive index value, high chemical and thermal stability, wide band gap, etc.(Gupta et al. 2016b, Pokhrel et al. 2016c, Zhang et al. 2016) In addition, due to their high chemical stability, high catalytic activity, high melting point, and excellent oxide ion conductivity,(Renju et al. 2017) they have innumerable applications in many other scientific and technologic areas, such as magnetic materials,(Nguyen et al. 2017) gas sensors,(Zhong et al. 2017) catalysts,(Kim et al. 2017a) solid oxide fuel cells,(Sun and Huang 2017) lithium ion batteries,(Ali et al. 2017) structural materials in fusion reactors,(Lu et al. 2017a) etc. In addition, $A_2B_2O_7$ pyrochlore nanocrystals possess excellent luminescent properties, including intense photoluminescence in the infrared region, efficient pump-power dependence light emission, and excellent

cathodoluminescence.(Mao et al. 2009b).

Structurally, $A_2B_2O_7$ type compounds belong to the fluorite-pyrochlore phase family.(Wang et al. 2014a) Preference for either phase is contingent on the ionic radius of the RE^{3+} ion in the A-site and the B^{4+} ion in the B-site. The fluorite structure is favorable if the ionic radii of A^{3+} and B^{4+} ions are similar ($r_A/r_B < 1.46$). The oxygen vacancies are randomly distributed on the anion sites. The similar ionic radii of the A^{3+} and B^{4+} cations gives them the capability to swap sites in the lattice, which leads to anti-site defects.(Wang et al. 2014a) On the other hand, the pyrochlore structure has D_{3d} symmetry and differs from the fluorite in that it has a more ordered structure, which causes the cations to prefer the site most suitable for their size. The A^{3+} ions have an 8-fold coordination with oxygen and the B^{4+} ions have 6-fold coordination with oxygen. The anion Wyckoff sites (8b and 48f) are entirely occupied.

Among pyrochlores, $La_2Hf_2O_7$ stands out with unique properties such as high density, high refractive index, wide band gap, high thermal/chemical stability, which are very important from a technical perspective. It has been envisaged to be very good dielectric material because of its rather low defect densities and less Fermi level pinning than HfO_2.(Qi et al. 2011) Also, because of its high stopping power for X- and γ-rays with $Z_{Hf} = 72$ and its high density of 7.9 g/cm^3, it was found to be very attractive for novel high-energy radiation detectors.(Wahid et al. 2017a) $La_2Hf_2O_7$ is also known to exhibits defects induced luminescence on irradiation with ultraviolet photons, and the oxygen vacancies were found to be the most probable reason for the recombination centers in their photoluminescence process.(Eagleman et al. 2013)

Doped $RE_2Hf_2O_7$ nanoceramics with metal ions has proven to be a very successful way for tailoring their electrical,(Cepeda-Sánchez et al. 2015) optical,(Du 2015a, Papan et al. 2016) nuclear,(Whittle et al. 2009) order-disorder phenomenon,(Kong et al. 2015) scintillation,(Eagleman et al. 2012b) etc. Our group recently have done some work on photo- and radio-luminescence of the $La_2Hf_2O_7:Eu^{3+}$ nanoparticles (NPs) Figure 1.1.(Pokhrel et al. 2016c, Wahid et al. 2017a)

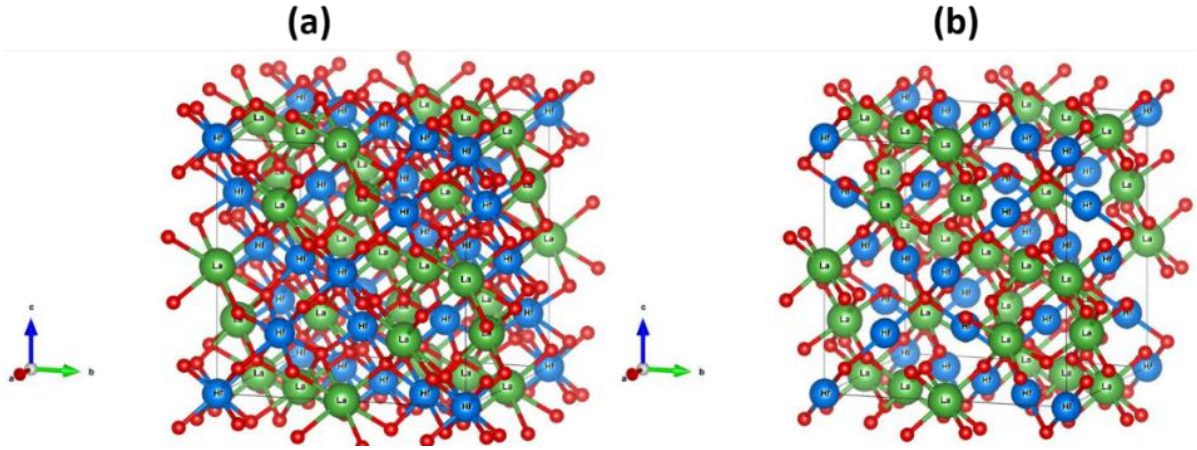

Figure 1.1: (a) Crystal structures of the (a) LHO and (b) LHOE NPs.

1.1.2 Manipulation of Particle Parameters:

Synthesis methods have great influence on the properties of materials, especially the optical performance of luminescent NPs.(Vecht et al. 1999) The changes could be triggered by precursor selection, modification of reaction conditions, and post-synthesis processing, etc.(Gupta et al. 2016j, Gupta et al. 2016l, Wang et al. 2007a, Jung et al. 2005, Shea et al. 1998, Shea et al. 1996) For example, increase of synthesis time or temperature could lower surface defect density and luminescence quenching, and so enhance quantum yield of luminescent NPs, however, it also could induce undesirable particle growth and agglomeration, which may scatter excitation/emission light, and eventually compromise the overall performance of luminescent NPs.(Wang et al. 2007c) There are various ways to induce change in particle size of nanophasic

materials, such as changing pH value of precursor solution, varying annealing temperature, altering synthesis duration, differing reaction kinetics, and modifying thermodynamics of reactions, etc. The changes of synthesis duration and temperature may indirectly affect obtained particle size, crystallinity, coordination number, and geometry around dopant ions in an inorganic phosphor. This also leads to change in type, size and density of defects. It was reported that synthesis temperature and duration have profound effects on size, morphology, defects density and surface energy of obtained products,(Gupta et al. 2016j, Gupta et al. 2016m, Gupta et al. 2017e) which ultimately alter the optical properties of nanomaterials. Melato and the group investigated the effect of annealing time on the structure, morphology and photoluminescent properties of $MgAl_2O_4:In^{3+}$ nanophosphor.(Melato et al. 2017) On the other hand, Motloung et al. investigated the effects of the annealing time on the optical properties of $ZnAl_2O_4$.(Motloung et al. 2018b) There are a few more reports on the effect of annealing time on optical properties of $YAG:Ce^{3+}$ and $ZnAl_2O_4:Cr^{3+}$, etc.(Abd et al. 2018, Menon et al. 2017, Motloung et al. 2018a)

In materials science, thermal annealing is a heat treatment that alters the physical and sometimes chemical properties of a material such as intrinsic stress liberation, structural improving, and surface roughness control. In annealing, atoms migrate in the crystal lattice, surface morphology modifies, and the number of dislocations decreases, leading to property change of materials, so further heat treatments of various materials with temperature and time have been used to achieve desirable properties. Thermal annealing is also known to have significant influence on the luminescence properties of europium ion doped nanophosphor materials. Exposing nanophosphors to different annealing temperatures and durations may leads to change in size of NPs, can affect the crystallinity of the samples, and the coordination number and geometry around dopant Eu^{3+} ion. Such changes may affect the type and density of defect in

the nanomaterials. Structural changes induced by annealing temperature was also studied using X-ray diffraction (XRD), Raman spectroscopy, Fourier transformed infrared spectroscopy (FTIR) and Brunauer–Emmett–Teller (BET) surface area.

1.1.3 Importance of Photoluminescence to Probe Structural Change:

The luminescence in doped samples is governed by energy transfer process (ETP) from host to dopant ion. Understanding the dynamics of ETP in doped phosphors sometime become so imperative in designing a tunable phosphor. Lanthanide based luminescent nanomaterials exhibit unique properties such as narrow emission, high color purity, millisecond lifetime, and large Stoke shift, which make them favorable for various applications such as biological imaging,(Cho et al. 2018) optical sensors,(Mehlenbacher et al. 2017) high power LEDs,(Kim et al. 2017b) anti-counterfeiting,(Han et al. 2016) memory devices,(Zhou et al. 2014b) photovoltaic cells,(Kumar et al. 2017) etc. Exploiting the luminescence probe that is sensitive to the local structure is expected to give useful information on its local site, site symmetry and distribution ratio at A^{3+} and B^{4+} sites in $A_2B_2O_7$ type compounds, which are very important for designing efficient opto-electronic devices. 4f electron exhibits special photophysical characteristics compared to 3d and 5f electrons, and therefore exploring nanomaterials doped with luminescent lanthanide ions has been found to be an indispensable approach for designing high quality nanophosphors for future applications. Once doped with Ln^{3+} ion, NPs exhibit photophysical properties that are different from their bulk counterparts due to their small grains. Meltzer et al. reported increased photoluminescence efficiency in nanophasic materials compared to their bulk counterparts.(Meltzer et al. 1999)

1.1.4 Importance of Europium Ion as a Dopant:

Europium ion is one of the most efficient red emitting ions, which are often used commercially in light emitting diodes for solid-state lighting. It is also one of the most frequently used dopant ion as a spectroscopic probe for studying the roles of charge compensator,(Gupta et al. 2018b) local structure,(Gupta et al. 2016f, Gupta et al. 2013, Mani et al. 2018) host-dopant energy transfer dynamics,(Gupta et al. 2016e, Gupta et al. 2013, Gupta et al. 2015b) point group symmetry,(Gupta et al. 2016a, Gupta et al. 2016c, Gupta et al. 2016h, Gupta et al. 2015b, Gupta et al. 2018b) low temperature luminescence dynamics,(Gupta et al. 2016n) thermal effect,(Gupta et al. 2016j) etc. Its color output in various hosts can be tuned by optimizing the synthesis method, co-doping, host-sensitized energy transfer, dopant concentration, annealing time, and annealing temperature, etc.(Wang et al. 2017a) In terms of the optical properties of transition metal and lanthanide ion doped $La_2Hf_2O_7$, there are several research groups including ours where luminescence and scintillation properties are explored.(Eagleman et al. 2012a, Ji et al. 2005c, Pokhrel et al. 2016a, Wahid et al. 2017a, Wang et al. 2017c, Ji et al. 2005b, Yanagida and Okada 2016, Du 2015b) It is well documented that Eu^{3+} ions make an ideal spectroscopic probe for lanthanide sites due to its distinct spectroscopic signature, integer J-numbers, and the ease of assessing its site symmetry. Its ground state $^7F_0$ and the most informative excited state $^5D_0$ are non-degenerate. Therefore, they are not splitted by crystal-field effects.(Gupta et al. 2016d, Phatak et al. 2017) Eu^{3+} ions with the characteristic orange red emissions at 592 nm and 614 nm are highly sensitive to the local surroundings.(Gupta et al. 2015a) The information deciphered from Eu^{3+} photoluminescence and spectral data can give highly reliable information on whether the dopant ions are localized on the surface of $A_2B_2O_7$ NPs or they have percolated interstitially or substitutionally inside the $A_2B_2O_7$ lattice. Although closeness in size and charge guarantees

most of the Eu^{3+} ions to occupy the A^{3+} site, there may be lattice strain to mismatch in ionic radii between 8-coordinated Eu^{3+} and RE^{3+} ions, which may affect the optical properties of Eu^{3+} ions.

1.1.5 $A_2B_2O_7$ as a Suitable Host for White Light Applications:

Rare earth ion doped oxide nanoparticles for photonics application have several advantages such as resistance to photobleaching/photoblinking, high color purity, narrow emission, large stokes shifts etc.(Singh et al. 2014). In addition, their emission wavelengths do not change much because equilibrium geometry of the ground state and excited state wavefunction is same. These properties make them excellent candidate for solid-state lighting and light emitting displays.

Moreover, oxide nanocrystals with pyrochlore structure recently displayed variety of advanced applications because of their interesting thermo and physio chemical properties. In the past the spectroscopic investigation of $La_2Hf_2O_7$ doped with such ions as Eu^{3+}, Tb^{3+}, Pr^{3+}or Ce^{3+} proved that the matrix is able to transfer the gained energy to the dopants and produce luminescence of significant intensity(Zuniga et al. 2018c, Zuniga et al. 2018a, Trojan-Piegza et al. 2014, Ji et al. 2005a, Eagleman et al. 2012c, Hirayama et al. 2008). Each of the lanthanide ion has characteristics emission depending upon their energy level diagram. The most prominent visible emitting lanthanide ions are Dy^{3+} in blue-yellow region, Eu^{3+}/Sm^{3+} in orange-red and Tb^{3+} in green region(Gupta et al. 2016g). For white light or colored phosphors, the simultaneous generation of red, green and blue (RGB) is necessary. Based on RGB analogy characteristics emission from these ions can be combined to design the white light phosphor for solid-state lighting, which has several advantages such as long lifetimes, lower-energy consumption, high luminous efficiency and environmentally friendly characteristics. However, most of the

commercial scintillators are normally a single crystal which is very difficult to grow, time consuming and require very high temperature crystallization.

1.1.6 $A_2B_2O_7$ as a Suitable Host for Scintillator Applications:

The process of scintillation is shown in Figure 1.2. It can be defined as taking a high energy photon such as X-ray and converting it to a lower energy photon in the visible region. Moreover, X-ray induced visible light emission is difficult to tune over the visible range. In this work, we have proposed a simple, low temperature processable molten salt synthesis (MSS) approach for designing lanthanide-doped pyrochlores (LDPs) based nanoscintillator and their behavior under X-ray irradiation. These nanoscintillator particles are expected to display high absorption cross section for X-ray and intense radioluminescence in the visible spectrum. Compared to bulk scintillator, these pyrochlore NPs are can exhibit tunable radioluminescence across the visible wavelengths by tailoring the dopant ions.

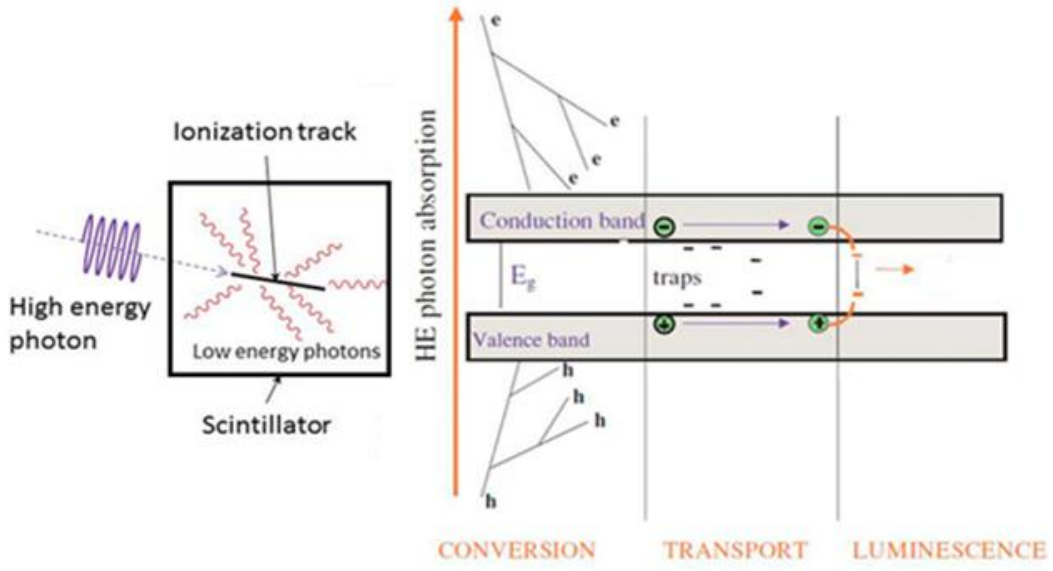

Figure 1.2: Scintillation mechanism

1.1.7 $A_2B_2O_7$ as a Suitable Host for Nuclear Waste Immobilization:

Uranium and its radioactive isotopes contribute to a high-level of nuclear waste, which needs to be properly disposed. Uranium ion has multiple oxidation states (i.e. +3, +4, +5 and +6), all of which are luminescence active with characteristics emission.(Hashem et al. 2014, Natrajan 2012, Sobczyk et al. 2008, Steudtner et al. 2006) Speciation studies of uranium ion in $A_2B_2O_7$ compounds will be highly beneficial for fundamental uranium chemistry and nuclear industry as shown in Figure 1.3. However, because of its complex nature and various existing valence states, the incorporation mechanism, oxidation state and structural environment of uranium ions in $A_2B_2O_7$ compounds are uncharted and vague. For example, Zhang and coworkers investigated the phase evolution of U doped $Y_2Ti_2O_7$ and $Gd_2Ti_2O_7$.(Zhang et al. 2017a) They have carried out detailed phase evolution investigation from $Ln_2Ti_2O_7$ pyrochlores to $Ln_{0.5}U_{0.5}Ti_2O_6$ (Ln=Y and Gd) brannerites in glasses sing various techniques such as X-ray diffraction, Raman spectroscopy, diffuse reflectance spectroscopy and electron microscopy. Shu et al. studied the effect of alpha irradiation on U doped $Gd_2Zr_2O_7$.(Shu et al. 2017) Their study revealed that main crystal structure does not changed but weaker structural ordering does takes place on alpha irradiation. They have also found increase in radiation stability of $Gd_2Zr_2O_7$ at higher uranium concentration. Lu *et al.* explored the effects of U_3O_8 on the phase and microstructure evolution of $Gd_2Zr_2O_7$ and found that that uranium is homogenously distributed in +4 and +6 oxidation state respectively at Gd^{3+} and Zr^{4+} site.(Lu et al. 2017b) One of us has studied the speciation of uranium using luminescence spectroscopy for $A_2Zr_2O_7$ (A = La, Nd and Gd) and the results shows the stabilization of uranium as U^{4+} and UO_6^{6-} in $Gd_2Zr_2O_7$, only as UO_6^{6-} in $Nd_2Zr_2O_7$ and as both UO_6^{6-} and UO_2^{2+} $La_2Zr_2O_7$.(Gupta et al. 2016i, Gupta et al. 2017c, Mohapatra et al. 2016) There are few more reports on uranium doped $Gd_2Zr_2O_7$ wherein speciation of uranium is carried

out in bulk phase using X-ray diffraction, Raman spectroscopy and X-ray photoelectron spectroscopy along with other suitable techniques.(Kutty et al. 2005, Shu et al. 2016, Zhang et al. 2014) However, none of these studies includes reports on structure and phase evolution of uranium doped $La_2Hf_2O_7$ nanoparticles (NPs).

Photoluminescence (PL) spectroscopy is the most acceptable technique for detecting and estimating uranium in ultra-trace level in both solids as well as aqueous media.(Phillips et al. 2017) Meanwhile, Therefore, through the successful development of uranium doped $La_2Hf_2O_7$ NPs and their thorough characterization of the fundamental spectra of uranium ions, doping induced phase transformation, and structure-optical property correlation, we believe this work open new research areas important for safe nuclear energy and sustainable environment.

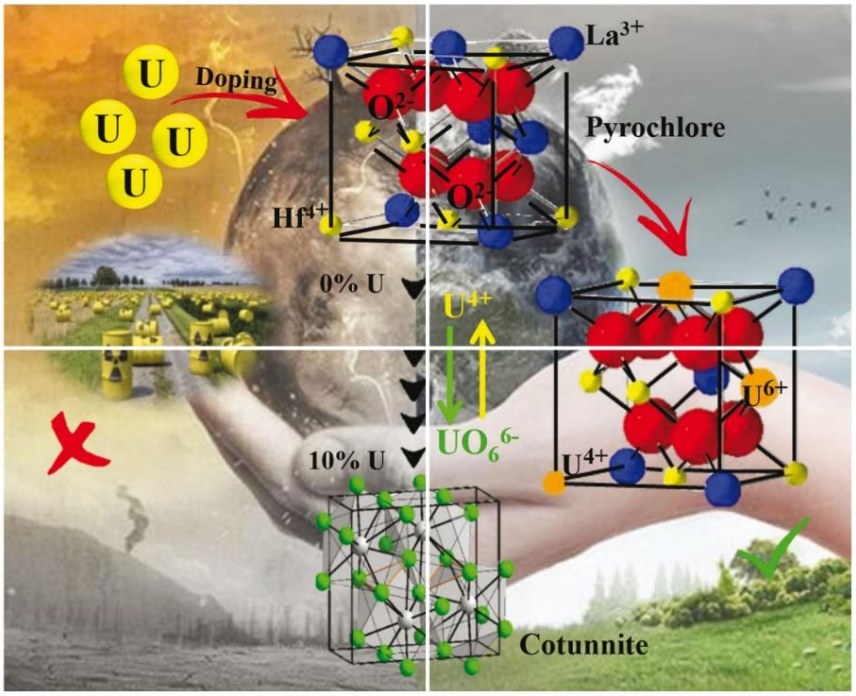

Figure 1.3: Phase transformation of Ideal pyrochlore structure with increasing concentration of uranium as a suitable host for nuclear waste immobilization applications.

CHAPTER II

DIFFERENT SYNTHESIS ROUTES FOR LUMINESCENT MATERIALS

2.1.1 Conventional Solid-state Route*:*

The solid-state reaction route is the most widely used method for the preparation of polycrystalline solids from a mixture of solid starting materials.(Im et al. 2004, Kesanli et al. 2006, Zhang et al. 2017b, Subramanian et al. 1983b, Sahu et al. 2018) Solids do not react together at room temperature over normal time scales and it is necessary to heat them to much higher temperatures, often to 1000 to 1500 °C for the reaction to occur at an appreciable rate. The factors on which the feasibility and rate of a solid-state reaction include, reaction conditions, structural properties of the reactants, surface area of the solids, their reactivity and the thermodynamic free energy change associated with the reaction. The mechanism of solid-state reactions is diffusion control; and hence, repeated grinding and repeated heating are required.

Consequences of high reaction temperatures

1. It can be difficult to incorporate ions that readily form volatile species (i.e. Ag+).
2. It is not possible to access low temperature, metastable (kinetically stabilized) products.
3. High (cation) oxidation states are often unstable at high temperature, due to the thermodynamics of the following reaction:

$2MO_n(s) + 2MO_{n-1}(s) + O_2(g)$

Due to the release of a gaseous product (O_2), the products are favored by entropy, and the entropy contribution to the free energy become increasingly important as the temperature increases.

Preparation of single-phase compound is difficult by the conventional solid-state method. Hence, doping a low concentration (of the order of 1–3%) of activator has always been delicate. Thus, the limitations of conventional solid state are:

1. Inhomogeneity of the product.

2. Formation of large particles with low surface area and hence, mechanical particle size reduction is required, which introduces impurity and defects.

3. Presence of defects, which are harmful to luminescence.

The problem of inhomogeneity could be mitigated by the use of non-conventional methods (wet-chemical). These techniques are defined as techniques which do not comprise of the normal mixing, calcinations and grinding operations. Wet-chemical methods such as sol-gel, combustion, polymeric precursor, reverse micellar etc. have been employed to synthesize rare-earth activated phosphors. These wet-chemical methods facilitate doping of rare earth activators uniformly. But calcination is required to get crystalline (required) phosphor.

2.1.2 Sol-Gel Method:

The Sol-gel method is another technique that has been used to synthesized luminescent materials.(Biswas et al. 2003, Kahouadji et al. 2017, Li et al. 2006, Yu et al. 2006, Gupta et al. 2012a) Even though, the most widely used synthetic technique for bulk metal oxides has been the solid-state method, which is based on the direct reaction of powder mixtures, these reactions

are completely controlled by the diffusion of the atomic or ionic species through the reactants and products. To bring the reaction partners sufficiently close together and to provide high mobility, these solid-state processes require high temperature and small particle sizes. Although the harsh reaction conditions only lead to thermodynamically stable phases, preventing the formation of metastable solids, these approaches gave access to many new solid compounds, enabling the development of structure-properties relationships. However, in comparison to organic chemistry, where highly sophisticated synthetic pathways are employed to make and break chemical bonds in a controlled way, the ceramic method is a rather crude approach. It is therefore no surprise that for the size- and shape-controlled synthesis of nanoparticles especially liquid-phase routes represent the most promising alternatives. In contrast to solid-state processes, but analogous to organic chemistry, "chimie douce" approaches offer the possibility to control the reaction pathways on a molecular level during the transformation of the precursor species to the final product, enabling the synthesis of nanoparticles with well-defined and uniform crystal morphologies and with superior purity and homogeneity.(Cushing et al. 2004) Among the various soft-chemistry routes, sol-gel procedures were particularly successful in the preparation of bulk metal oxides (e.g., ceramics, glasses, films and fibers)(Livage et al. 1988, Hench and West 1990), and therefore they have also been applied for nanoparticle synthesis. But despite great efforts, the number of oxidic nanoparticles obtained by sol-gel chemistry is still rather small compared to the variety of compounds obtained via powder routes. In many cases a synthesis protocol developed for a bulk metal oxide could not directly be adapted to its corresponding counterpart on the nanoscale. The reasons for this observation are manifold. Aqueous sol-gel chemistry is quite complex, on the one hand due to the high reactivity of the metal oxide precursors towards water and the double role of water as ligand and solvent, and, on

the other hand, due to the large number of reaction parameters that have to be strictly controlled (hydrolysis and condensation rate of the metal oxide precursors, pH, temperature, method of mixing, rate of oxidation, the nature and concentration of anions, ...) in order to provide good reproducibility of the synthesis protocol.(Livage et al. 1988) Another fundamental problem of aqueous sol-gel chemistry is that the as-synthesized precipitates are generally amorphous. The required post-synthetic annealing step to induce the crystallization process prevents any subtle control over crystal size and shape. For the preparation of bulk metal oxides, these limitations play only a minor role; however, in the case of nanoparticle synthesis, they constitute a major issue.

In material science, the sol-gel process is a method for producing solid materials from small molecules. The method is used for the fabrication of metal oxides, especially the oxides of silicon and titanium. The process involves conversion of monomers into a colloidal solution (sol) that acts as the precursor for an integrated network (or gel) of either discrete particles or network polymers.

In general, the precursor or starting compound is either an inorganic (no carbon) metal salt (chloride, nitrate, sulfate etc.) or a metal organic compound such as an alkoxide. Metal alkoxides are the most widely used precursors, because they react readily with water and are known for many metals. Some alkoxides, which are widely used in industry, are commercially available at low cost (Si, Ti, Al, Zr), whereas other ones are hardly available or only at very high costs (Mn, Fe, Co, Ni, Cu, Y, Nb, Ta ...).

In general, the sol-gel process consists of the following steps (Figure 2.1)(Mehrotra and Singh 1997), i) Preparation of a homogeneous solution either by dissolution of metal organic precursors in an organic solvent that is miscible with water, or by dissolution of inorganic salts in

water; ii) conversion of the homogeneous solution into a sol by treatment with a suitable reagent (generally water with or without any acid/base); iii) aging; iv) shaping; and v) thermal treatment/ sintering. The first step in a sol-gel reaction is the formation of an inorganic polymer by hydrolysis and condensation reactions, i.e., the transformation of the molecular precursor into a highly cross-linked solid. Hydrolysis leads to a sol, a dispersion of colloidal particles in a liquid, and further condensation results in a gel, an interconnected, rigid and porous inorganic network enclosing a continuous liquid phase. This transformation is called the sol-gel transition. There are two possibilities to dry the gels. Upon removal of the pore liquid under hypercritical conditions, the network does not collapse, and aerogels are produced. When the gel is dried under ambient conditions, shrinkage of the pores occurs, yielding a xerogel. One of the highly attractive features of the sol-gel process is the possibility to shape the material into any desired form such as monoliths, films, fibers, and mono-sized powders, and subsequently to convert it into a ceramic material by heat treatment.

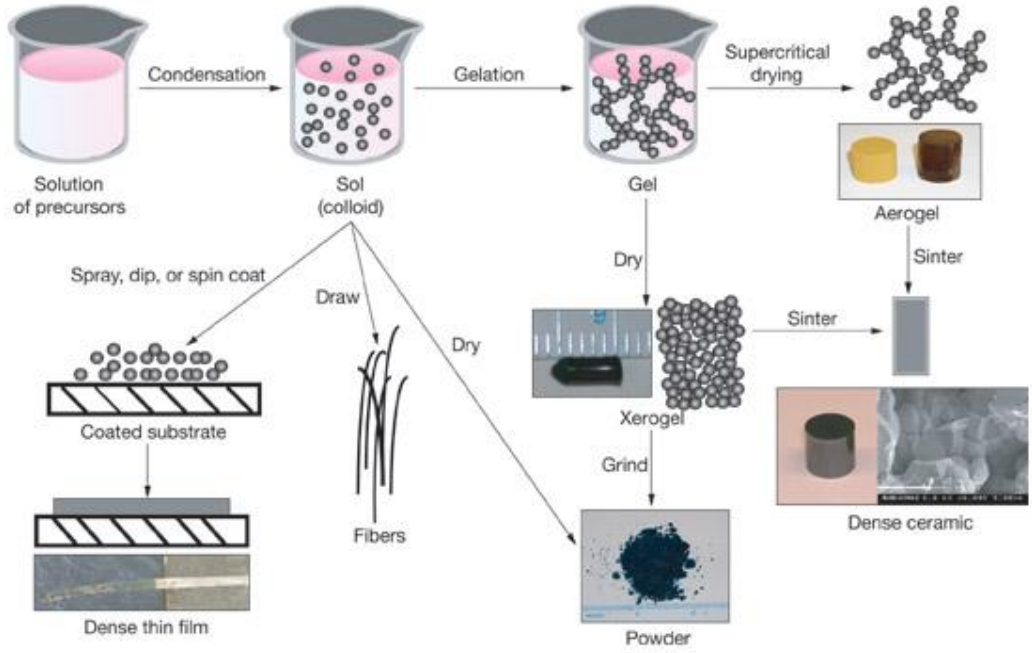

Figure 2.1: Various steps in the sol-gel process to control the final morphology of the product.(Mehrotra and Singh 1997)

The sol-gel conversion of metal alkoxides involves two main reaction types: hydrolysis and condensation (Scheme 2.1). During hydrolysis, the alkoxide groups (-OR) are replaced via the nucleophilic attack of the oxygen atom of a water molecule under release of alcohol and the formation of a metal hydroxide. In most cases hydrolysis step requires catalyst as can be seen from Figure 2.2. Condensation reactions between two hydroxylated metal species leads to M-O-M bonds under release of water (oxolation), whereas the reaction between a hydroxide and an alkoxide leads to M-O-M bonds under release of an alcohol (alkoxolation). Steps involved in the condensation of tetra ethyl orthosilicate (TEOS) during sol-gel process are shown in Figure 2.3. In the present work, Sr_2SiO_4 has been synthesized using sol-gel method. Main reactions in the sol-gel process using metal alkoxides. Hydrolysis (Eq. 2.1) and condensation, involving oxolation (Eq. 2.2) and alkoxolation (Eq. 2.3)

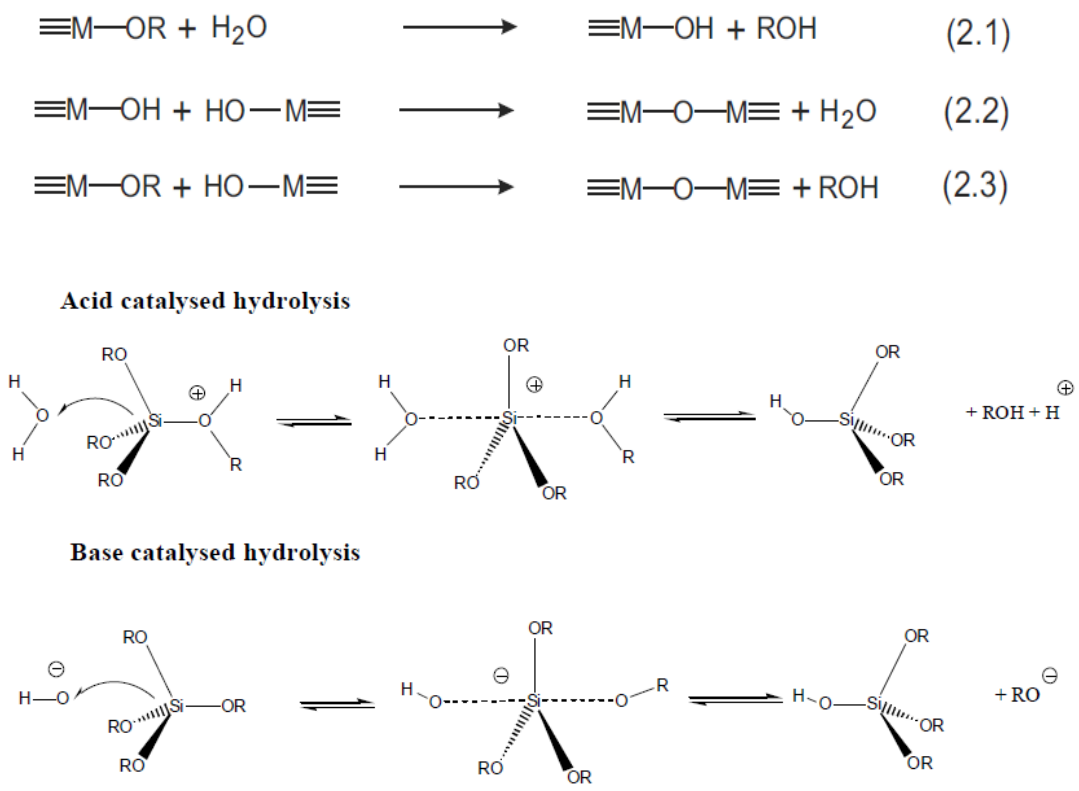

Figure 2.2: Acid and base catalyzed hydrolysis step

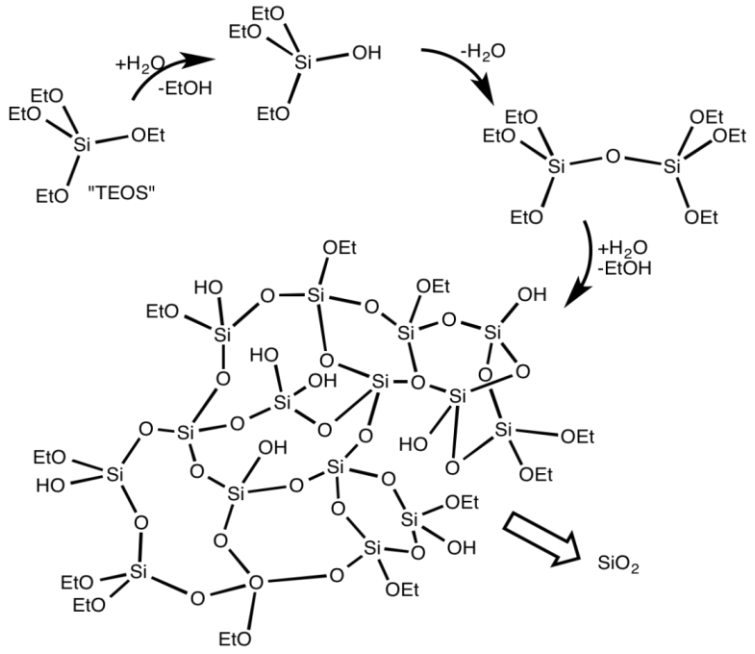

Figure 2.3: Simplified representation of the condensation of TEOS in sol gel process

2.1.3 Gel-Combustion Method:

Combustion synthesis (CS) or self-propagating high-temperature synthesis (SHS) is an effective, low-cost method for production of various industrially useful bulk/ nano-crystalline powders of oxide ceramics, at a lower calcination temperature in a surprisingly short time.(Gupta et al. 2014a, Gupta et al. 2012b, Liao et al. 2005, Shea et al. 1996, Wang et al. 2016, Martirosyan et al. 2002, Martirosyan et al. 2001, Martirosyan et al. 2009) The solution-combustion is a two-step process viz. (i) formation of a precursor and (ii) auto-ignition.

In a typical reaction, the precursor (mixture of water, metal nitrates and fuel) on heating decomposes, dehydrates and ruptures into a flame. The resultant product is a voluminous, foamy powder, which occupies the entire volume of the reaction vessel. The chemical energy released from the exothermic reaction between the metal nitrates and fuel can rapidly heat the system to high temperatures without an external heat source. Nanomaterials synthesized by combustion route are generally homogeneous, contain fewer impurities, and have higher surface areas than powders prepared by conventional solid-state methods. The parameters that influence the reaction are the nature of fuel, fuel to oxidizer ratio, ignition temperature and water content of the precursor mixture. The major advantage of this method is that large-scale production can be made at relatively low temperatures and disadvantage is that the particles obtained are highly agglomerated and cannot be dispersed in solvents.

The formation of the precursor (viscous liquid or gel), is a primary condition for an intimate blending of the starting constituents and preventing the random redox reaction between a fuel and an oxidizer. The very high exothermicity generated during combustion manifests in the form of either a flame or a fire and hence, the process is termed as auto-ignition process. The nature of the fuel and its amount, are some of the important process parameters, for getting the

transparent viscous gel without any phase separation or precipitation.(Purohit and Tyagi 2002) Thus, the basic characteristics of the fuel are that it should be able to maintain the compositional homogeneity among the constituents and also undergo combustion with an oxidizer at a low ignition temperature. The commonly used fuels are glycine, citric acid, urea, ascorbic acid etc. The two events, which occur during combustion, are (i) generation of heat of combustion, and (ii) gas evolution. Heat of combustion (or flame temperature) helps in crystallization and formation of the desired phase. However, a very high flame temperature can adversely affect powder characteristics like increase in the crystallite size, formation of hard agglomerates and thereby reduction in the surface area and sinterability. The evolution of gaseous products during combustion dissipates the heat of combustion and limits the rise of temperature, thus reducing the possibility of premature local partial sintering among the primary particles. The powder characteristics are primarily governed by heat of combustion and gas evolution, which themselves are dependent on nature of the fuel and oxidant-to-fuel ratio.(Chavan and Tyangi 2004)

Depending on the type of the precursors, as well as on conditions used for the process organization, the SCS may occur as either volume or layer-by-layer propagating combustion modes. This process not only yields nanosized oxide materials but also allows uniform (homogeneous) doping of trace amounts of rare-earth impurity ions in a single step. Among the gamut of papers published in recent years on SCS, synthesis of luminescent materials and catalysts occupy the lion share. The latest developments in SCS technique are discussed based on the materials applications. The synthesis of nanophosphors is currently a hot topic in the field of CS. There are various advantages and disadvantages of gel-combustion method over other routes as mentioned in table 2.1. We have synthesized $SrZrO_3$ using gel-combustion method.

Table 2.1: Advantages and disadvantages of Combustion route

	Advantages	**Disadvantages**
1	Decreases diffusion path length	Safety related issues
2	Size control	Evolution of NOX
3	Less Energy and time consuming	Shape control is a problem
4	Metastable state can be synthesized	Synthesis of non-oxide ceramic is difficult
5	Better powder characteristics	Scaling up is an issue

2.1.4 Polymeric Precursor Method:

The polymerized complex technique, known originally as the Pechini method(Pechini 1967) (wherein a solution of ethylene glycol (EG), citric acid (CA) and metal ions is polymerized to form a polyester-type resin), has received considerable attention among others. This technique offers a convenient means in which a wide range of metal compounds stay as soluble species throughout the resin formation and leaves enough flexibility for the system to persist without undergoing precipitation. Because of the high degree of compositional control afforded by the polymerized complex technique, it has been preferably used to study the effects of slight change in composition on electrical properties of high technology multicomponent oxides. (Chan et al. 1981, Kakihana 1996)

The polymeric citrate method is based on the Pechini-type reaction route.(Pechini 1967, Kakihana and Arima 1999) It involves reacting a mixed solution of citric acid, ethylene glycol and the desired cations to form a polyester type of gel. The metal ions can be immobilized in a rigid polyester network, which is charred off by heating the gel. This can greatly reduce the diffusion path lengths of a reactant during the processing. Thus, a distinct advantage over most

other methods is that very pure mixed metal oxides can be prepared. Also compared to the ceramic route, this method can give rise to homogeneous and fine-grained powders at relatively lower reaction temperature. Figure 2.4 shows various stages involved in the synthesis using polymeric precursor route or polymerization complex method.

Approach: Decrease diffusion distances through intimate mixing of cations.

Advantages: Lower reaction temps, possibly stabilize metastable phases, eliminate intermediate impurity phases, and produce products with small crystallites/high surface area.

Disadvantages: Reagents are more difficult to work with, can be hard to control exact stoichiometry in certain cases, sometimes it is not possible to find compatible reagents (for example ions such as Ta^{5+} and Nb^{5+} immediately hydrolyze and precipitate in aqueous solution).

Methods: Apart from using mixed cation reactants, all precursor routes involve the following steps:

1. Mixing the starting reagents together in solution.
2. Removal of the solvent, leaving behind an amorphous or nano-crystalline mixture of cations and one or more of the following anions: acetate, citrate, hydroxide, oxalate, alkoxide, etc.
3. Heat the resulting gel or powder to induce reaction to the desired product.

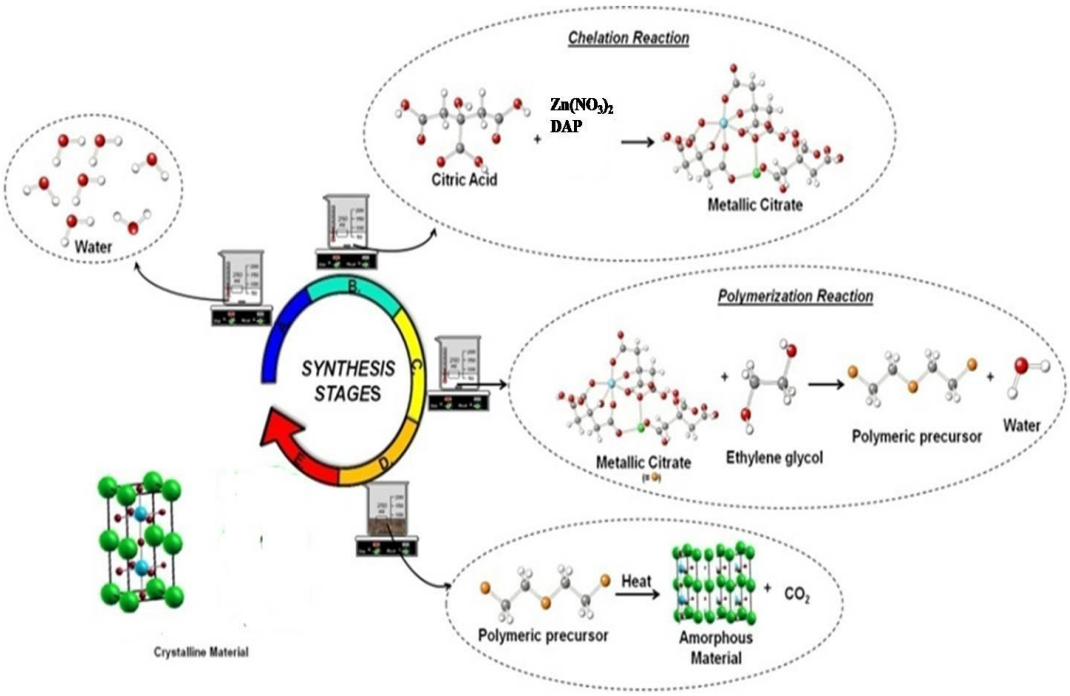

Figure 2.4: Typical synthesis stages in polymeric precursor route

2.1.5 Microemulsion Method/*Reverse Micellar Route:*

A micro-emulsion is a mixture of water, water-insoluble and water-soluble components forming a visually homogeneous, transparent liquid. One or more active ingredients may be present in either the aqueous phase, the non-aqueous phase, or in both phases. A variety of micro-emulsion formulations may be prepared in which the aqueous phase can be considered the dispersed phase, the continuous phase or, alternatively, where the two phases are continuous. In all cases micro-emulsions will disperse into water to form either conventional emulsions or dilute micro-emulsions. Synthesis of nano particles via micro emulsions is a simple and powerful technique, which does not require specialized or expensive equipment's. Here precipitation reaction is carried out in mono dispersed aqueous cores dispersed in non-polar solvent and are stabilized by surfactant / co surfactant molecules. The material obtained is micro homogeneous, because the desired stoichiometry is maintained. The advantage of this technique over other

methods of synthesis lies in the fact that a micro emulsion may assume a variety of structures depending on the constituents and the location within the phase diagram. It may therefore be possible to control not only the size but also the morphology of the product nano particles by proper choice of the composition of the micro emulsion system.

It is a macro homogenous transparent solution formed by dissolving surfactant in organic solvent with limited amount of water. Reverse micelles can be defined as "Water in oil micro emulsion (see Figure 2.5) in which polar head groups of surfactant molecules are attracted by aqueous core and directed towards inside and hydrocarbon chain i. e. a polar part is attracted by non-aqueous phase and directed towards outside." The non-polar tail of surfactant molecules encounters the organic phase and the polar heads sequester together, forming a vesicle, which encloses the water pool inside the cavity. It consists of nanometer sized, monodisperse water droplets. It can easily control the size and shape of the aqueous core by varying the value of water to surfactant ratio (Wo). The reverse-micelles obtained at a ratio of the aqueous phase to the surfactant leads to uniform–size nano-reactors and have an aqueous core of 5-10 nm in which it is possible to precipitate the inorganic material. It was initially assumed that these nanodroplets could be used as templates to control the final size of the particles, however, the research carried out in the last few years has shown that besides the droplet size, several other parameters also play an important role in the final size distribution.

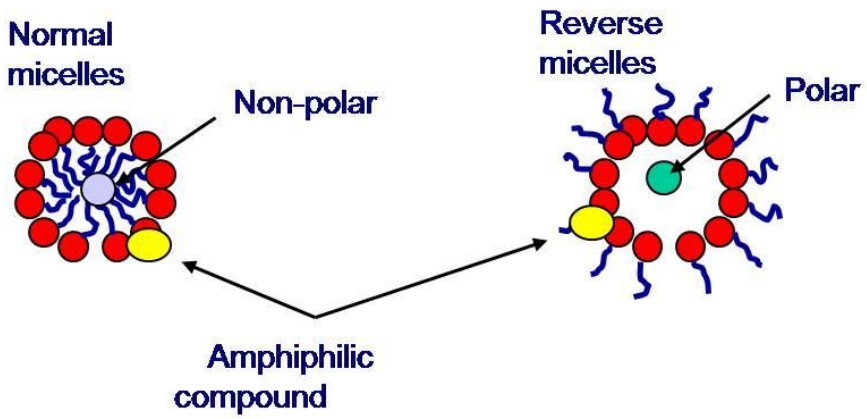

Figure 2.5: A typical structure of micelle.

Among all the chemical processes, the microemulsion processing (reverse micelle synthesis) has been demonstrated as a very versatile and reproducible method.(Boutonnet et al. 1982, Pileni et al. 1992, Ahmad et al. 2005, Ahmad and Ganguli 2004) This method is superior to many others in terms of being able to deliver homogeneous and monodisperse nanoparticles of a variety of metals(Lisiecki and Pileni 1993, Wilcoxon et al. 1993), oxides(Osseo-Asare and Arriagada 1999, H and R 1997), and chalcogenides(A et al. 1990). The reaction takes place in the aqueous cores of the reverse micelles which are dispersed in an organic solvent and are stabilized by a surfactant. The dimensions of these aqueous cores are in the Nano regime and are thus being referred to as nanoreactors. The product obtained after the reaction is homogeneous. The other advantage of using this methodology is that the morphology of the product can also be controlled as the surfactant aggregates from a variety of structures which are used as templates. The size of the core of the reverse micelles can also be controlled by changing Wo ($[H_2O]$/ [surfactant]). Thus, the size and morphology of the product can be controlled by proper choice of the composition of the microemulsion system.

CHAPTER III

DIFFERENT TYPES OF POSSIBLE CHARACTERIZATION TECHNIQUES FOR NANOMATERIAL

3.1.1. X-ray Diffraction:

The Discovery of X-ray has been a milestone in the scientific regime and research development. X-rays were discovered accidentally by Wilhelm Roentgen in 1895 during an experiment involving electrical current passing through gases in a novel way to study the effects of cathode rays. Roentgen observed that unknown rays were ejected when current pass through the discharged tube. At the time Roentgen, was working with barium platinocyanide in a dark room and a well-covered discharged tube allowing for luminescence to happen. He noticed that even when the screen was placed at a distance in front of the unknown rays the screen was fluorescent. This allows Roentgen to conclude that these rays could pass through any type of matter and had an electromagnetic radiation. These rays were later known as X-rays. Roentgen to win the first Nobel Prize in Physics in 1901 due to his discovery of X-rays, revolutionizing the field of medicine.

3.1.2. Diffraction Principle:

X-rays interact primarily with electrons in atoms. When an incident x-ray wave approaches an atom, it is scattered, and interference of these scattered waves occur. If the atoms have a periodic arrangement, as in a crystal, the scattering produces a diffraction pattern with sharp maxima

(peaks) at certain angles. The peaks in the x-ray diffraction pattern are directly related to the interatomic distances. An incident x-ray beam interacting with the atoms arranged in a periodic manner is shown in two dimensions (2-D) in Figure 3.1. The atoms can be viewed as forming different sets of planes in the crystal. For a given set of lattice plane with an interplanar distance of, the condition

$$2d \sin \theta = n\lambda \qquad (3.1)$$

This is known as Bragg's law, after W.L. Bragg, who first proposed it. In equation, θ is the Bragg angle, which is half of the scattering angle; an integer representing the order of the diffraction peak and λ is the wavelength of the x-rays.

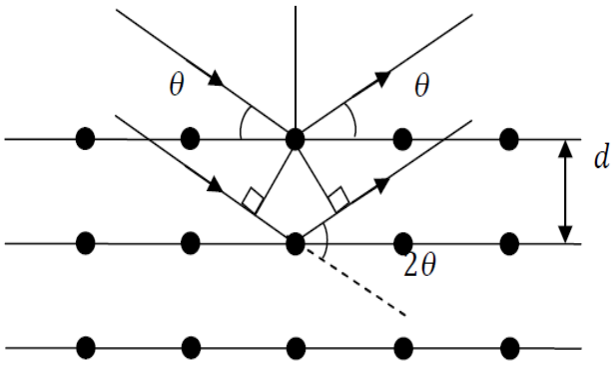

Figure 3.1: Scattering of x-rays from atoms and Bragg's law

3.1.3. X-ray Production:

X-rays are a part of the spectrum of electromagnetic radiation in the region between ultraviolet and gamma rays. X-rays have a wavelength between 10.0 and 0.1 Å. They are produced when fast-moving electrons of enough energy are decelerated. In an x-ray tube, the high voltage maintained across the electrodes draws electrons toward a metal target (the anode).

X-rays are produced at the point of impact and radiated in all directions. The kinetic energy of the electrons is transformed into electromagnetic energy (x-rays). Since energy must be conserved, the energy loss results in the release of x-ray photons of energy equal to the energy for a diffraction (peak) to occur can be written as loss. This process generates a broad band of continuous radiation (called Bremsstrahlung, or braking radiation) as shown in Figure 3.2.

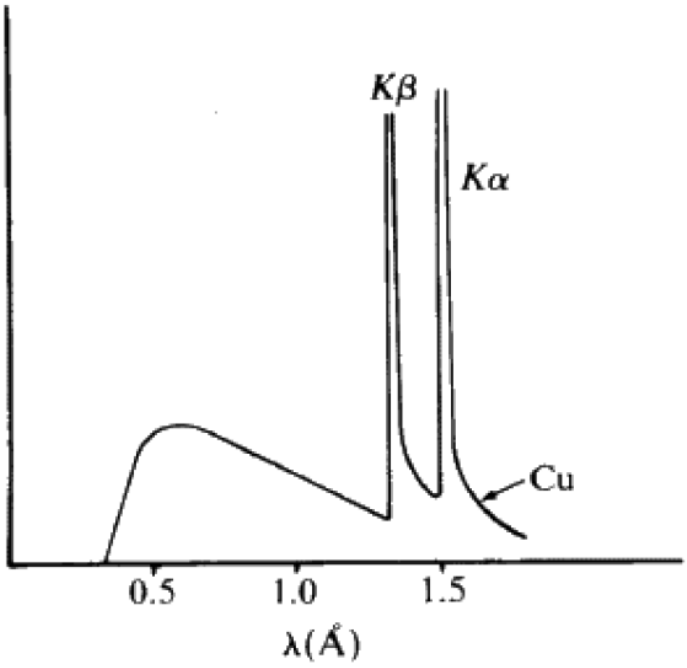

Figure 3.2: Continuous and characteristic x-rays for copper(Dept. of Chemistry and Biochemitry 2016)

If the moving electron interacts with an inner-shell electron of the target atom, characteristic x-rays can be produced. When the moving electron ionizes a target atom by removal of a K-shell electron, transition of an orbital electron from an outer to an inner shell will occur, accompanied by the emission of an x-ray photon. The x-ray photon has energy equal to the difference in the binding energies of the orbital electrons involved. If an L-shell electron moves to replace a K-shell electron, a Kα x-ray is produced (with wavelength 1.54178 Å for Cu).

If an M-shell electron moves to replace a K-shell electron, a K_β x-ray is produced (with wavelength 1.39217 Å for Cu). These characteristic x-rays, also shown in Figure 3.3, are suitable for diffraction experiments. To obtain monochromatic x-rays a suitable metal filter can be used. Nickel strongly absorbs x-rays below 1.5 Å and can be used to filer the K β x-rays from copper.

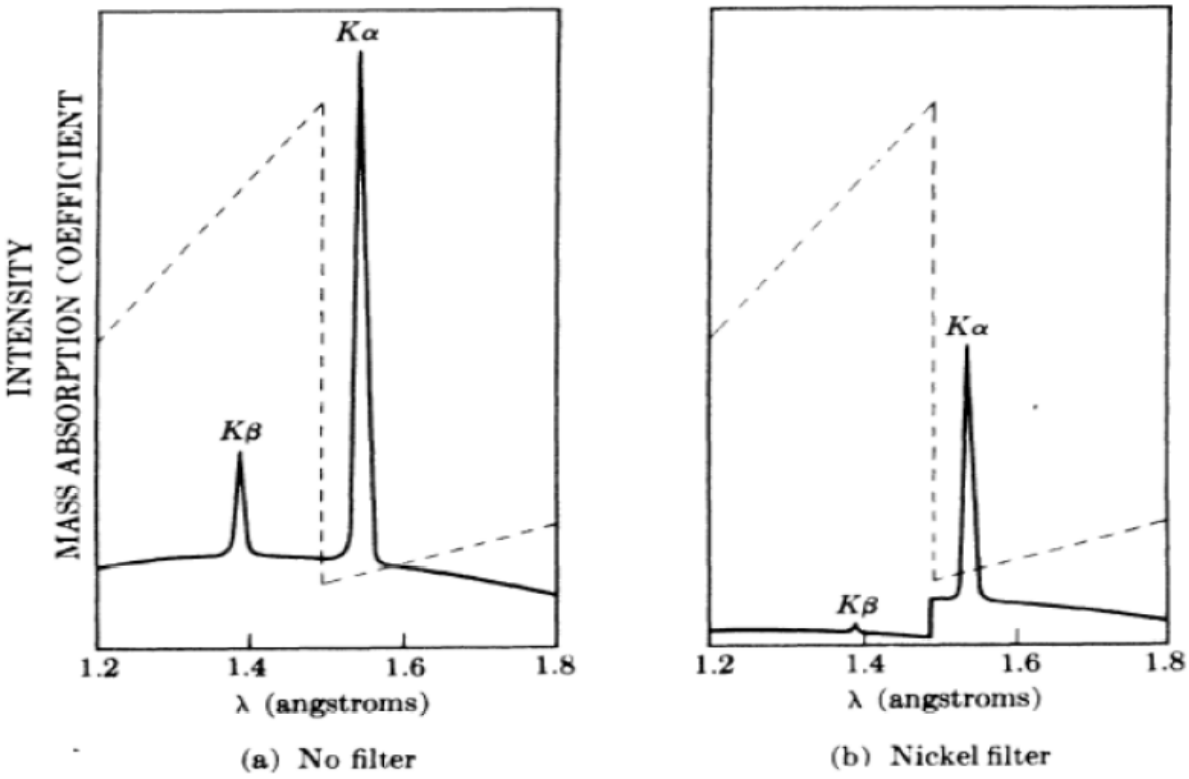

Figure 3.3: Using a Nickel filter for Cu X-rays (Cullity 1956)

3.1.4. XRD Diffractometer:

A diffractometer records the diffraction pattern of a sample. The essential features of a diffractometer are presented schematically in Figure 3.4. It consists of an x-rays source (usually an x-ray tube) producing monochromatic x-rays of known wavelength, a sample stage, a detector, and a way to vary the angle. The x-rays are focused on the sample at some angle θ, while the detector reads the intensity of the diffracted x-rays it receives at the scattering angle 2θ.

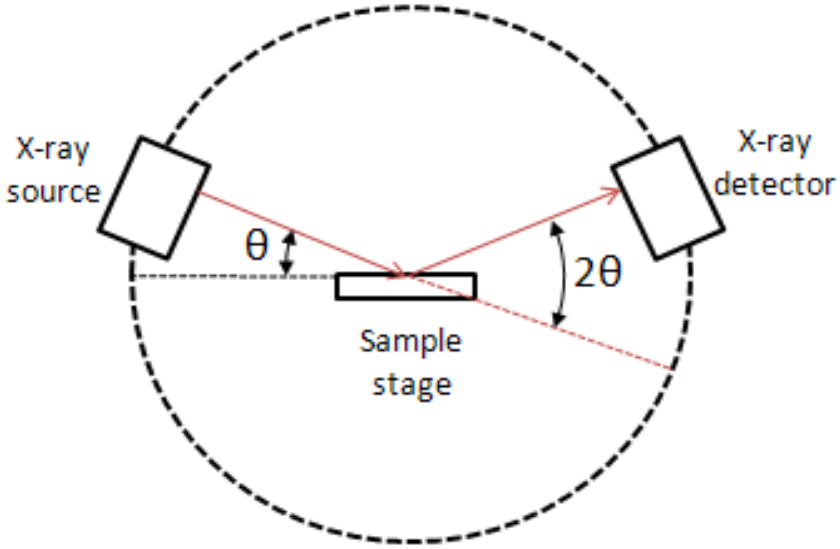

Figure 3.4: X-ray diffractometer(MindTouch 2017)

3.1.5. XRD Applications: Phase Purity and Crystallite Size:

With the XRD pattern the identification of an unknown crystalline material becomes possible. Bragg's law is used to convert the angles where peaks occur to interplanar spacings (d-spacings) using Bragg's law (Equation 3.1). Files of d-spacings for hundreds of thousands of inorganic compounds for comparison are available in the Powder Diffraction Files (PDF) of the International Centre for Diffraction Data (ICDD).

When crystallites are less than 100 nm in size, appreciable broadening in the x- ray diffraction reflections will occur. These regions may in fact correspond to the actual size of the particles. The grain size can be calculated from the broadening of the diffracted beam using the Scherer's formula:

$$t = K\lambda / B \cos\theta \qquad (3.2)$$

Where, t = Diameter of the grain, λ = Wavelength of the X-ray (for Cu-Kα, λ = 1.5418 Å), θ = Bragg angle or diffraction angle, B = Full width at half maximum (FWHM) of a diffraction peak, K = Scherer's constant and its value are the order of unity for usual crystals. Normally, K = 0.9 is used. Hence,

$$t = 0.9\lambda / B \cos\theta \qquad (3.3)$$

The line broadening B is measured from the broadened peak at full width at half maxima and obtained from the Warren's formula:

$$B^2 = B_M^2 - B_S^2 \qquad (3.4)$$

Where, B_M = Full width at half maximum of the sample, B_S = Full width at half maximum of a standard sample of grain size of around 2 μm. Quartz was used as the standard and the reflections were chosen such that the sample and standard had closest possible 2θ values and the operations carried out on two reflections were identical.

In the present case measurements were carried out on a STOE X-ray diffractometer equipped with Ni filter, scintillation counter and graphite monochromator. The diffraction patterns were obtained using monochromatic Cu-K_α radiation (λ= 1.5406Å) keeping the scan rate at 1sec./step in the scattering angle range (2θ) of 10^o to 60^o. The $K_{\alpha 2}$ reflections were removed by a stripping procedure to obtain accurate lattice constants. The goniometer was calibrated for correct zero position using silicon standard. Samples are well grounded and made in the form of a slide. As all the micro crystals are randomly oriented, at any point on the sample different planes from crystals will be exposed to X-rays.

3.1.6. Thermal Analysis: TGA/DTA/DSC

Thermal analysis is a branch of materials science where the properties of materials are studied as they change with temperature. Several methods are commonly used – these are distinguished from one another by the property which is measured:

1. Dielectric thermal analysis (DEA): dielectric permittivity and loss factor
2. Differential thermal analysis (DTA): temperature difference
3. Differential scanning calorimetry (DSC): heat difference
4. Dilatometry (DIL): volume
5. Dynamic mechanical analysis (DMA): mechanical stiffness and damping
6. Evolved gas analysis (EGA): gaseous decomposition products
7. Laser flash analysis (LFA): thermal diffusivity and thermal conductivity
8. Thermogravimetric analysis (TGA): mass
9. Thermomechanical analysis (TMA): dimension
10. Thermo-optical analysis (TOA): optical properties

Thermal analysis methods are essential for understanding the compositional and heat changes involved during reaction. They are useful for investigating phase changes, decomposition and loss of water or oxygen and for constructing phase diagrams.

In TGA, the weight of a sample is monitored as a function of time as the temperature is increased at a controlled uniform rate. Loss of water of crystallization or volatiles (such as oxygen, CO_2, etc.) is revealed by a weight loss. Oxidation or adsorption of gas shows up as a weight gain. A phase change is generally associated with either absorption or evolution of heat. In DTA experiments, the sample is placed in one cup and a standard sample (like Al_2O_3) in the other cup. Both cups are heated at a controlled uniform rate in a furnace, and the difference in

temperature (ΔT) between the two is monitored and recorded against time or temperature. Any reaction involving heat change in the sample will be represented as a peak in the plot of ΔT vs. T. Exothermic reactions give an increase in temperature, and endothermic reaction leads to a decrease in temperature and the corresponding peaks appear in opposite directions.

DSC is a thermo-analytical technique in which the difference in the amount of heat required to increase the temperature of a sample and reference is measured as a function of temperature. Both the sample and reference are maintained at nearly the same temperature throughout the experiment. Generally, the temperature program for a DSC analysis is designed such that the sample holder temperature increases linearly as a function of time. The reference sample should have a well-defined heat capacity over the range of temperatures to be scanned. The result of a DSC experiment is a curve of heat flux versus temperature or versus time. There are two different conventions: exothermic reactions in the sample shown with a positive or negative peak, depending on the kind of technology used in the experiment. This curve can be used to calculate enthalpies of transitions. This is done by integrating the peak corresponding to a given transition

3.1.7. Electron Microscopy: SEM/TEM

Micro-structural characterization has become important for all types of materials as it gives substantial information about the structure-property correlation. Micro- structural characterization broadly means ascertaining the morphology, identification of crystallographic defects and composition of phases, estimating the particle size, etc. Electron microscopic techniques are extensively used for this purpose. Electron microscopy is based on the interaction between electrons (matter wave) and the sample.

Electron microscopes are scientific instruments that use a beam of highly energetic electrons to examine objects on a very fine scale. They are widely used as tools for research, quality assurance and failure analysis in material science. They are indispensable implements in biological and life sciences. In electron microscopy beams of electrons are used to produce images wavelength of electron beam is much shorter than light, resulting in much higher resolution. Table 3.1 shows the advantages and disadvantages of electron microscope while Table 3.2 shows the comparison between light optical microscope and electron microscope. Figure 3.5 depicts the range of optical and electron microscope.

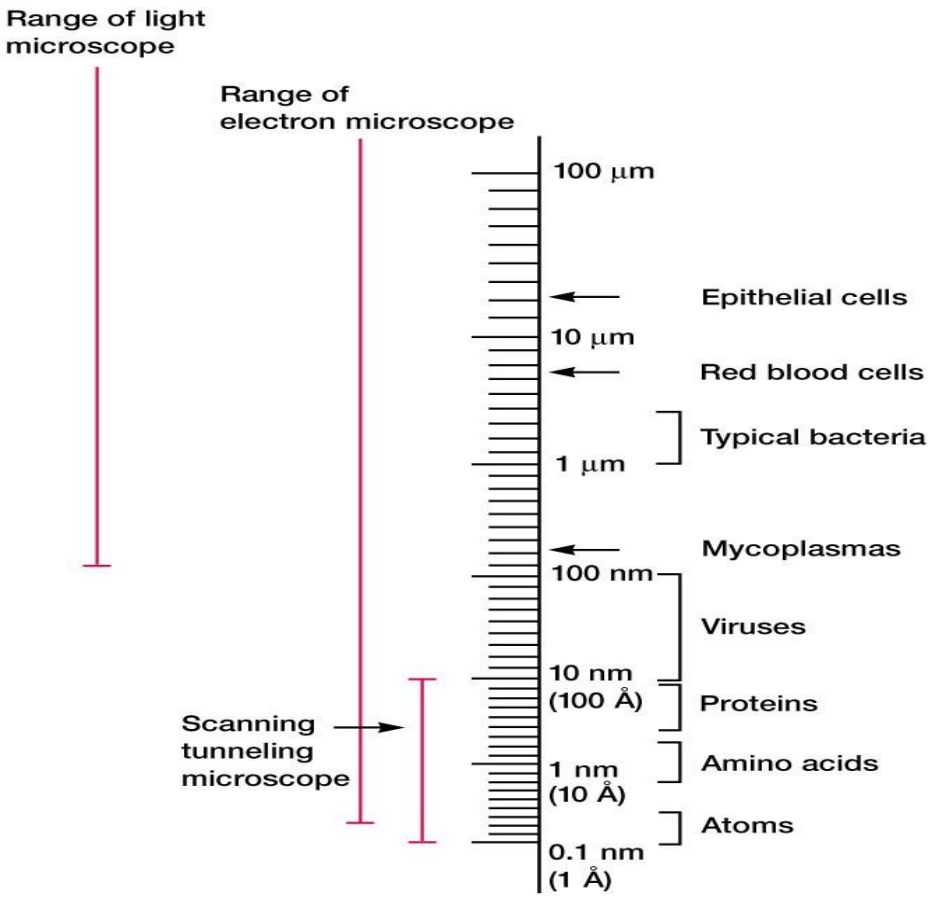

Figure 3.5: Typical range of light and electron microscope

Table 3.1: Advantages and disadvantages of electron microscope

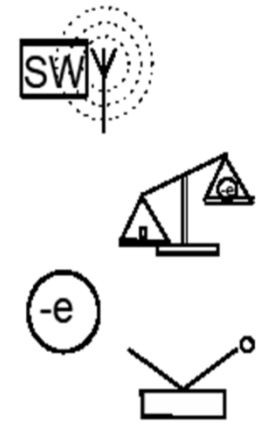

Advantages

Shorter wavelength	Better resolution
Low mass	Non-destructive for most specimens
Negative charge	Beam focused / deflected via electric coils
Strong interaction electron-matter	Different signals available - Elastic scattering: imaging - Phase shift: weak-scatter imaging - Diffraction: crystallography - Inelastic scattering / ionisation: chemical analysis

Disadvantages

Strong interaction electron-matter	Excellent vacuum and **thin specimen for TEM,** **conductive specimen for SEM**

Table 3.2: Comparison between light optical microscope and electron microscope

	Light Microscopy	Electron Microscopy
Carrier	Photons	Electrons
Wavelength	400–800 nm (visible) 200 nm (ultra violet)	0.0037 nm (at 100kV) 0.0020 nm (at 300kV)
Medium	Air	Vacuum
Observation	Direct	Via fluorescent screen
Contrast by	Absorption, reflection, phase changes, polarisation…	Scattering, phase changes and diffraction
Information	Mass Density Distribution	Mass Density Distribution, Crystallographic and Chemical
Resolving Power	0.2 µm (visible) 0.1 µm (ultra violet)	0.2 nm (point) 0.1 nm (line)
Lenses	Glass	Electromagnets
Focusing and Alignment	Mechanically	Electronically
Aperture Angle	<64°	0.2–0.7°
Depth of Focus	0.1µm–0.1m	1–10,000m
Depth of Field	(1-1k) <0.1µm	(1k–1000k) <1µm

/TV screen

In the present study, Scanning Electron Microscopy (SEM) and Transmission Electron Microscopy (TEM) have been used to characterize the nano powders. The principle and experimental details of these two techniques are given below.

They can be used to study the following in **MATERIALS SCIENCE**:

1. Topography - the surface features of an object or ` how it looks', its texture, direct relation between these features and material's properties like hardness, reflectivity etc.
2. Morphology - the shape and size of the particles making up the object. There is a direct relation between these structures and material's properties like strength, ductility, reactivity etc.
3. The composition of the specimen - the elements and compounds that the specimen is composed of and their relative amounts. The uniformity of composition and its relation between properties like melting point, mechanical properties can be evaluated using an electron microscope.
4. Crystallographic information - how the atoms arranged in the specimen of the object. This gives a direct relation between the atomic arrangements and the properties like conductivity, electrical characteristics, strength etc., of the material under investigation.

In fact, a complete *structure – property* correlation is possible using an electron microscope.

Scanning Electron Microscopy (SEM):

In a typical scanning electron microscope, a well-focused electron beam is incident and scanned over the sample surface by two pairs of electro-magnetic deflection coils. The signals generated from the surface by secondary electrons are detected and fed to a synchronously scanned cathode ray tube (CRT) as intensity modulating signals. Thus, the specimen image is

displayed on the CRT screen. Changes in the brightness represent changes of a property within the scanned area of the specimen. The SEM has a large depth of field, which allows a large amount of the sample to be in focus at one time. The SEM also produces images of high resolution, which means that closely spaced features can be examined at a high magnification. For carrying out SEM analysis, the sample must be vacuum compatible (~ 10-6 Torr or more) and electrically conducting. The surfaces of non-conductive materials are made conductive by coating with a thin film of gold or platinum or carbon.

Schematic representation of SEM is shown in Figure 3.6. Image formation in a SEM depends on the acquisition of signals produced from the interaction of the specimen and the electron beam. Figure 3.7 pictorially represent the types of information that can be obtained from SEM.

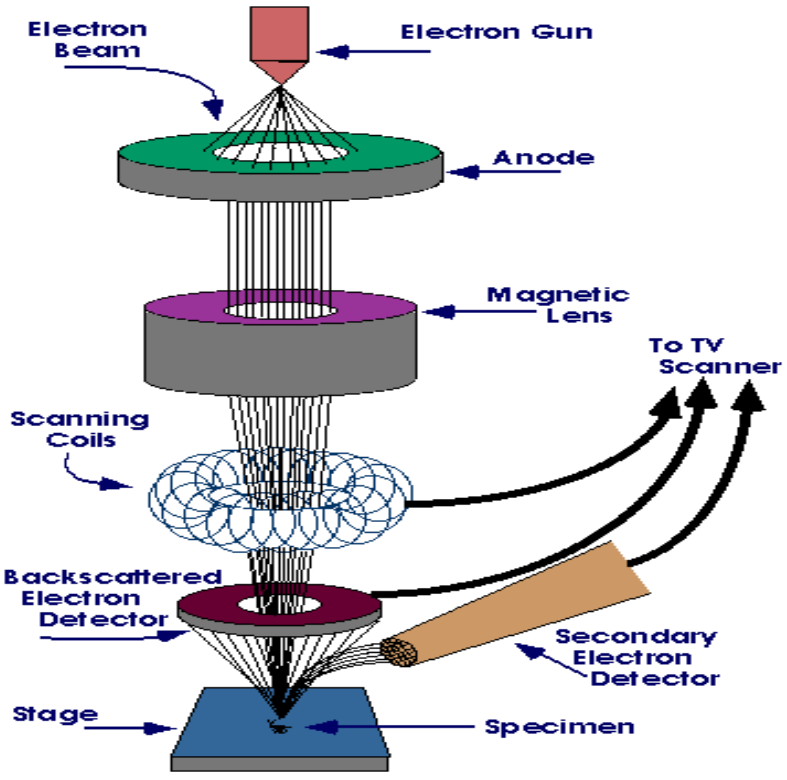

Figure 3.6: Schematic of scanning electron microscope. (Shinde et al. 2012)

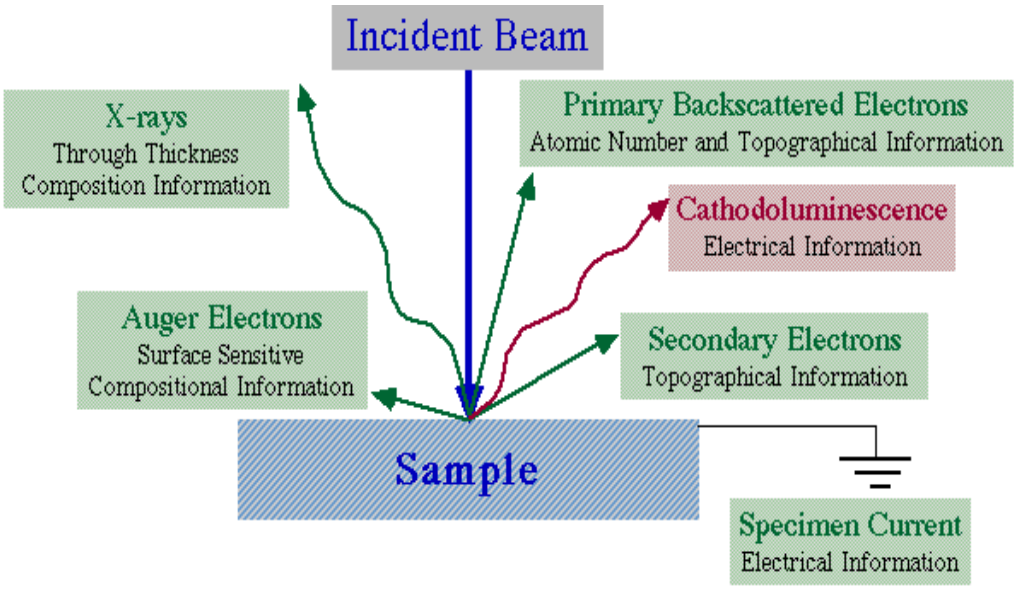

Figure 3.7: Various electron and photon emitted in SEM and information's gathered

Transmission Electron Microscopy (TEM):

Transmission electron microscopy (TEM) is a microscopy technique in which a beam of electrons is transmitted through an ultra-thin specimen, interacting with the specimen as it passes through. An image is formed from the interaction of the electrons transmitted through the specimen; the image is magnified and focused onto an imaging device, such as a fluorescent screen, on a layer of photographic film, or to be detected by a sensor such as a charge couple device (CCD) camera. TEMs are capable of imaging at a significantly higher resolution than light microscopes, owing to the small de Broglie wavelength of electrons. This enables the instrument's user to examine fine detail—even as small as a single column of atoms, which is thousands of times smaller than the smallest resolvable object in a light microscope. Schematic representation of TEM is shown in Figure 3.8. Table 3.3 represents the comparison between SEM and TEM.

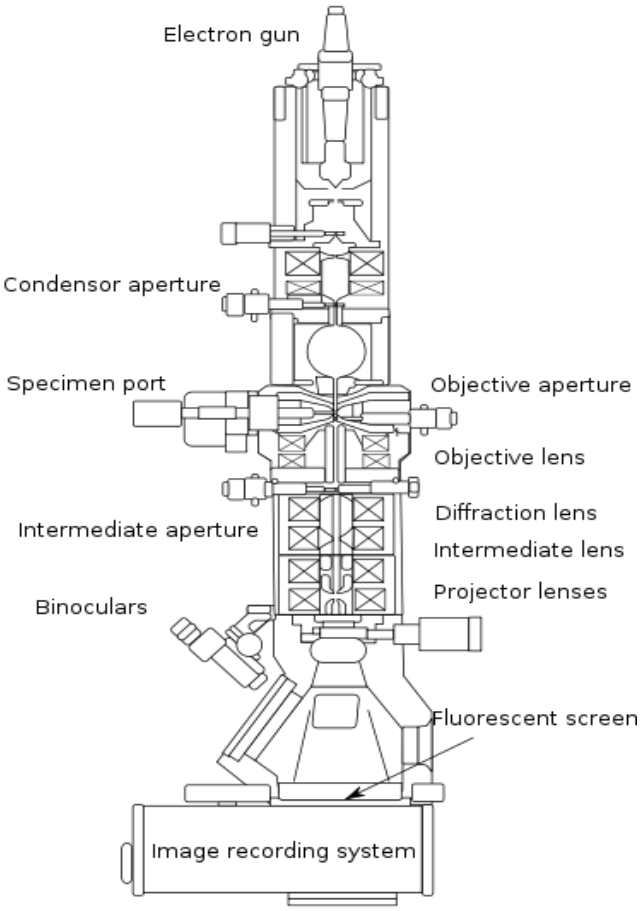

Figure 3.8: Schematic of transmission electron microscope. (H.H 2008)

Table 3.3: Comparison between SEM and TEM

SEM	**TEM**
Electrons scan the surface	Electron is transmitted through the specimen
Bulk sample can be done	Extremely thin sample
Larger depth of field	Comparatively less
Resolution-10 nm	Resolution-0.1 nm

3.1.8. Dynamic Light Scattering (DLS):

Dynamic light scattering (also known as photon correlation spectroscopy or quasi-elastic light scattering) is a technique in physics that can be used to determine the size distribution profile of small particles in suspension or polymers in solution. This method is used to determine the size of particles in the 5 to 5000 nanometer range. It uses the scattered light to measure the rate of diffusion of the particles. This motion data is conventionally processed to derive a size distribution for the sample, where the size is given by the "Stokes radius" or "hydrodynamic radius" of the particle. This hydrodynamic size depends on both mass and shape (conformation). Dynamic scattering is particularly good at sensing the presence of very small amounts of aggregated protein (<0.01% by weight) and studying samples containing a very large range of masses. It can be quite valuable for comparing stability of different formulations, including real-time monitoring of changes at elevated temperatures. Hydrodynamic radius is given by Stoke – Einstein equation which is given by

$$R_h = kT / 6\Pi\eta D \qquad (3.5)$$

where, k = Boltzmann constant, T = Temperature, η = viscosity of suspension, D = diffusion coefficient. So, the hydrodynamic particle radius can be calculated if the shear viscosity of the suspension and the temperature is known.

3.1.9. Fourier Transform Infrared Spectroscopy (FTIR):

Fourier Transform Infrared Spectroscopy (FTIR) is an analytical technique which can be used to identify chemical group in organic or inorganic materials. Infrared (IR) light passing through a sample is measured in order to determine the chemical functional groups in the sample. Different functional groups absorb characteristic frequencies of IR radiation. The FTIR

spectrometers with especial accessory can measure a wide variety of sample types such as gases, liquids, and solids. Infrared rays are a part of the electromagnetic spectrum and cover the range between 0.78 and 1000 mm. The wavelength in infrared spectroscopy is often expressed as the reciprocal of the wavelength in cm, with unit as cm^{-1}. For convenience the infrared region can be divided into three parts: near, mid and far infrared (Table 3.4). The part of the mid infrared region between 4000 – 670 cm^{-1} is the most useful one.

Table 3.4: Different region in IR

Region	**Wavelength range**	
	µm	**cm^{-1}**
Near	0.78-2.5	12800-4000
Mid	2.5-50	4000-200
Far	50-1000	200-10

"Molecular bonds vibrate at various frequencies depending on the elements and the type of bonds. For any given bond, there are several specific frequencies at which it can vibrate. According to quantum mechanics, these frequencies correspond to the ground state (lowest frequency) and several excited states (higher frequencies). One way to increase the frequency of a molecular vibration is to excite the bond by having it absorb light energy. For any given transition between two states the light energy must equal the difference in the energy between the two states exactly (usually ground state (E0) and the first excited state (E1)). The energy corresponding to these transitions corresponds to the infrared portion of the electromagnetic

spectrum. Therefore, absorption of IR is restricted to vibrational states. For a molecule to absorb IR, the vibrations within a molecule must cause a net change in the dipole moment of the molecule. The alternating electrical field of the radiation interacts with fluctuations in the dipole moment of the molecule. If the frequency of the radiation matches the vibrational frequency of the molecule, then radiation will be absorbed, causing a change in the amplitude of molecular vibration." In solids the same principles apply, but the vibrations of the lattice instead of individual molecules must be considered.

3.1.10. Positron Annihilation Spectroscopy (PAS):

Positron annihilation spectroscopy (PAS) or sometimes specifically referred to as Positron annihilation lifetime spectroscopy (PALS) is a non-destructive spectroscopy technique to study voids and defects in solids. Positron annihilation spectroscopy (PAS) is a well-established technique to study the electronic structure and defects in materials(Siegel 1980, Kelly and Quick 2008, Grafutin and Prokop'ev 2002, A 1983). The lifetime of positrons depends on the electron density at the annihilation site. The technique operates on the principle that a positron or positronium will annihilate through interaction with electrons. This annihilation releases gamma rays that can be detected; the time between emission of positrons from a radioactive source and detection of gamma rays due to annihilation corresponds to the lifetime of positron or positronium. When positrons are injected into a solid body, they interact in some manner with the electrons in that species. For solids containing free electrons (such as metals or semiconductors), the implanted positrons annihilate rapidly unless voids such as vacancy defects are present. If voids are available, positrons will reside in them and annihilate less rapidly than in the bulk of the material, on time scales up to ~ 1 nanosecond. Positrons have high affinity for open volume defects and in the presence of defects; the electron density experienced by positron

is reduced leading to increase in its lifetime. Thus, positron lifetime spectroscopy can give information about the size, type and relative concentration of various defects/vacancies even at ppm level concentration. Doppler broadening technique, on the other hand, measures the momentum distribution of the annihilating electrons. The low momentum part of the Doppler spectrum (511 keV gamma line) arises mainly from the annihilation with the valence electrons and the core electrons that can be taken as signature of an element, contribute to the high momentum part of the spectrum. A very small fraction of positrons annihilates with core electrons due to the repulsion of positron by the positively charged nucleus. The amplitude of the high momentum or core electron component is, therefore, low and it is buried in the Compton background in conventional Doppler spectrum. Coincidence Doppler broadening (CDB) technique using two HPGe detectors(Puska and Nieminen 1994), is capable of eliminating the background to a great extent, e.g., peak to background ratio of ~ 10^6 can be obtained as compared to a few hundred in conventional Doppler technique. This enables unambiguous extraction of the shape and magnitude of the high momentum part of the Doppler spectrum. The chemical surrounding of the annihilation site or elemental specificity is obtained from the shape/magnitude of the high momentum core component, which carry the signature of the element. Since the core electron momentum distribution is not influenced by the physical or chemical state of the element, the CDB technique can identify the elements at the annihilation site irrespective of its physical or chemical state in the sample. Therefore, combined use of lifetime spectroscopy (LTS) and CDB technique can provide valuable information about the vacancy structure. A schematic representation of positron annihilation is shown in Figure 3.9. and Figure 3.10 shows the schematic of instrument used in positron lifetime measurement.

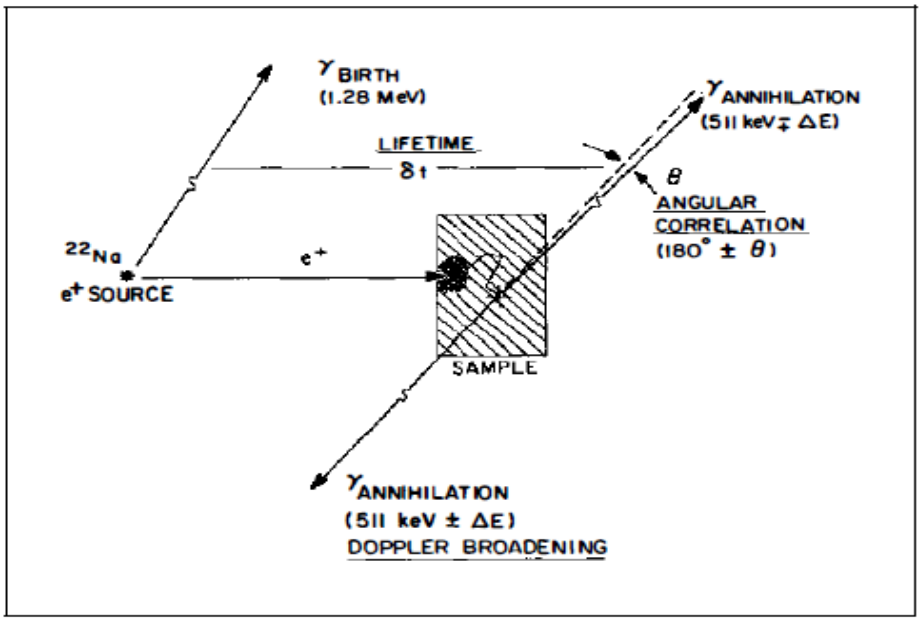

Figure 3.9: Schematic representation of positron annihilation indicating the basis for the three experimental techniques of positron annihilation spectroscopy (PAS): lifetime, angular correlation, and Doppler broadening

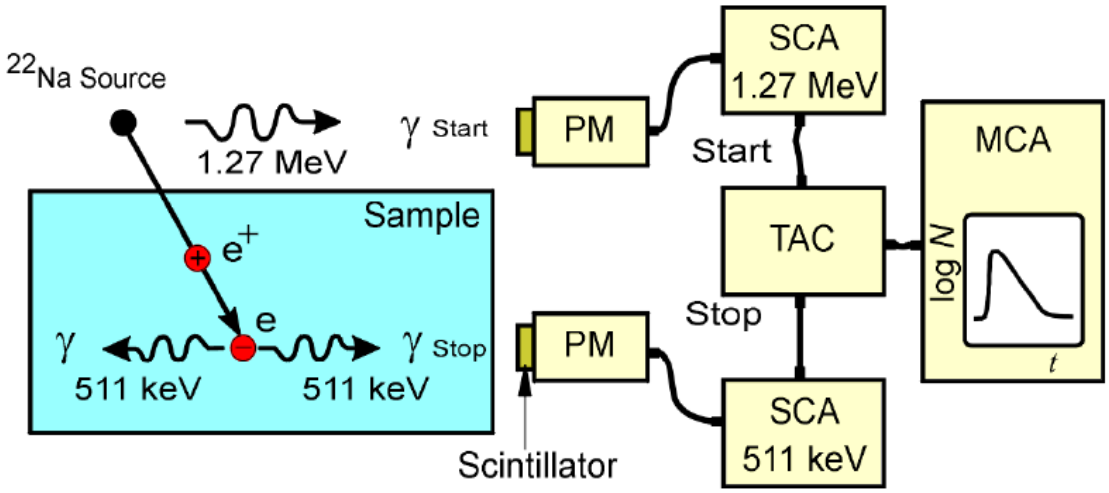

Figure 3.10: The conventional positron lifetime measurement system

3.1.11. Electron Paramagnetic Resonance (EPR) Spectroscopy:

Electron Paramagnetic Resonance, EPR, is a spectroscopic technique which detects species that have unpaired electrons. It is also often called ESR, Electron Spin Resonance. A surprisingly large number of materials has unpaired electrons. These include free radicals, many transition metal ions, and defects in materials. Free electrons are often short-lived, but still play crucial roles in many processes such as photosynthesis, oxidation, catalysis, and polymerization reactions. As a result, EPR crosses several disciplines including chemistry, physics, biology, materials science, medical science and many more.

EPR is a magnetic resonance technique very similar to NMR, Nuclear Magnetic Resonance. However, instead of measuring the nuclear transitions in our sample, we are detecting the transitions of unpaired electrons in an applied magnetic field. Like a proton, the electron has spin, which gives it a magnetic property known as a magnetic moment. The magnetic moment makes the electron behaves like a tiny bar magnet. When we supply an external magnetic field, the paramagnetic electrons can either orient in a direction parallel or antiparallel to the direction of the magnetic field. This creates two distinct energy levels for the unpaired electrons and allows us to measure them as they are driven between the two levels.

Initially, there will be more electrons in the lower energy level (i.e., parallel to the field) than in the upper level (antiparallel). We use a fixed frequency of microwave irradiation to excite some of the electrons in the lower energy level to the upper energy level. For the transition to occur we must also have the external magnetic field at a specific strength, such that the energy level separation between the lower and upper states is exactly matched by our microwave frequency as shown in Figure 3.11. To achieve this condition, we sweep the external magnet's field while exposing the sample to a fixed frequency of microwave irradiation. The condition

where the magnetic field and the microwave frequency are "just right" to produce an EPR resonance (or absorption) is known as the resonance condition and is described by the equation shown in the above Figure 3.11.

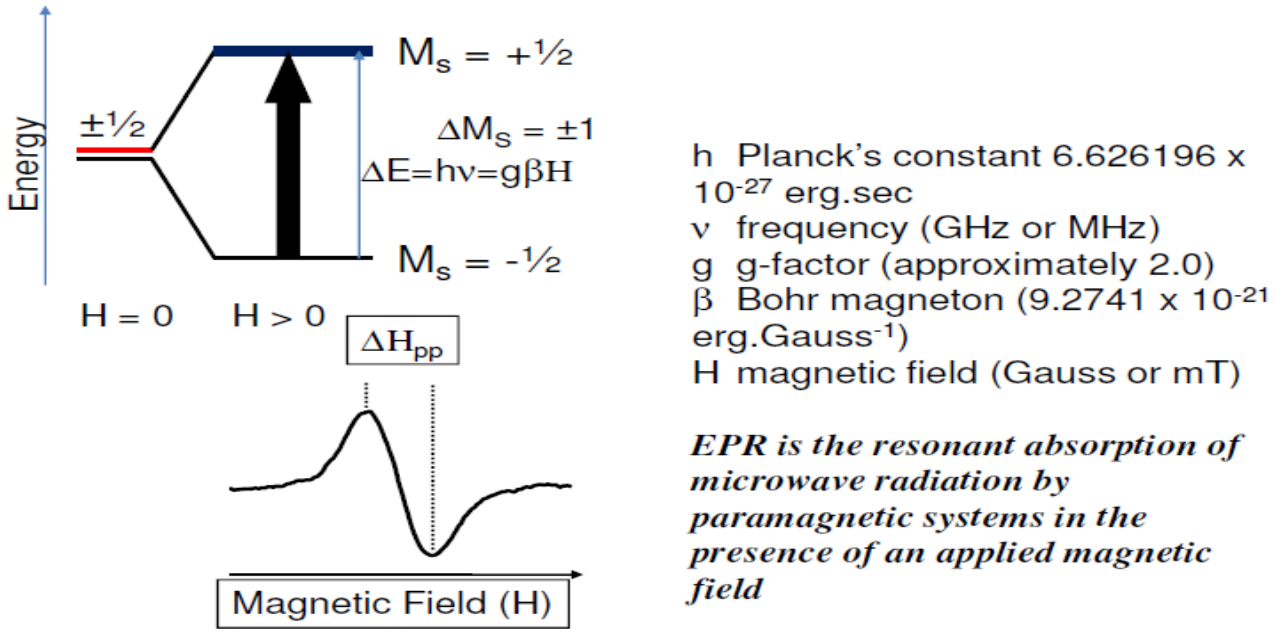

Figure 3.11: Separation from lower and the upper state for unpaired free electrons in EPR

The factor g is the measure of the total magnetic moment associated with the paramagnetic molecule and it is represented by the following equation.

$$g = 1+ [J (J +1) + S (S+1) – L (L + 1)]/ [2 J (J + 1)] \quad (3.6)$$

For free electron, S =1/2, L = 0, J = S = ½. This gives g = 2.0. The g factor is a dimensionless constant. For most of the free radicals g value is very close to 2.0000. This is because in case of free radicals the unpaired electron is not confined to a localized orbital but can move freely over the orbital resulting in the quenching of the orbital contribution (L=0). In case of transition metal complexes, on the other hand, the unpaired electron is confined in an orbital. Because of the loss of orbital degeneracy and the spin orbit coupling the g value of the complex is different from

2.0000. The g value of the transition metal complexes depends on the relative magnitude of the spin orbit coupling and the crystal field splitting. The spin orbit contribution makes "g" as a characteristic property of a transition metal ion and its oxidation state. The g factor is an anisotropic quantity i.e. its value depends on the direction of observation (orientation dependent). From the g value of a transition metal complex, one can obtain important information about the structure of the complex. In solids, the movement of the molecule is restricted and thus one can have different g values for different direction of observations. In a cubic crystal field, the metal ligand bond lengths are same along three crystallographic axes and hence g value remains the same (isotropic), that is $g_x = g_y = g_z$.

If the crystal field is tetragonal, the metal - ligand distance along the x and y axis are the same but different from the metal ligand distance along the z direction. The g value for such complex is anisotropic and they are expressed as $g_z = g_{II}$ and $g_x = g_y = g_{\perp}$. This is because it is always assumed that, the principal axis (along which the magnetic field if aligned) is along the z axis. Whereas if the symmetry of the complex is orthorhombic, all the three g values will be different that is $g_x \neq g_y \neq g_z$.

However, for most systems in solution or gas phase, the g value is averaged over all the orientations because of the free motion of the molecules. In this case, the

$$g_{av} = (g_x+g_y+g_z)/3. \qquad (3.7)$$

The simplest possible spectrometer for any spectroscopic technique has three essential components: a source of electromagnetic radiation (EMR), a sample, and a detector. To acquire a spectrum, we can vary the frequency of the EMR and measure the amount of radiation which passes through the sample with a detector to observe the spectroscopic absorptions. In an EPR

spectrometer, the source of the microwave radiation is a Klystron or a Gunn-diode. The source provides a limited range of variable frequency. The microwave source and the detector are in a box called the microwave bridge.

To measure the EPR spectrum of a paramagnetic sample, the sample is placed in a magnetic field of a resonator cavity in which microwave power is concentrated. The sample is so positioned inside the resonator cavity that the electrical component of the EMR is at its minimum and the magnetic component is at its maximum.

At the sample, the static magnetic field (H) is perpendicular to the microwave magnetic field. The interaction of magnetic spins with the oscillating magnetic field of the electromagnetic radiation leads to the EPR transitions. The EPR spectrum can be recorded by either varying the magnetic field strength or the microwave frequency. As it is easier to vary the magnetic field than the frequency due to restriction in the electronics, usually the magnetic field H is varied over a wide range and the frequency is kept constant.

An electromagnet having sweep width ranging from 5000 G to 15000 G can be used. The microwave energy is modulated, and the microwave power absorbed by the sample at the resonance is measured by the phase sensitive detector, the signal is amplified and fed to a computer for data processing. A semiconductor silicon-tungsten diode is used as a detector. Earlier, the EPR spectrum used to be recorded as a function of absorption intensity against magnetic field. Such a curve often produces broad absorption bands. In modern instrument, the first derivative of the absorption intensity (dA/dH, i.e. slope) is plotted against H. This type of plot gives more accurate g values. It may be noted that the resonance field H is not a unique fingerprint for identification of the paramagnetic species because spectra can be acquired at different frequencies. The g-factor, $g = h\nu/\beta H$ being independent of the microwave frequency, is

much better for that purpose. Notice that higher values of ‘g’ occur at low magnetic fields and vice versa. A list of fields for resonance for a g= 2 signal at microwave frequencies commonly available in EPR spectrometers is presented in the Table 3.5. In addition, Figure 3.12 shows the block diagram of typical EPR spectrometers. Figure 3.13 shows the photographs of EPR spectrometer used in current studies.

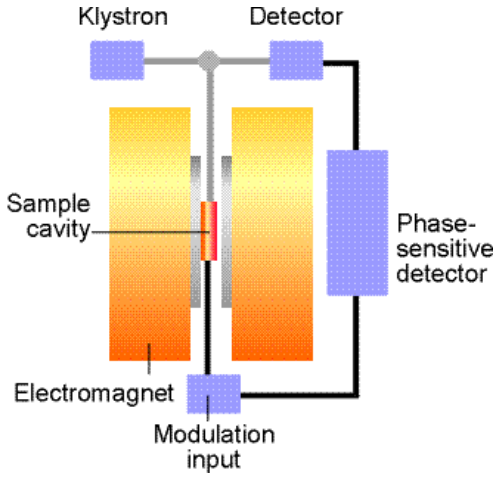

Figure 3.12: Block diagram of typical EPR spectrometers

Figure 3.13: Photograph of Bruker ESP-300 EPR spectrometer

Table 3.5: List of fields for resonance for a g= 2 signal at microwave frequencies commonly available in EPR spectrometers

Designation	□**/GHz**	$H_{(electron)}$/ ***Tesla***
L	□□□	*0.0392*
S	3.0	0.107
X	9.5	0.339
K	23	0.82
Q	35	1.25
W	95	3.3

The most widely used EPR spectrometer is the X-band spectrometer operating in the frequency range 9-10 GHz. The sensitivity of an EPR spectrometer is directly proportional to the square of the frequency, and a high frequency is preferred for a better resolution of the EPR signal. The sensitivity of the Q band spectrometer is fifteen times than that of X band spectrometers.

3.1.12. Thermally Stimulated Luminescence (TSL):

Thermoluminescence is a form of luminescence that is exhibited by certain crystalline materials, such as some minerals, when previously absorbed energy from electromagnetic radiation or other ionizing radiation (like gamma) is re-emitted as light upon heating of the material. The phenomenon is distinct from that of black body radiation. High energy radiation

creates electronic excited states in crystalline materials. In some materials, these states are *trapped*, or *arrested*, for extended periods of time by localized defects, or imperfections, in the lattice interrupting the normal intermolecular or inter-atomic interactions in the crystal lattice. Quantum-mechanically, these states are stationary states which have no formal time dependence; however, they are not stable energetically. Heating the material enables the trapped states to interact with phonons, i.e. lattice vibrations, to rapidly decay into lower-energy states, causing the emission of photons in the process. Figure 3.14 pictorially represent the process thermally stimulated luminescence.

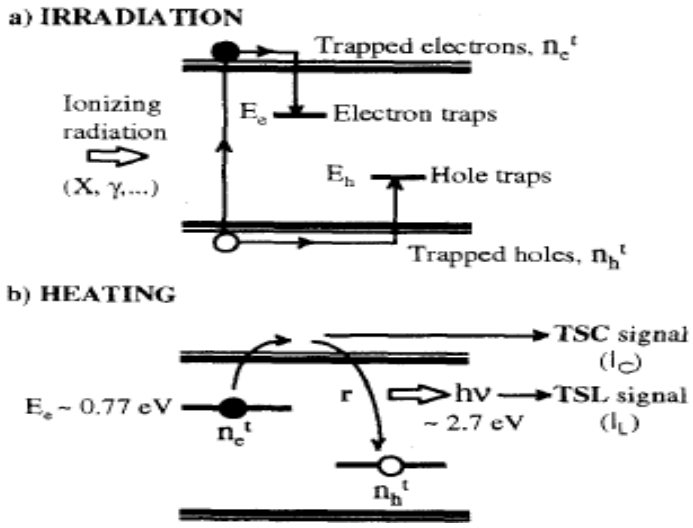

Figure 3.14: Thermally stimulated luminescence

Thermoluminescence (TL) or more specifically Thermally Stimulated Luminescence (TSL) is stimulated thermally after initial irradiation given to a phosphor by some other means (∝- rays, β -rays, γ - rays, UV rays and X-rays). Thermally stimulated luminescence (TSL) is the phenomenon of emission of light from a solid which has been previously exposed to ionizing radiation under conditions of increasing temperature. Unlike other luminescence process such as Electroluminescence, Chemiluminescence, here heat is not an exciting agent, but it acts only as a

stimulant. Hence it is better known as thermally stimulated luminescence (TSL). Excitation is achieved by any conventional sources like ionizing radiation, ∝-rays, β-rays, γ- rays and UV rays and X-rays. TSL is exhibited by a host of materials, glasses, ceramics, plastics and some organic solids. By far insulating solids doped with suitable chemical impurities, termed as activator, are the most sensitive TL materials. The band theory of solids is normally used to explain this phenomenon. When a solid is irradiated, electrons and holes are produced. The defects in the solid results in the presence of localized energy levels within the forbidden gap. On irradiation, electron and holes can be trapped at these defect sites. When the solid is heated, these trapped electrons/holes get enough thermal energy to escape from the trap to the conduction band (or valence band). From here they may get re-trapped again or may recombine with trapped holes/electrons. The site of recombination is called recombination center. If this recombination is radiative, then center is called luminescence center. Alternatively, a trapped hole can be released by heating which can recombine with a trapped electron resulting in luminescence. These features are shown diagrammatically in Figure 3.15. It is not required that all charge recombination should result in luminescence, they may be non- radiative too. The plot of intensity of emitted light versus the temperature known as a TL glow curve. A glow curve may exhibit one or many peaks depending upon the number of electron/hole traps with different trap depths, present in the lattice. These peaks may or not be well separated. The position, shape and intensity of the glow peaks therefore are characteristic of the specific material and the impurities and defects presents. Therefore, each TSL peak corresponds to the release for an electron (or hole) from a trap level within the band gap of the material. The nature of the TL glow peaks gives information about the luminescent centers present in the material. It may be mentioned that TSL is highly sensitive to structural imperfections in crystals. Defects densities as low as

$10^7/cm^3$ also can give measurable TSL if radiative recombination is dominant whereas techniques such as EPR and OAS are sensitive only for relatively higher defect concentrations such as $10^{12}/ cm^3$. The first step towards understanding the mechanism for TSL glow peaks is the identification of the trapping center and the recombination centers for the observed light emission. Apart from being a tool for the study of defects in solids, TSL has also found widespread use in radiation dosimetry, archaeological dating of pottery, ceramics, minerals etc; and meteorite research.

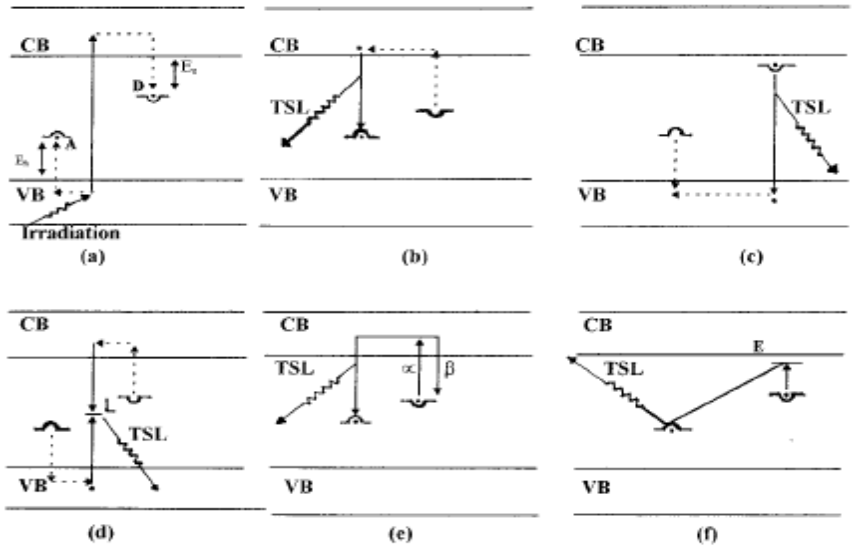

Figure 3.15: Processes involved in radiation induced electron/hole trapping and subsequent recombination on thermal stimulation with associated luminescence emission.

VB- Valence band, CB - Conduction band, Eh - Trap depth for hole, Ee - Trap depth for electron, L - Luminescent center, A - Hole trap and D - Electron trap. (a) On gamma irradiation, electrons and holes are produced and trapped at electron hole traps. (b) On thermal stimulation, trapped electron is released and recombines at trapped hole site. (c) e-h recombination at trapped electron site. (d) e-h recombination at luminescent center site. (e) Process of de trapping and re

trapping (second order kinetics, a – de trapping probability and p- re trapping probability); (f) e-h recombination via an excited state 'E' and tunneling.

3.1.13. Photoluminescence Spectroscopy (PL):

Photoluminescence spectroscopy is analytical technique that can determine quantities such as emission and excitation spectra and luminescence lifetimes. By this technique, a sample is excited by photons (generally in UV range) and the excess energy released by the sample through the emission of light can be detected and recorded for different modes, i.e. excitation, emission and luminescence decay lifetime. A spectrofluorometer is an instrument capable of recording the emission spectrum or both the excitation and emission spectra. An emission spectrum is the wavelength distribution of an emission measured at a single constant excitation wavelength. An excitation spectrum is the dependence of emission intensity, measured at a single emission wavelength, upon scanning the excitation wavelength. With a pulsed excitation source and a fast detector, the spectrofluorometer can record the luminescence lifetime decay curve. A fluorescence decay time is a measurement, at fixed wavelength, of fluorescence signals as a function of time. A decay curve is a spectrum measured within a narrow time-window during the decay of the fluorescence of interest. Two requirements for lifetime measurements are a pulsed excitation source (pulse duration short in comparison with the excited-state lifetime of the molecule) and a fast detector.

3.1.14. Physical Principle:

In photoluminescence spectroscopy, the species is first excited (by absorbing a photon) from its ground electronic state to one of the various vibrational states in the excited electronic state. Collisions with other molecules cause the excited molecule to lose vibrational energy until

it reaches the lowest vibrational state of the excited electronic state. The molecule then drops down to one of the vibrational levels of the ground electronic state, emitting a photon in the process. As molecules may drop down into any of several vibrational levels in the ground state, the emitted photons will have different energies. These processes are often visualized with the Jablonski diagram shown in Figure 3.16. There are factors which can affect fluorescence intensity which is pictorially represented in Figure 3.17.

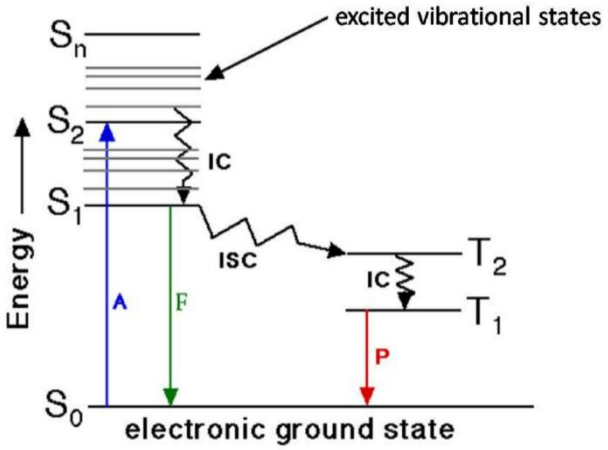

Figure 3.16: A Jablonski diagram shows the possible relaxation processes in a molecule after the molecule has absorbed a photon (A): IC = internal conversion, ISC= intersystem conversion, F= fluorescence, P= phosphorescence

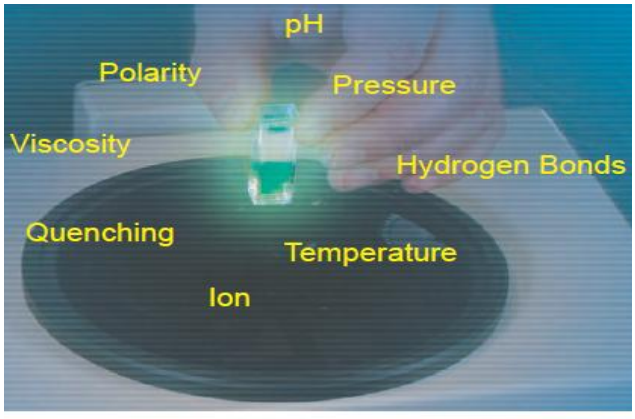

Figure 3.17: Parameters affecting fluorescence emission

3.1.15. Instrumentation: Excitation and Emission Spectroscopy

The source produces light photons. Various light sources may be used as excitation sources, including lasers, photodiodes, and lamps. Photons impinge on the excitation monochromator, which selectively transmits light in a narrow range around the specified excitation wavelength. With a laser excitation sources, filters may be used instead of a monochromator, or with a monochromator to give high quality monochromatic light. The transmitted light passes through adjustable slits that control intensity and resolution by further limiting the range of transmitted light. The filtered light passes into the sample. Emitted light goes through a filter to prevent the excitation light entering the detector and causing second order peaks. The filtered light then enters the emission monochromator, which is often positioned at a 90º angle from the excitation light path to eliminate background signal and minimize noise due to stray light. Again, emitted light is transmitted in a narrow range centered on the specified emission wavelength and exits through adjustable slits, finally entering the photomultiplier tube (PMT). Schematic diagram of a general purpose spectrofluorometer are illustrated in Figure 3.18. With most spectrofluorometer it is possible to record both excitation and emission spectra. An emission spectrum is the wavelength distribution of an emission measured at a single constant excitation wavelength. Conversely, an excitation spectrum is the dependence of emission intensity, measured at a single emission wavelength, upon scanning the excitation wavelength. For an ideal instrument, the directly recorded emission spectra would represent the photon emission rate or power emitted at each wavelength, over a wavelength interval determined by the slit widths and dispersion of the emission monochromator. Similarly, the excitation spectrum would represent the relative emission of the fluorophore at each excitation wavelength. This instrument has a xenon lamp as a source of exciting light. Such lamps are

generally useful because of their high intensity at all wavelengths ranging upward from 250 nm. The instrument shown is equipped with monochromators to select both the excitation and emission wavelengths. The excitation monochromator in this schematic contains two gratings, which decreases stray light, that is, light with wavelengths different from the chosen one. In addition, these monochromators use concave gratings, produced by holographic means to further decrease stray light. Both monochromators are motorized to allow automatic scanning of wavelength. The fluorescence is detected with a photomultiplier tubes and quantified with the appropriate electronic devices. The output is usually presented in graphical form and stored digitally. Figure 3.19 shows the fluorescence spectrometer used in current studies and the various source available such as (980 laser, microsecon lamp, XE lamp X-ray source).

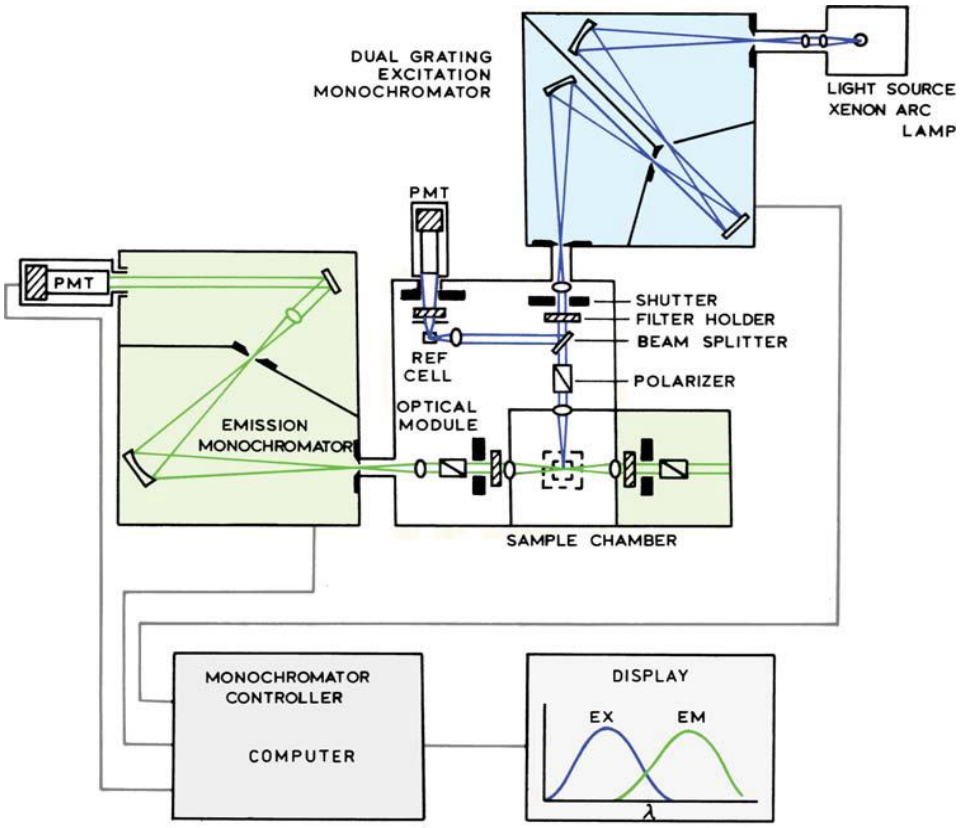

Figure 3.18: Block diagram of spectrofluorometer**.**

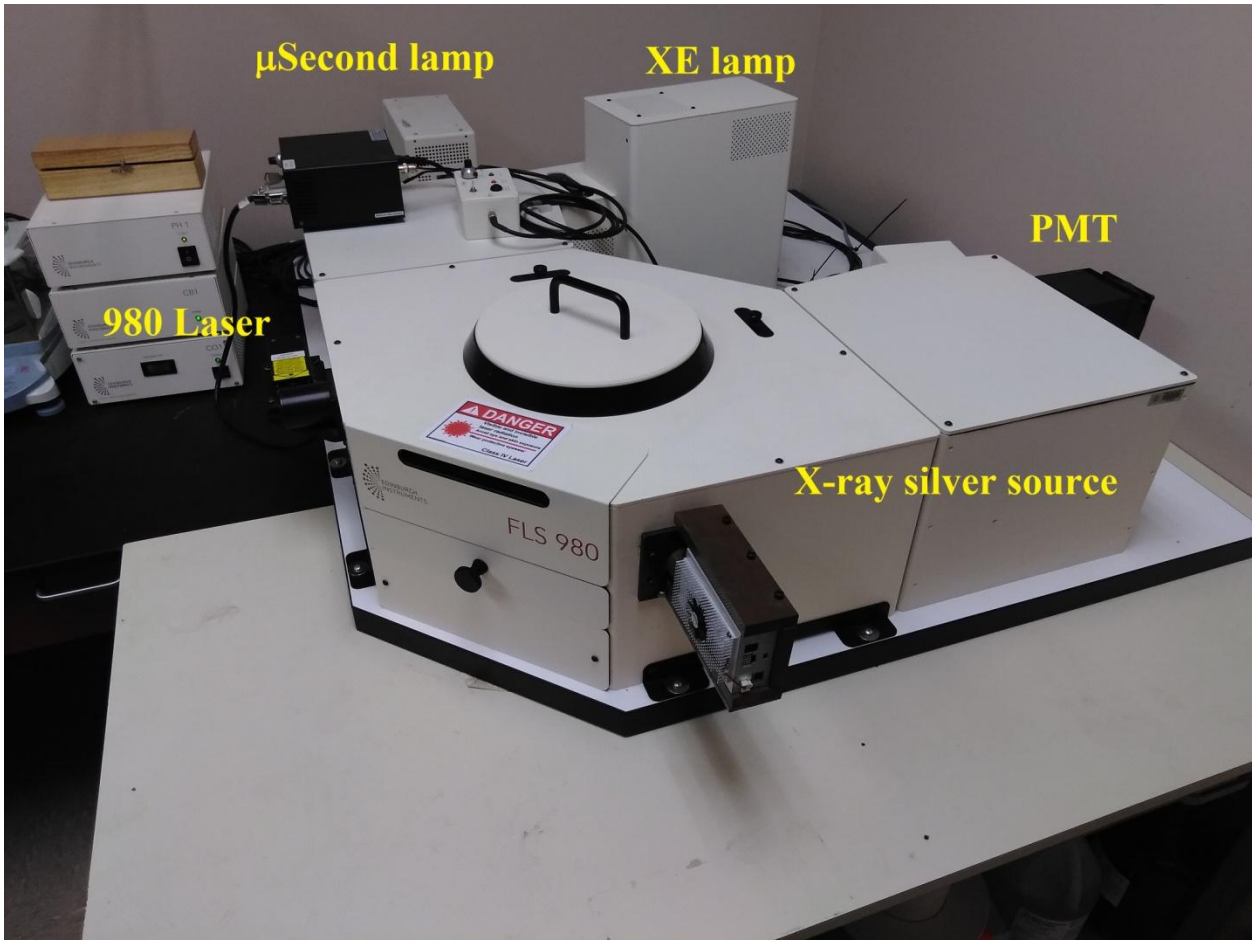

Figure 3.19: Photograph of the FLS 980 fluorescence spectrometer

3.1.16 Diamond Anvil Cell (DAC) for Pressure Dependence Photoluminescence.

In order to investigate how luminescence of certain material behave under pressure, a set up for pressure luminescence had to be design from scratch since we didn't have availability to perform these types of measurements in the past. Figure 3.19 show a photograph of the DAC and all its components that was purchase alongside with a vial of ruby to ensure that the pressure deliver was known using the ruby technique. The components of the DAC involved three screws two 1 carat diamond and pre indented stainless steel gaskets. Figure 3.21 shows the steps taken

to design an effective set up to measure pressure dependence photoluminescence. First, measurements needed to be taken to ensure that the beam would be aligned with the DAC. Here, it was notices that the design used for the DAC was in a 180 degree and our FLS 980 used a 90-degree set up. Meaning that the source of excitation was a 90 degree to the detector PMT. A beam splitter was used to bend the beam of the excitation source an extra 90 degrees and therefore change the direction to 180 degrees to the detector. As seen in figure 3.21(b) a 3-D printed stage was created with the specifics measurements and a hole was drilled to secure the beam splitter into position. The beam splitter can be admired in Figure 3.21(C). Once the beam was aligned with the DAC and the PMT the sample must be mounted into the pre-indented gasket with a hydrostatic fluid. Initially a solution of 4:1 Methanol: Ethanol was used as the hydrostatic fluid; however, the solution was too volatile and partial, or all solution evaporated before the sample was loaded in the DAC and align with the beam. Therefore, silicone oil was used a s a suitable replacement as the hydrostatic fluid. The sample was maneuver with the use of a microscope with the addition of ruby as a reference and pressure sensor. The ruby technique was used to calculate how much pressure was deliver since the spectra of ruby is very well known around 694 nm and shifts to higher wavelength with pressure. The separation between the reference line of ruby and the measure ruby at a specific pressure will determine the accurately the pressure deliver. It was notices that the pressure delivers is sometimes har to manipulate and pressures are not always the same for repetitive experiments. After several turns of the screws the pressure increase exponentially. The recommended operational pressure is in the range of 30 GPa and 40 GPa. Other gasket can be used for higher pressures made of a different material or lower pressures. Figure 3.21 (e) and (f) show the different views of the operational design. On the other hand, Figure 3.22 shows a diagram of the DAC and how it operates when expose to

electromagnetic radiations. The light passes from one diamond to the other to a detector. However, in between there's a gasket with a pre indented hole were the sample and ruby sit with a hydrostatic fluid and become the sample chamber. Hence, the light passes from one end og the diamond through the sample chamber to the other end of the diamond and the emission is recorded with a sensitive detector such a s PMT. Overall, the set up resulted in a successful and effective design to measure pressure dependence photoluminescence and study how material behave under high pressures.

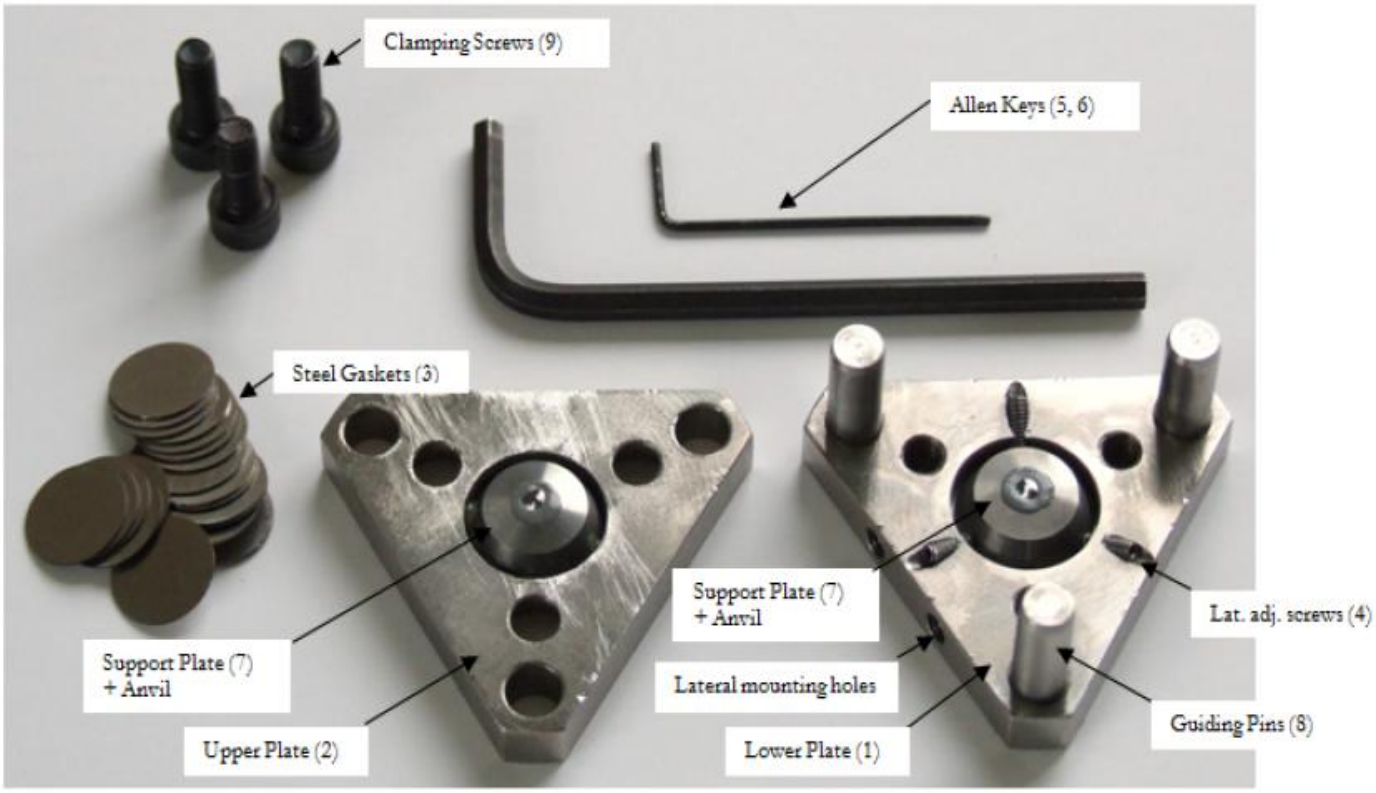

Figure 3.20: Photograph of all the components of the DAC

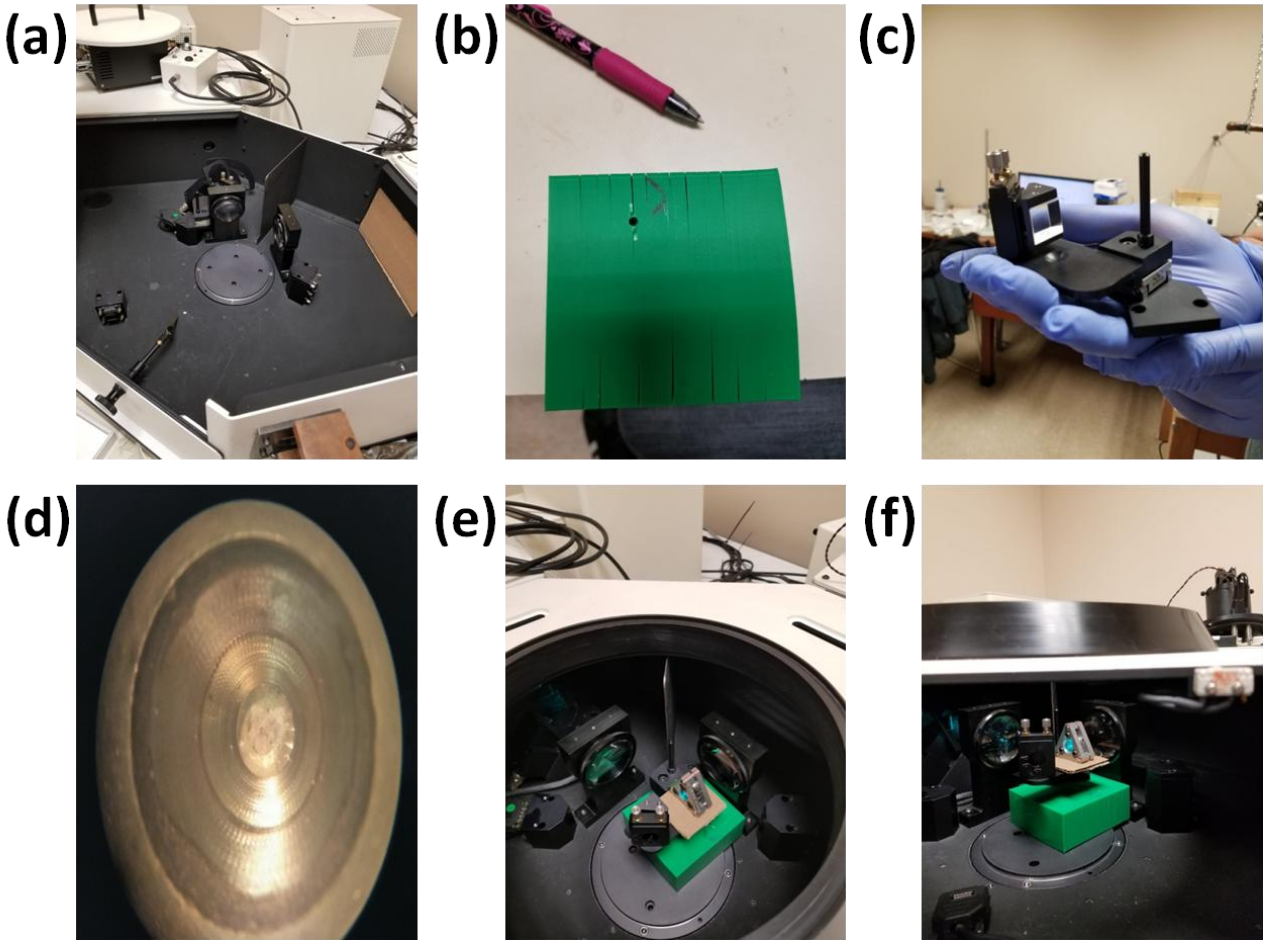

Figure 3.21: (a) Photographs of FLS 980 set up without top cover, (b) 3-D printed staged for the DAC at specifics measurements for proper alignment with the beam, (c) Beam splitter used to redirect the beam to a 90 degreed, (d) properly mounting the sample using 40x microscope, (e) eagle eye view of the final set up for pressure luminescence studies (f) Lateral view of the final set up.

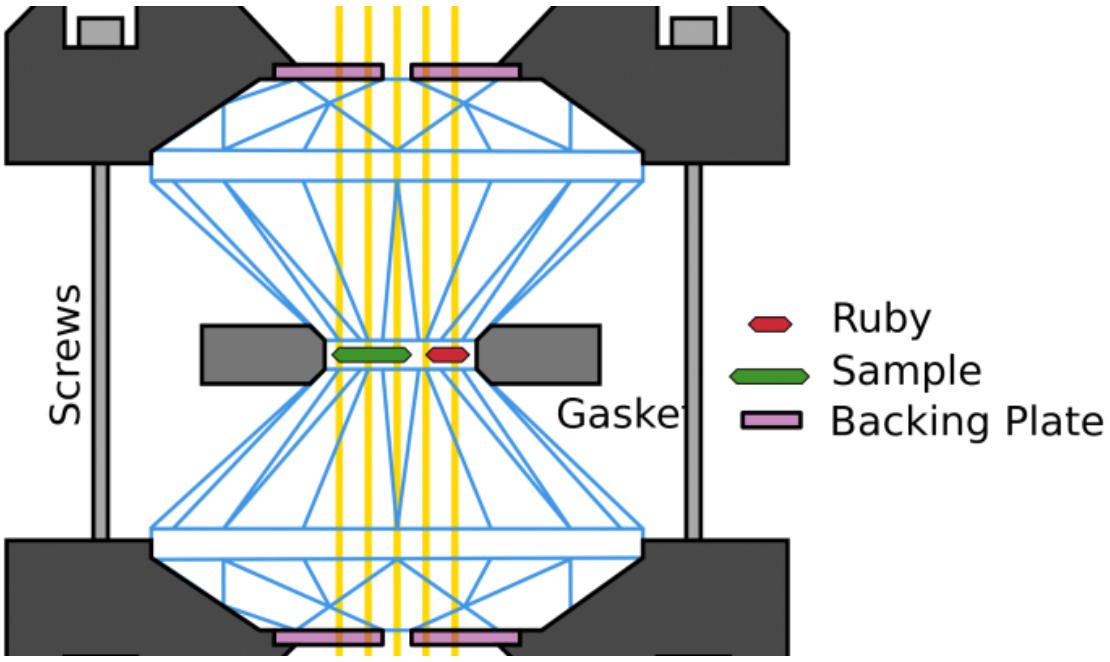

Figure 3.22: Diagram of a DAC in operation when exposed to electromagnetic radiation.(Scully 2016)

3.1.17. Instrumentation: Luminescence Lifetime

Time-correlated single-photon counting (TCSPC) is a well-established and a common technique for fluorescence lifetime measurements, it is also becoming increasingly important for photon migration measurements, optical time domain reflectometry measurements and time of flight measurements.

The principle of TCSPC is the detection of single photons and the measurement of their arrival times in respect to a reference signal, usually the light source. TCSPC is a statistical method requiring a high repetitive light source to accumulate enough photon events for a required statistical data precision. TCSPC electronics can be compared to a fast stopwatch with two inputs (Fig 3.20). The clock is started by the START signal pulse and stopped by the STOP signal pulse. The time measured for one START – STOP sequence will be represented by an

increase of a memory value in a histogram, in which the channels on the x-axis represent time. With a high repetition rate light source, millions of START – STOP sequences can be measured in a short time. The resulting histogram counts versus channels will represent the fluorescence intensity versus time. Generally, one of the inputs to the TCSPC electronics (either START or STOP) will be a pulse generated by a single photon. Single photons can be detected by photodetectors with intrinsically high gain. Most of those photodetectors are photomultipliers or micro-channel plate photomultipliers, but also single photon avalanche photodiodes. For statistical reasons it is important to ensure no more than one single photon event per light flash is detected. Multi-photon events will affect the histogram statistics and will yield to erroneous measurement results. (This is known in literature as the "pulse pile-up problem".) In order to ensure that only one photon per light flash is detected; the photon rate is kept low in comparison to the rate of the exciting lamp; usually 5% or lower.

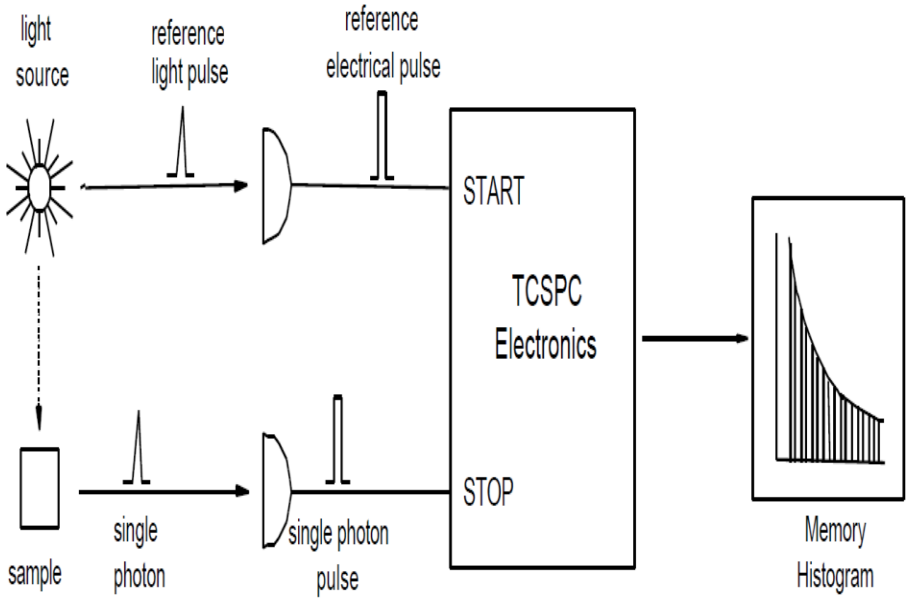

Figure 3.23: TCSPC - A fast stopwatch with two inputs**.**

The main components for signal processing in TCSPC as shown in Figure 3.21 are constant fraction discriminators (CFD), electrical delays (DEL), the Time-to-Amplitude Converter (TAC), Amplifier (between the TAC and ADC), Analogue to Digital Converter (ADC) and digital memory (Mem).

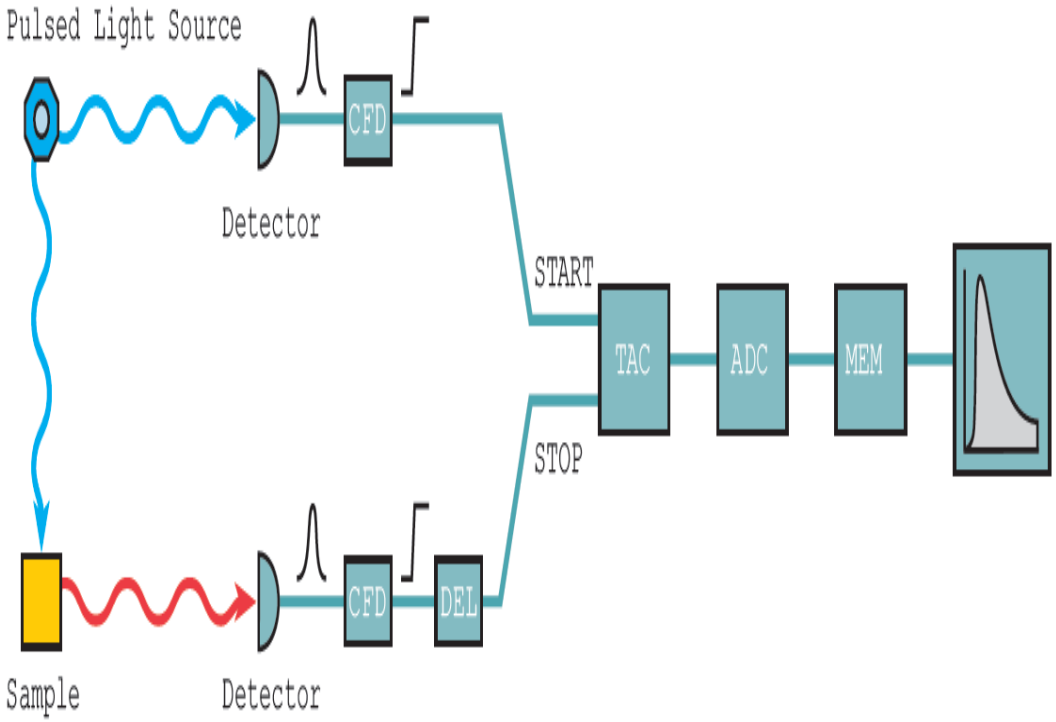

Figure 3.24: The main components for signal processing in TCSPC

At the input of the electronics, incoming pulses are evaluated with respect to pulse height. Only pulses higher than a given threshold will be accepted for further signal processing. Thus, small amplitude noise pulses are readily eliminated. The constant fraction discriminators on both the START and the STOP input then analyses the pulse shape of the individual pulses. The portion of the incoming (generally negative) pulses with the steepest slope on the leading edge is taken as a criterion for the temporal position. Which portion of the slope is taken will depend on the fraction, the constant fraction delay (or shaping delay), and the zero-crossing level.

Threshold, fraction, constant fraction delay, and zero crossing level will depend on the type of detector used and need to be matched to the individual detector. At the output of the CFD pulses are re-shaped to a standard height and shape. They then can be delayed by an electronic shifting delay. This delay will later result in a left or right shift of the entire measurement on the time axis. The TAC is the fast clock, started by the START and stopped by the STOP pulse. The START pulse initiates the growth of a ramp signal. Depending on the arrival time of the STOP pulse the ramp will have a lower or higher height. Once the growth of the ramp has been stopped, the level will remain constant for a defined period. The TAC output pulse can then be amplified, thus effectively stretching the time axis. Minimum and maximum available (amplified) TAC amplitude determine the time range. The amplified TAC output pulse is effectively an analogue pulse of a height corresponding to a measured time of a single START – STOP sequence. For further processing the pulse height will be measured by a digital pulse height measure devise, the ADC. The ADC resolution determines how many discrete time values are possible. All possible measured TAC pulse amplitudes will therefore put into different time bins. The width of the time bin is the ratio of the full-time range and the resolution of the ADC in channels. It is the time resolution, usually given in picoseconds / channel or nanoseconds / channel.

CHAPTER IV

MOLTEN-SALT METHOD AS A SUITABLE TEHNIQUE FOR SYNTHESIZING NANOPARTICLES

4.1.1. Introduction to Molten-Salt Method

Molten-salt synthesis (MSS) involves the use of a molten salt as the reaction medium for preparing nanomaterials from their constituent precursors. The molten salt acts as the solvent and facilitate the enhanced reaction rate by increasing the contact area between reactants and their mobility. The choice of molten salts is of paramount importance for the success of the MSS method. They must meet some important quality requirements such as low melting point, compatibility with reacting species, and optimum aqueous solubility. Molten salt has been used before to enhance the rate of solid-state reactions. However, in a flux system, only a small amount of molten salt is used, unlike the MSS where large quantity of salt is added to form a soluble medium for the reaction and control the properties of the synthesized nanomaterials, such as particle size, shape, and crystallinity, etc. In this sense, MSS is a modification of the powder metallurgical method and different from the flux method.(Kimura 2011, Mao et al. 2005, Mao et al. 2010) The employment of molten salt can (1) increase reaction kinetic rate(Mao et al. 2009a) while decreasing synthesis temperature(Yu et al. 2018), (2) increase the degree of reactant homogeneity(Liu et al. 2013), (3) control crystalline size and morphology(Chang et al. 2017), and (4) reduce the level of agglomeration.

Nanomaterials have been in high demand in scientific research and novel industrial applications because of their superior electrical, chemical, magnetic, optical, electronic and thermal properties. Their properties are highly dependent on the particle size crystallinity. Compared with other synthesis methods for nanomaterials, MSS has several obvious advantages even though it is not yet as well-known as other synthesis methods in the nanoscience and nanotechnology community. As described below, these advantages include its simplicity, reliability, scalability, generalizability, and environmental friendliness, cost effectiveness, relative low synthesis temperature, and free agglomeration of NPs with clean surface, etc.(Mao et al. 2007a)

4.1.2. Simplicity of MSS

The MSS process can be easily carried out in a simple laboratory with basis facility. No sophisticated instrumentation is needed. Precursors and molten salts are air stable with no need for glove box handling.

4.1.3. Reliability of MSS

Once all initial synthesis parameters such as concentration, pH, processing time, and annealing temperature, etc. are optimized, one is sure to make high quality and pure products by the MSS method. If one carries out all synthesis steps properly, the final products could attain all basic criteria needed for good quality NPs. A novice to the MSS method does not change the synthesis outcome if s/he follows all synthesis parameters properly and carefully.

4.1.4. Scalability of MSS

The MSS method’s ability to produce large quantities of size- and shape-controlled particles is crucial. This critical factor is important because it allows for the determination of

industrial usefulness and efficiency. Compared to other synthesis techniques, it can easily generate enough products by adjusting stoichiometric amounts during the MSS synthesis. This is an important feature of the MSS method because it allows for convenience at the industrial level, shape and making it a more desired approach due to its scalability.(Liu et al. 2014, Yuanbing Mao et al. 2003)

4.1.5. Generalizability of MSS

The MSS method is also a generalizable technique to make nanoparticles with various compositions. Other than simple metal oxides and some fluorides, nanomaterials of complex metal oxides which have been successfully synthesized by the MSS method include perovskites (ABO_3)(Mao 2012, Hailili et al. 2018, Yuanbing Mao et al. 2003, Yuanbing Mao 2013, Mao and Wong 2005), spinel (AB_2O_4)(Rojas-Hernandez et al. 2015, Reddy et al. 2015), pyrochlore ($A_2B_2O_7$)(Zuniga et al. 2018b, Mao et al. 2009a, Pokhrel et al. 2016b, Wahid et al. 2017b) and orthorhombic structures ($A_2B_4O_9$)(Park et al. 2005, Mao et al. 2005, Mao et al. 2010). More specifically, these nanomaterials include ferrites, titanates, niobates, mullite, aluminium borate, wollastonite and carbonated apatite.(Chang et al. 2017, Gilbert 2016, Liu et al. 2014) The MSS method has also been used to produce nanomaterials of various morphologies such as nanosphere(Mao et al. 2009a), ceramics powder bodies(Huang et al. 2016b), nanoflakes(Huang et al. 2016a), nanoplates(Chang et al. 2017), nanorods(Wang et al. 2017b), and core-shell nanoparticles (NPs)(Pokhrel et al. 2017) depending on synthesis conditions and crystal structure of the products.

4.1.6. Environmental Friendliness of MSS

Several traditional methods for making nanomaterials involve the use of large amounts of organic solvents and toxic agents that generate environmental issues. The partial or total elimination of the use of them and the generation of waste by sustainable processes is in demand of green chemistry nowadays.(Mao et al. 2007a) The MSS method is an environmentally friendly approach to synthesize nanomaterials by employing nontoxic chemical and renewable materials and minimizing waste, byproducts and energy.

4.1.7. Relative Low Synthesis Temperature

The processing temperature of the MSS method is relatively low compared to that required in a conventional solid-state reaction(Ramesh et al. 2010) and sol-gel combustion reaction.(Gupta et al. 2016k) It saves energy during the low temperature approach while producing high quality NPs.

4.1.8. Cost Effectiveness

The MSS method does not require any harsh or costly reactants or solvents nor any specialized instrumentation. Water is the main solvent used for washing away the used molten salts, which are also cheap. Moreover, experimental setup needed includes only simple glassware and furnace without specialized instrumentation while nanomaterials with complex composition and refractory nature could be produced.

4.1.9. Agglomeration Free with Clean Surface

During the MSS process, the formed nanoparticles are well-dispersed in the molten salt medium due to its large quantity used along with its high ionic strength and viscosity.(Mao et al.

2007a, Kimura 2011, Liu et al. 2013) Unlike colloidal synthesis and most hydrothermal/solvothermal processes, no protective surface layer is necessary to prevent the continuous growth and agglomeration of the formed NPs.

4.1.10. Exemplary Synthesis of Complex Metal Oxide NPs by the MSS Method

The MSS method as a universal and cost-effective approach to rationally and large-scale synthesize nanomaterials for a sufficiently wide spectrum of material is highly welcomed by scientists working in nanoscience and nanotechnology. Here, lanthanum hafnate $La_2Hf_2O_7$ is selected because of its multifunctional applications in the areas of X-ray imaging, high *k*-dielectric, luminescence, thermographic phosphor, thermal barrier coating, and nuclear waste host. $La_2Hf_2O_7$ is also a good host for doped scintillators due to its high density, large effective atomic number, and the possibility of its crystal structure to be engineered along with an order-disorder phase transition. It belongs to $A_2B_2O_7$ family of compounds (where A is a rare-earth element with +3 oxidation state, and B represents a transition metallic element with +4 oxidation state). However, due to the refractory nature and complex chemical composition, there was the lack of proper low temperature and large-scale synthesis method for $La_2Hf_2O_7$ NPs.

For fundamental scientific investigation and advanced technological applications, it is a prerequisite to make monodisperse, high quality and uniform $A_2B_2O_7$ NPs. Here we use the synthesis of highly crystalline $La_2Hf_2O_7$ NPs as an example to demonstrate the advantages of the MSS method. As schematically shown in Figure 4.1, $La_2Hf_2O_7$ NPs were prepared by the MSS method with a two-step process following our previous reports. First, a single-source complex precursor of $La(OH)_3 \cdot HfO(OH)_2 \cdot nH_2O$ was prepared via a coprecipitation route. In the second step, size-controllable $La_2Hf_2O_7$ NPs were synthesized through the facile MSS process using the

single-source complex precursor and nitrate mixture ($NaNO_3$:KNO_3 = 1:1, molar ratio) at 650^{o}C for 6 h.

4.1.11. Controlling Factor of the MSS Method

The chart in Figure 4.2 provides several reliable controlling factors of the MSS method and accounts for alternative pathways to fine-tune the features of synthesized nanomaterials. In addition, it helps identify critical steps essential in the MSS process.

First, the identity of precursors is critical, especially for the synthesis of complex metal oxide NPs. For making $A_2B_2O_7$ NPs, it is very important to first generate a single-source complex precursor which contains the main elements that make up the final product, i.e. A and B, at an atomic level with the formula of $A(OH)_3 \cdot BO(OH)_2 \cdot nH_2O$. In our example, the particle size of the final $La_2Hf_2O_7$ NPs could be controlled in this step by adjusting the concentration of the titrant ammonia solution, where higher ammonia solution concentration generates bigger $La_2Hf_2O_7$ NPs. Other trials have also been performed to make $A_2B_2O_7$ NPs using different precursors, such as commercially available nitrates or oxides containing the main elements of $A_2B_2O_7$, but none of them worked[4]. The advantages of this amorphous single-source complex precursor is that the composing elements of $A_2B_2O_7$ are mixed at an atomic level, and are homogeneously distributed in the same order as the final $A_2B_2O_7$ product, decreasing the space or range the reactants need to be transported.

Second, the selection of proper molten salt has major importance to obtain nanomaterials with desirable morphology and characteristics. The melting point of the selected salt should be appropriate for the synthesis of the required phase of nanomaterials. The formation of nanomaterials is ultimately govern by the melting point of salts used as molten solvents such as

alkali chloride, sulfate, carbonate or hydroxide(Ozen et al. 2017, Kimura 2011, Liu et al. 2013)'(Kimura 2011, Fazli et al. 2013). It has been reported that the use of different molten salts can modify the formation temperature and thereby altering the particle size and morphology.(Pokhrel et al. 2016b)

In addition, the ramp rate tends to affect the synthesis of the NPs. A fast ramp rate tends to generate agglomerated NPs,(Bortolani and Dorey 2010) which affect their properties. In case of luminescent and scintillation material, high agglomeration is not desirable as it can scatter excited and emitted light.(Zuniga et al. 2018b, Wahid et al. 2017b) A slow ramp rate is more suitable and allows enough time to reach actual temperature inside the crucible. A slow cooling process usually allows NPs with spherical shape to form.(Zhou et al. 2007)

There is another important criterion for the selection of the salt: the salt should have enough aqueous solubility. With simple washing by water, the used molten salt should be easily washed away after the MSS.

Finally, the addition of a volatile liquid such as acetone and ethanol during the mixing of the salts used and the single-source complex precursor helps ease the grinding process but is not essential. The addition of a liquid is helpful to make a homogenous mixture in shorter time and less effort, which is important to generate pure products. The added volatile liquid does not affect the characteristics of the resultant NPs since it fully evaporates by the end of the grinding process. Due to its high volatility, the amount added could range anywhere from 1 mL to 5 mL.

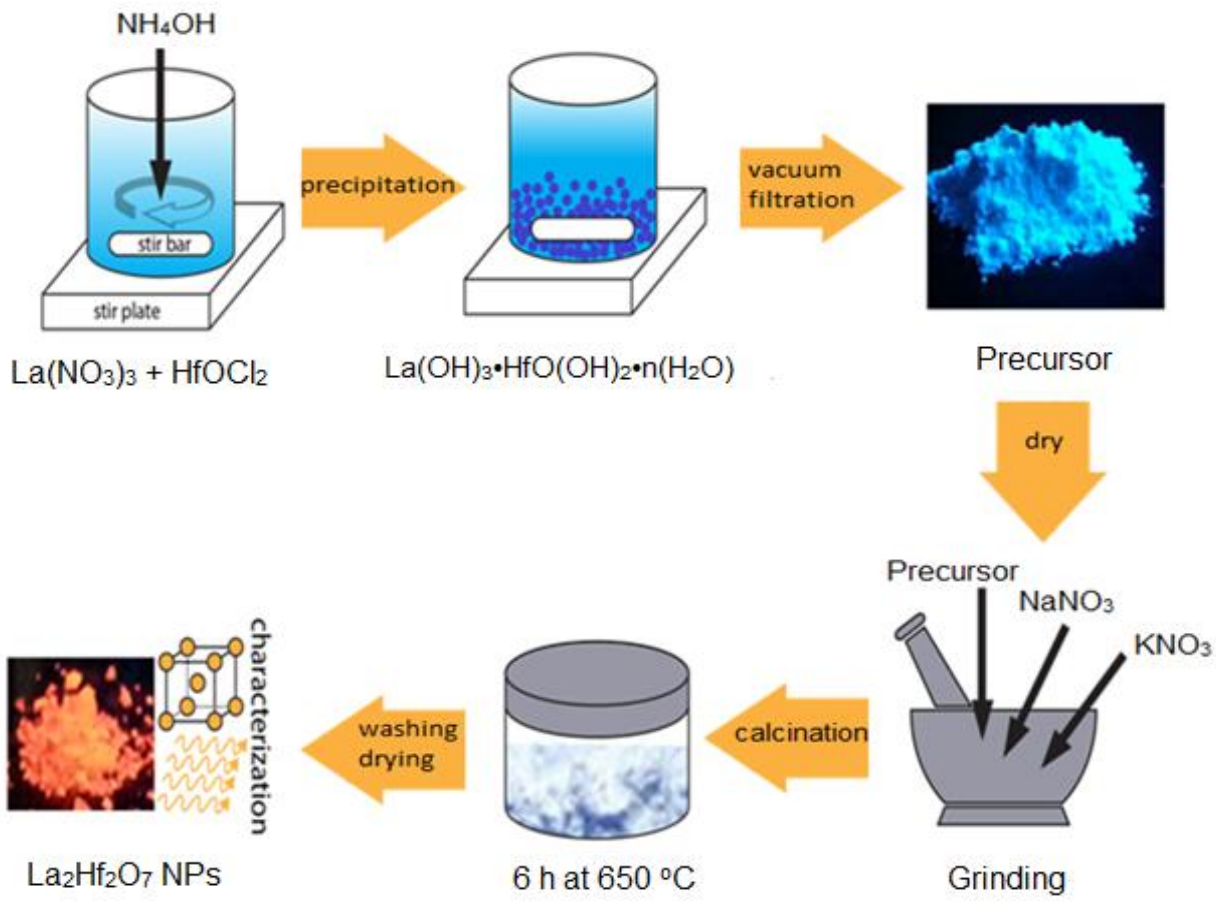

Figure 4.1: Schematic of the synthesis steps for $La_2Hf_2O_7$NPs via the MSS method. (Zuniga et al. 2018)

4.1.12. Modifications and Troubleshooting of the MSS Process

The MSS method is straightforward and simple way to synthesize NPs at any university and industry. However, modifications of the protocol can be made. For example, in case a vacuum filter system is not available, the single-source complex precursor obtained from the coprecipitation step can be centrifuged. Different eutectic salt mixtures can be used to engineer NPs with desired characteristics.

4.1.13. Limitations of the MSS Method

Even though the MSS method is generally easy to be employed, limitations which can occur include: (1) The possibility of the product formation is limited by the area of contact of the dissimilar reactants in the reaction(Kimura 2011). (2) Not every nanostructured product can be formed within selected molten salts. The cases are rare, but could certainly happen.(Kimura et al. 1983) It is desirable that the selected salts act only as pure solvents and do not react with the reactants or the products. Furthermore, common mistakes that could hinder the quality of the final product involved covering the burette during the titration changing the concentration of the ammonium hydroxide which will change particle size. In addition, another common mistake is not allowing the precipitation to form during a period of two hours. By adding the titrant at a faster rate the kinetics of the reaction changes which might cause unwanted complex precursor. Finally, if one is not careful in the grinding process and the final mixture is not as fine as possible the resultant product made yield larger particles.

4.1.14. The Significance of the MSS Method with Respect to Existing/Alternative Methods

The MSS method is simplistic, effective, fast, low temperature, and cost efficient as proved with many reported results compared with conventional solid-state and sol–gel/combustion synthesis methods.(Gupta et al. 2016k) It is also scalable, reliable, and generalizable to make agglomeration-free NPs without surface protective layer, unlike the colloidal and hydrothermal/solvothermal synthesis methods.

4.1.15. Future Applications or Directions of the MSS Method

The application of the MSS method has widely spread in the last couple of decades from ferroelectric and ferromagnetic materials to materials for Li-ion batteries(Liu et al. 2017),

semiconductors(Huang et al. 2010, Zuniga et al. 2018b), phosphors(Wahid et al. 2017b, Zuniga et al. 2018b) and electro-catalysts,(Ahmed and Mao 2016a, Ahmed and Mao 2016b) mainly for nanosized materials, especially those with complex compositions. In conclusion, the MSS method provides a suitable pathway in the synthesis of simple and complex metal oxide NPs. It is expected that the MSS method will become an even more popular synthesis method for nanomaterials and be more widely employed in the nanoscience and nanotechnology community in the upcoming years.

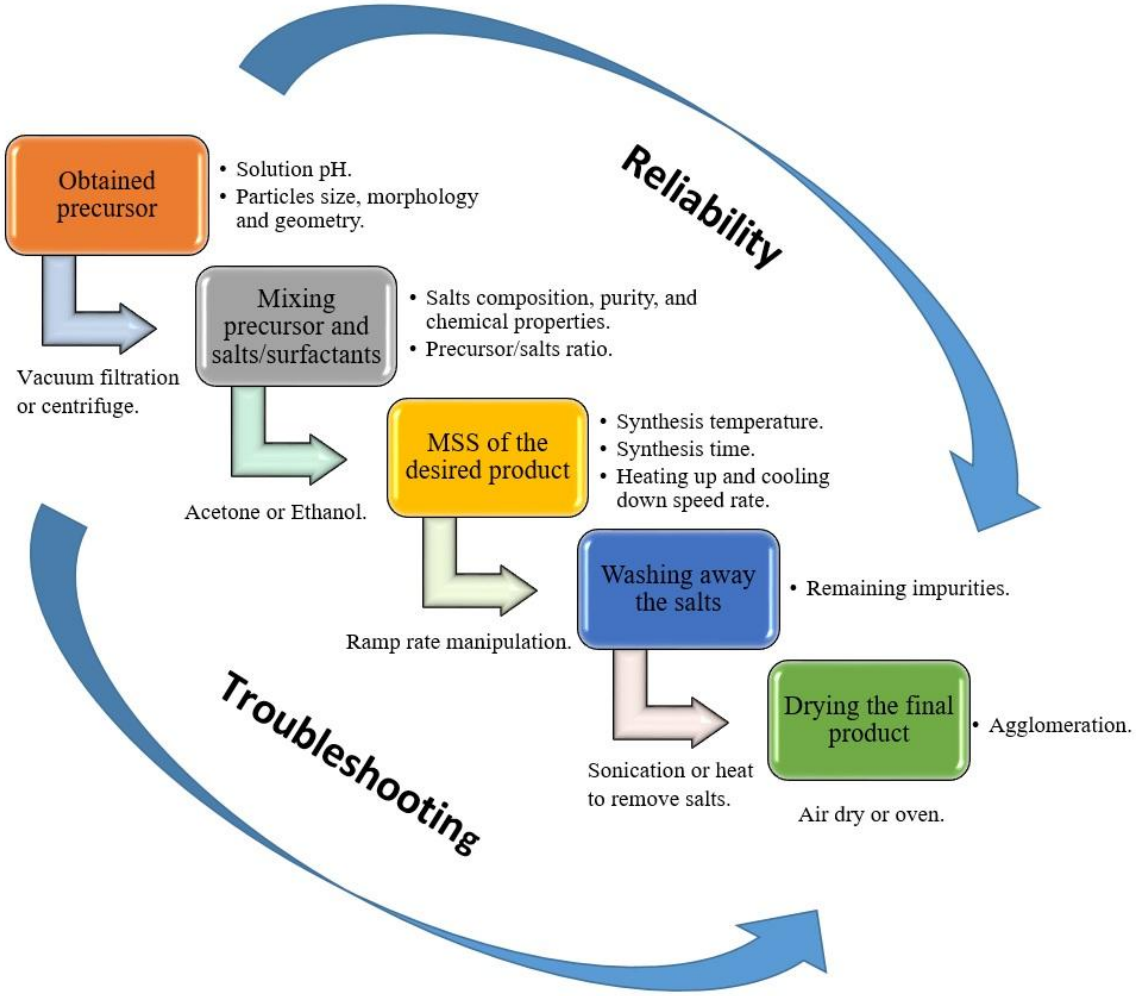

Figure 4.2: Flowchart of the critical steps of MSS indicating the controlling factors of the synthetic procedure for NPs with potential pathways to fine-tune their characteristics.

CHAPTER V

OPTIMIZATION OF SYNTHESIS PARAMETERS

5.1.1 Adjusting the NH_4OH Concentration in the Formation of the Single Source Complex Precursor

During this step we first needed to ensure that all parameters were optimized before moving on to engineering the most optimum nanophosphor for scintillation, white light LEDs, and nuclear waste immobilization. Here we adjusted the NH_4OH concentration of the titrant during the co-precipitation step of the molten-salt synthesis. This optimization allowed us to modify the final particle size without adjusting the time and temperature during the molten-salt process. The concentration was adjusted by changing the final molarity of the concentration in the range of 0.75% to 7.5%. This change the way the single source complex precursor was made and modify the structural and optical properties of the resultant nanophosphors. It was found that the modification of concentration did not rearrange the structural lattice of the nanoparticles, however it tunes the size. As the concentration of NH_4OH increase the particle size increase proportionally. In figure 5.1 it shows a representative HRTEM image of the 7.5% $La_2Hf_2O_7$ nanoparticle showing no change of the lattice. The $La_2Hf_2O_7$ nanoparticles were mostly sphere shaped and had the average diameter of approximate 10-12 nm. The FT image illustrated the lattice planes in two different sized nanoparticles, showing an interplanar spacing of approximate 3.125 and 3.202, which corresponds to the (222) and (311) plane of order pyrochlore $La_2Hf_2O_7$. In addition, the purpose of this study is to investigate the physicochemical factors that will leads to the improvement in the optical properties of $La_2Hf_2O_7$ NPs. Figure 5.2 (a) shows the emission

spectra of $La_2Hf_2O_7$ nanophosphors prepared with various pH of solution (change in concentration of NH_4OH solution), after excitation at 306 nm. It can be seen from the Figure 5.2 (b) that emission intensity increase with increase in pH initially and thereafter decreases. The powder sample prepared with 1.5 % ammonium hydroxide solution (1.5%, pH=12.1) display maximum violet blue emission intensity which is related to its optimum particle size, surface area and crystallinity. From 0.75% to 1.5% particle size increases but surface area decreases. Small surface area brought less surface defect and thereby probability of non-radiative relaxation decreases which leads to more emission intensity(Zhang et al. 2008, Tong et al. 2016). As the pH is further, increase although the surface defect is decreased the effect of hydroxyl ions incorporation predominates the decrease in surface defect. Hydroxyl ion are known to provide additional pathways for non-radiative relaxation and therefore emission intensity decreases(Luwang et al. 2010). The luminescence lifetime decay profile for $La_2Hf_2O_7$ nanophosphors prepared with various pH is shown in Figure 5.2 (c). The lifetime value doses not change much with the value of 9.6 ms for 0.75% and 1.5% where there is slight enhancement to 10.0 ms for 3% to 0.75% samples. As a function of pH; there is a spectral shift too observed in the emission spectra of lanthanum hafnate nanoparticles that leads to slight change in color emitted by $La_2Hf_2O_7$ nanophosphors. The CIE index diagram shown in Figure 5.2 (d) clearly show that color emitted by the NPs changes slightly in domain of bluish-indigo to bluish violet from 0.75% to 7.5%. This study projects a probable way to making color tunable nanophosphors simply by changing pH.

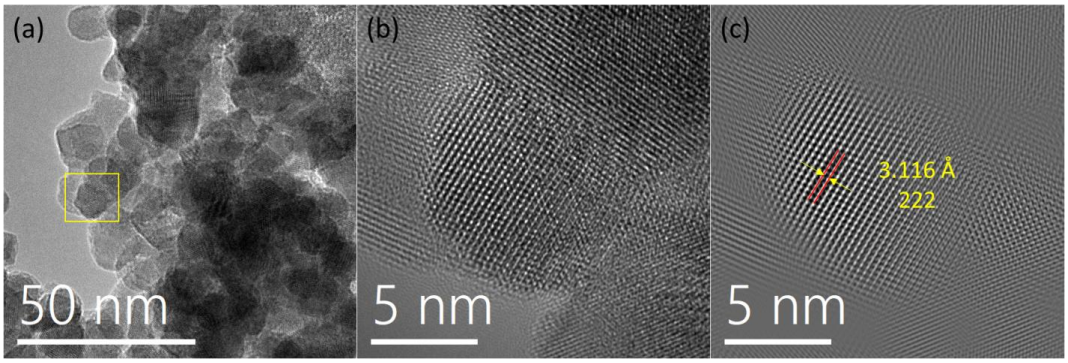

Figure 5.1: Representative HRTEM micrographs of $La_2Hf_2O_7$ NPs (S10) and corresponding Fourier Transformed images of two different particle

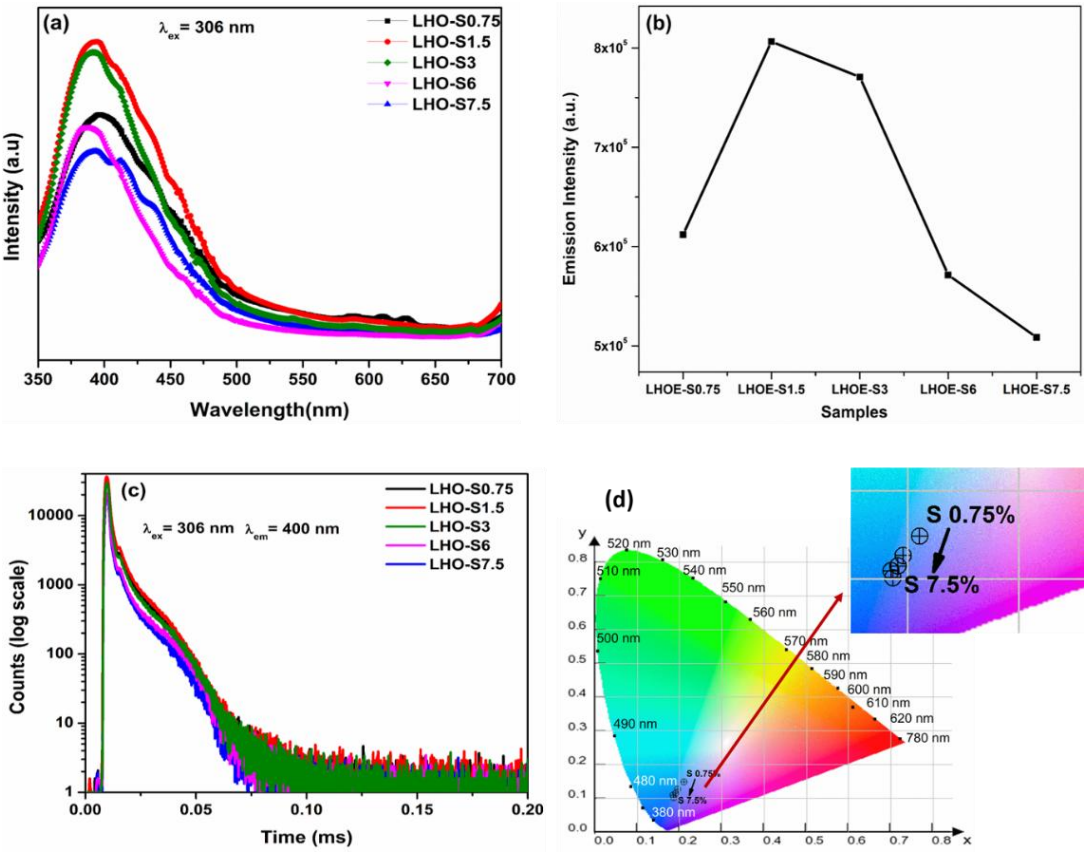

Figure 5.2. (a) Emission spectra taken at λ_{ex} = 306 nm, (b) corresponding emission intensity variation with different [NH_4OH] used, (c) PL decay profiles taken at λ_{ex} = 306 nm and λ_{em} = 396 nm, and (d) CIE color coordinate diagram of the $La_2Hf_2O_7$ NPs co-precipitated at various pH values. Inset of 4(d) shows the magnified CIE coordinates of the LHO NPS.

Overall, we correlated the structure and luminescence of undoped and Eu^{3+}-doped $La_2Hf_2O_7$ NPs. The undoped $La_2Hf_2O_7$ NPs emit violet-blue color on ultraviolet irradiation. Extent of ordering in pyrochlore network increases as the pH is raised and indeed, at lower pH the $La_2Hf_2O_7$ NPs still have some lattice disordering. The color emitted by the bare NPs changes slightly in domain of bluish-indigo to bluish violet from lower to higher pH (LHOE-S0.75→LHOE-S7.5). DFT based density of state calculations showed origin of defects sates in the electric band-gap due to charged oxygen defects. The optimum luminescence efficiency for both undoped and doped sample was found for the sample with 1.5 % NH_4OH owing to it optimum crystallinity, low agglomeration, low hydroxyl ion concentration and low surface defects. On doping europium in LHO host, an efficient host to dopant energy transfer takes place, which is explained based on DFT calculation. Moreover, our DFT calculated DOS shows Eu doping in LaO_8 site lifts the degeneracy between majority/minority spin components and Eu-f states preset at the defect energy levels in both majority and minority spin components. Therefore, origin of most intense peaks at 613 nm and 630 nm in Eu^{3+}-doped-$La_2Hf_2O_7$ is mediated through Eu-f states present at charged oxygen defect states in the electronic band-gap and Eu-d states present at valence band. Based on DFT it is also proposed that europium is energetically more stable at LaO_8 site that is responsible for its highly asymmetric environment in LHO host. The high quantum yield, high excited lifetime, exhibiting intense RL, high thermal stability highlighting the potential of the synthesized NPs for advance optoelectronic, radiation detection and bio-imaging applications. Figure 5.3. shows the summary of this work.

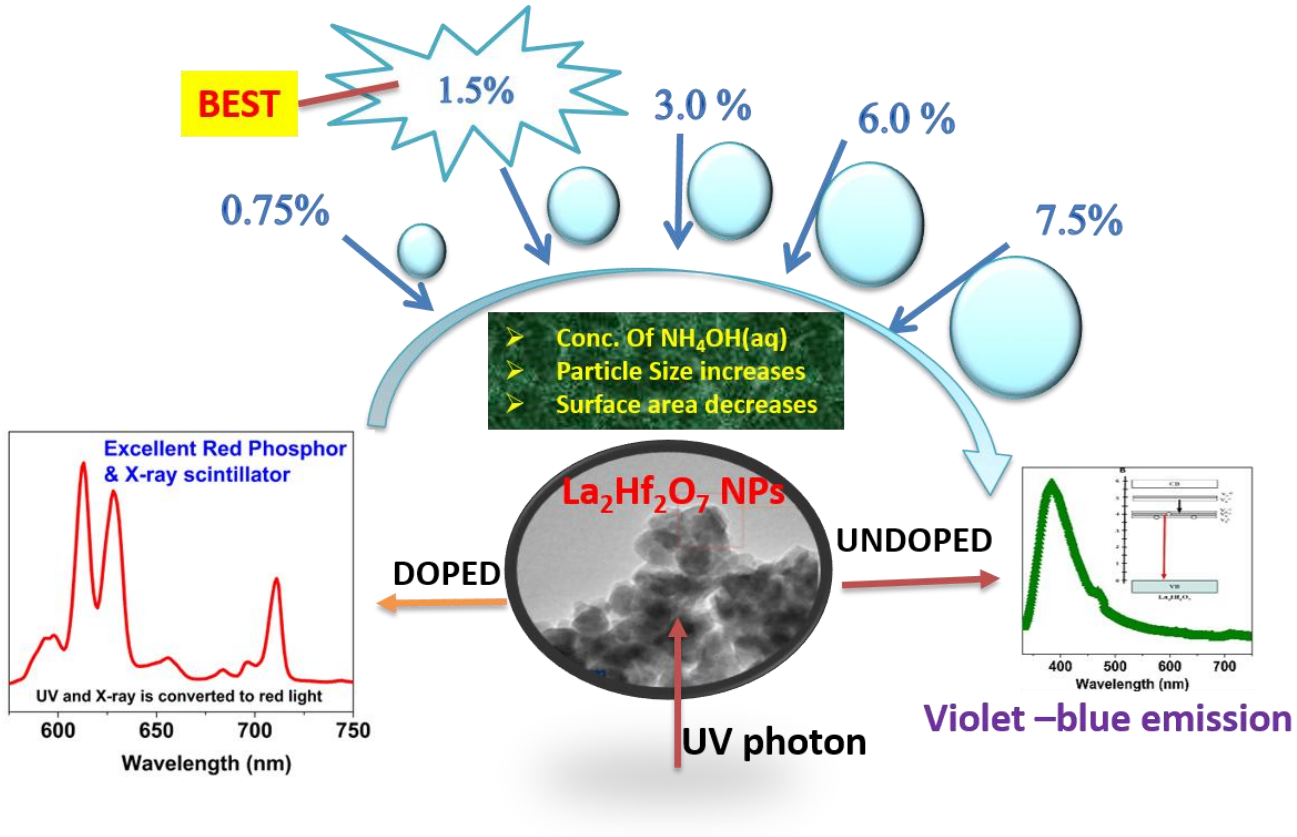

Figure 5.3. Summary of pH dependent effect on structural and optical properties of LHOE.(Gupta et al. 2018d)

5.1.2 Adjusting Processing Time in the Molten-Salt Synthesis.

In this study, we have correlated the changes in optical properties of europium doped lanthanum hafnate $La_2Hf_2O_7:Eu^{3+}$ NPs synthesized by an environmentally-friendly MSS method as a function of processing duration with Judd–Ofelt parameter and other related photophysical parameters(Mao et al. 2007b). Judd-Ofelt analysis was carried out to decipher various photophysical information, such as radiative and non-radiative transition rates, quantum efficiency, Judd-Ofelt parameters, branching ratio, etc. In addition, systematic studies were carried out to explore the potential applicability of these $La_2Hf_2O_7:Eu^{3+}$ NPs as phosphor materials. The focus was to synthesize highly efficient red phosphors for multifunctional applications which can get excited by UV light (mid and near UV), blue LEDs, green LEDs, and

X-ray. We have also explored the effect of MSS processing duration of these NPs on their X-ray excited optical luminescence for the first time.

Commercial red phosphors for near ultra-violet (NUV) based white light emitting diodes (WLED) are excited by NUV or blue LEDs. Based on the Laporte selection rules, the intra f-f transitions are forbidden in nature, therefore Eu^{3+}-based phosphors have poor absorptivity in near ultraviolet/blue region as a result they exhibit weaker emission under similar excitation. Because the excitation spectra of our samples are very rich in near, mid and far UVs as well as blue and green regions, they exhibit intense red emission corresponding to the $^5D_0 \rightarrow {}^7F_2$ transition of Eu^{3+} ions under excitations by far UV (at 200 nm), mid UV (at 265 nm), near UV (at 393 nm), blue light (at 463 nm), and green light (at 534 nm) (Figure 5.4). Such intense red emitting NPs can be explored for white LEDs based on phosphor-converted LEDs (pc-LEDs) wherein blue LEDs is combined with red and green phosphor.

By correlating the asymmetry ratio with the particle size/surface defects of our $La_2Hf_2O_7$:Eu^{3+} NPs, there are two ways to investigate this phenomenon. Highest asymmetry ratio from the LHOE-3h sample suggests highly asymmetric local environment around the Eu^{3+} ions compared to other LHOE samples. Therefore, Laporte's selection rules are more relaxed for the LHOE-3h sample compared to the other samples, which means higher transition probability as well as oscillator strength for f-f transition leading to enhanced emission output.(Gupta et al. 2018a) Secondly, in terms of size/surface defects, this phenomenon can also be explained. The LHOE-3h sample has minimal surface defect and least agglomeration that favor high radiative transition and low scattering of excited and emitted light respectively leading to high luminescence output.(Gupta et al. 2016m, Wang et al. 2007b) The PL emission enhancement up to 3h MSS processing duration can be ascribed to reduction in non-radiative pathways as a result

of reduction in surface defects with increased particle size. Beyond 3h MSS processing duration, the $La_2Hf_2O_7$:5%Eu^{3+} NPs tends to agglomerate, which may cause scattering of the emitted light, and therefore reduction in emission intensity. These observations could be explained based on our SEM results. Figure 5.5 is the schematic showing the progressive increase in particle size as the MSS processing duration is increased, which reflects increased particle size but reduced surface defects.

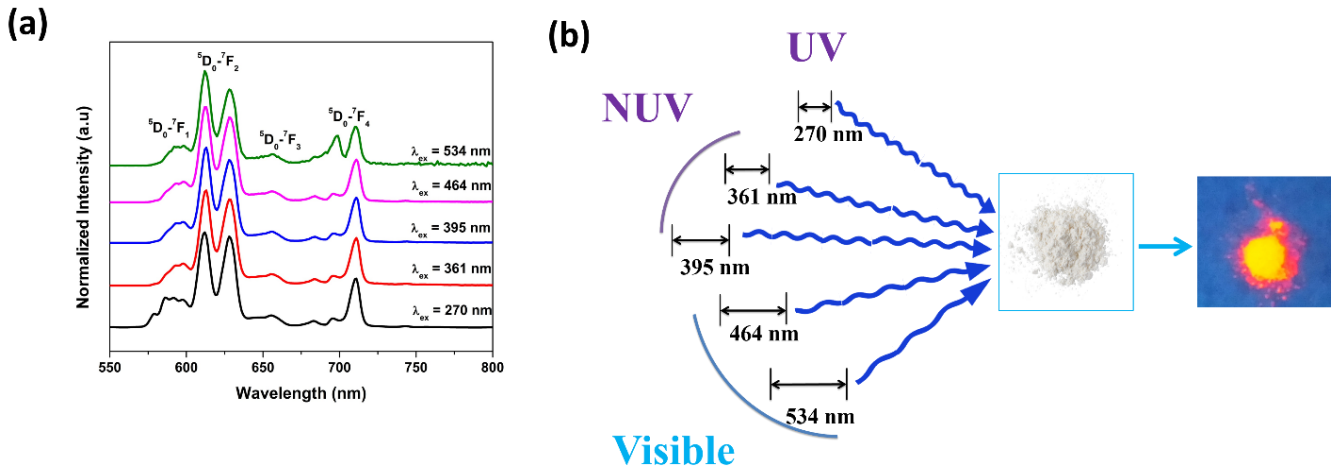

Figure 5.4: (a) Emission spectra and (b) schematic of the LHOE-3h NPs under various excitations, including far UV, mid UV, near UV, blue light, and green light.

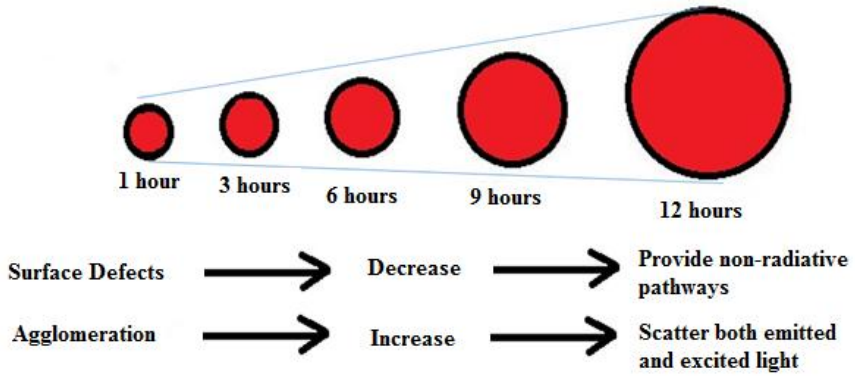

Figure 5.5: Schematic showing the particle size increase of the $La_2Hf_2O_7$:5%Eu^{3+} NPs as the function of the MSS processing duration.

In summary, we demonstrated that the europium-doped lanthanum hafnate ($La_2Hf_2O_7:Eu^{3+}$) nanoparticles with an ordered pyrochlore phase structure could be successfully prepared at 650^oC by a molten-salt synthesis method for various durations. The emission output and quantum yield were found to be the highest for the MSS processed sample for 3h owing to its least surface defect and least agglomeration. Emission spectrum revealed predominant asymmetric environment of Eu^{3+} ions with large spectral splitting and presence of forbidden $^5D_0 \rightarrow {}^7F_0$ transition. Optical purity of red emission was also very high for the LHOE-3h NPs due to the least contribution among all of the LHOE samples from orange emission at 593 nm as seen from the branching ratio calculations. The large spectral splitting could be seen in reduction of point group symmetry from D_{2d} to C_{4v} because of the created lattice strain and distortion due to the localization of the Eu^{3+} ions at La^{3+}/Hf^{4+} sites. The synthesized nanoparticles displayed unique ability to emit bright red light under far UV to green light excitations. These $La_2Hf_2O_7:Eu^{3+}$ nanoparticles were further explored for their applications as radioluminescent phosphors. Interestingly, the synthesized $La_2Hf_2O_7:Eu^{3+}$ NPs can convert highly energetic X-ray into red light which highlights its suitability for X-ray scintillators. Our results indicate the important role of the molten salt synthesis processing duration plays in optimizing nanophosphors for optoelectronic applications. This work opens a new pathway for people to optimize the molten salt synthesis conditions suitably for getting highly efficient luminescent materials for phosphor and scintillator applications.

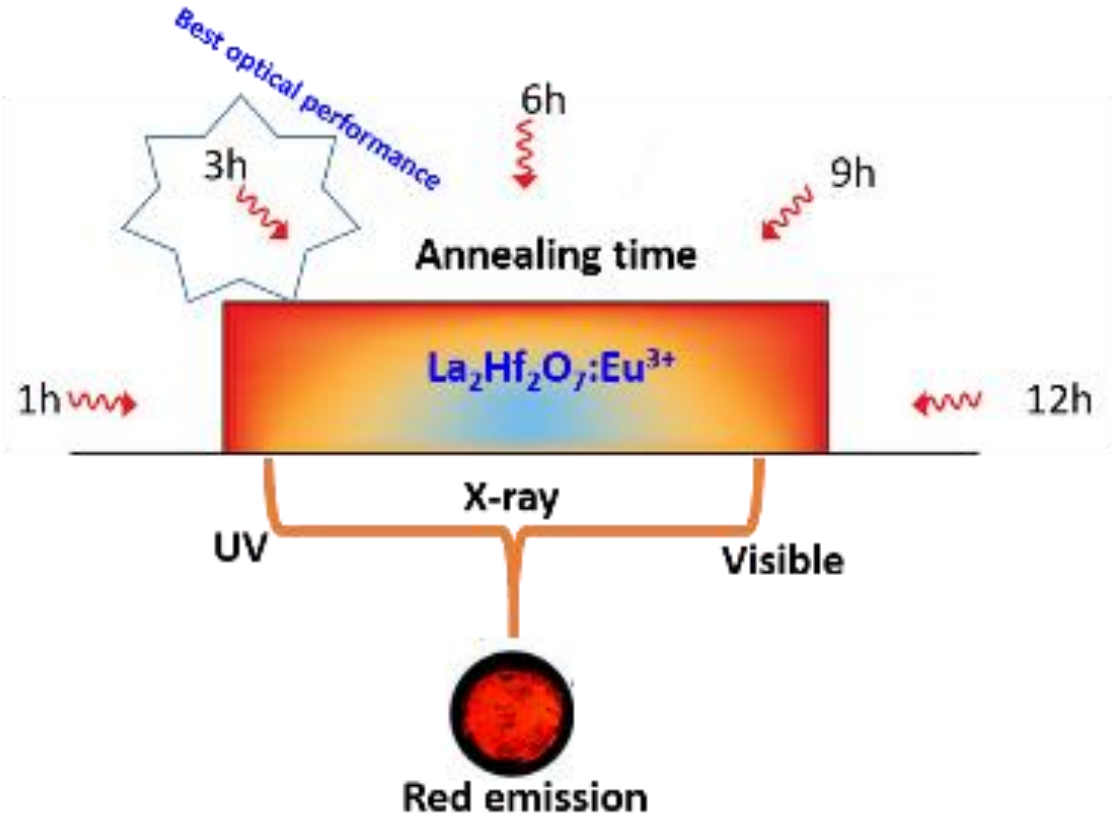

Figure 5.6: Exploration of processing time in molten-salt using $La_2Hf_2O_7$ doped Eu^{3+} NPs

5.1.3 Adjusting the Annealing Temperature in the Molten-Salt Synthesis

In this study, we have taken Eu^{3+} as luminescence structural probe to study the effects of thermal annealing on PL and RL of $La_2Hf_2O_7$:5%Eu^{3+} NPs. The effort was taken to investigate the effect of annealing temperature on radiative transition rate, Judd-Ofelt parameters, branching ratio, asymmetry ratio, and quantum yield of $La_2Hf_2O_7$:Eu^{3+} NPs. Structural changes induced by annealing temperature was also studied using X-ray diffraction (XRD), Raman spectroscopy, Fourier transformed infrared spectroscopy (FTIR) and BET surface area.

Figure 5.7 depicts the emission spectra of $La_2Hf_2O_7$:Eu^{3+} NPs at various annealing temperature under excitation of charge transfer band (CTB). The spectra consisted of typical

europium emission at 578, 586, 612, 654 and 708 nm corresponding to $^5D_0 \rightarrow {}^7F_0$, $^5D_0 \rightarrow {}^7F_1$, $^5D_0 \rightarrow {}^7F_2$, $^5D_0 \rightarrow {}^7F_3$ and $^5D_0 \rightarrow {}^7F_4$ transitions, respectively. Among these transitions, $^5D_0 \rightarrow {}^7F_1$ is called magnetic dipole transition (MDT), which is not affected by the crystal/ligand field or any kind of perturbation around europium ion. On the other hand, $^5D_0 \rightarrow {}^7F_2$ is called as hypersensitive electric dipole moment transition (EDT) is strongly influenced by the crystal or ligand field. $^5D_0 \rightarrow {}^7F_0$ transition is allowed neither by MDT nor by EDT and is normally seen when the site symmetry around europium ion is very low; normally C_s, C_n or C_{nv}. The presence of this transition in $La_2Hf_2O_7:Eu^{3+}$ NPs indicated that europium ion is not localized in symmetric environment. This is further supported by high intensity of EDT compare to magnetic dipole one.

There are two types of polyhedra that exist within the ideal pyrochlore lattice, 8-fold A site and 6-fold B site. The exact type of polyhedron formed is determined by the x coordinate of the 48f oxygen anion.(Richardson 2016) At x = 0.375, the six-fold polyhedron is at its most distorted, whilst the 8-fold polyhedron is a cube, which forms the defect-fluorite structure. At x = 0.3125, the 6-fold polyhedron forms a perfect octahedron, whilst the 8-fold polyhedron forms a distorted scalenohedra, a polyhedron where each face forms a scalene triangle, and can be viewed as a distortion of a cube which forms the ideal pyrochlore structure.

In the emission spectra, the high intensity of EDT up to 950^{o}C and presence of $^5D_0 \rightarrow {}^7F_0$ is attributed to majority of europium ion localized at distorted LaO_8 scalenohedra. Beyond 950^{o}C, the NPs tend to agglomerate to such an extent that it overpowers the effect of surface area and causes scattering of the emitted light and thereby decreasing the observed emission intensity. Therefore, the slight reduction in PL intensity beyond certain crystallite size is attributed to larger crystallite size, which tends to scatter light in particle excitation, leading to decrease in emission intensity.(Wang et al. 2007b) Table 5.1 lists the quantum yield value of our

$La_2Hf_2O_7:Eu^{3+}$ NPs annealed at various temperatures. Similar correlation can be found in the quantum yield measurement, wherein the 950°C annealed sample was found to have the maximum QY of 20.82%.

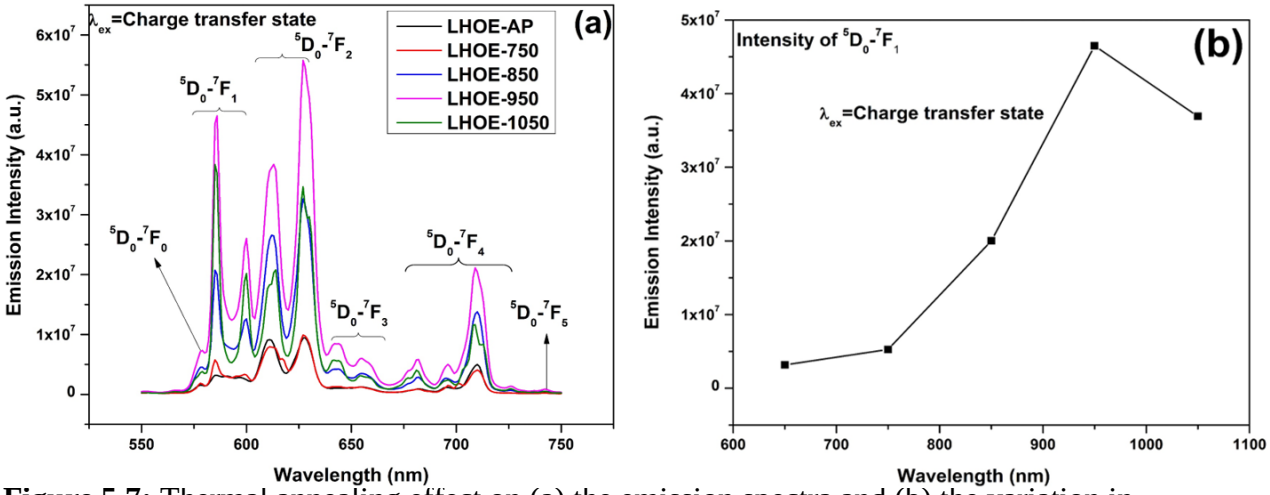

Figure 5.7: Thermal annealing effect on (a) the emission spectra and (b) the variation in emission intensity.

Table 5.1: BET surface area and asymmetry ratio of the $La_2Hf_2O_7:Eu^{3+}$ NPs as a function of annealing temperature

Samples	**BET surface area (m^2/g)**	**PL asymmetry ratio**	**Quantum yield (QY)**
LHOE-AP	25.007±0.1802	2.96	16.52
LHOE-750	18.982±0.0838	1.72	18.27
LHOE-850	15.293±0.0570	1.58	19.73
LHOE-950	9.6559±0.0365	1.23	20.82
LHOE-1050	6.8072±0.0296	0.90	18.13

In most of the phosphor materials, Eu^{3+} ion cannot be efficiently excited by near UV light (395 nm) due to its poor molar absorption coefficient (< 5 M^{-1} cm^{-1})(Binnemans 2015) owing to its forbidden f-f nature of $^7F_0 \rightarrow {}^5L_6$. To overcome these problems, proper sensitizer ions or host materials must be selected to sensitize Eu^{3+} to obtain ideal and tunable phosphor materials. This phosphor material, because it has very intense peaks at 395, 465 and 534 nm, ultra-violet (UV),

near-UV, UV-blue (UVB), and blue or green laser diodes/ LEDs can act as efficient pumping sources for the red emission from Eu^{3+} ions. Figure 5.8a shows the excitation spectra of the $La_2Hf_2O_7:Eu^{3+}$ NPs at various annealing temperatures, and by monitoring the red emission band at 612 nm, corresponding to $^5D_0 \rightarrow {}^7F_2$ transition of europium ion. The excitation intensity increases monotonously with annealing temperature. There are two main features: (i) broad band in the region of 265-330 nm attributed to oxygen to europium charge transfer band (CTB) and (ii) the fine spectral features from 350 -550 nm of the f-f transitions of europium ion. The study of the change in spectral position of CTB in the $La_2Hf_2O_7:Eu^{3+}$ NPs as a function of annealing temperature (grain size) is very important for proper understanding on the interaction between host and lanthanide ion in nanophosphor. We could also find some variation in broadness as well as position of this band in our nanoparticles. Although there is not perfect correlation in spectral band shift but higher temperature annealed samples (850, 950 and 1050) are blue shifted w.r.t to lower annealed one (650 and 750^oC). The lack of perfect correlation can be due to contribution of other transitions in CTB such as $O^{2-} \rightarrow La^{3+}$, $O^{2-} \rightarrow Hf^{4+}$ and $Hf^{4+} \rightarrow Eu^{3+}$. The charge transfer energy for large sized nanophosphor is more than that for smaller one. Charge transfer process is strongly influenced by Eu-O bond energy. In smaller sized NPs higher surface to volume ratio destabilizes Oxygen ion and therefore Eu-O has less bond energy.(Boukerika and Guerbous 2014) If Eu-O bond energy decreases, the bond weakens and it became easier for oxygen to transfer electron to europium ion and therefore charge transfer energy decreases and there is red shift in smaller size grains.(Fu et al. 2007) Another interesting thing is the narrowing of CTB as the annealing temperature increases. This may be because of predominating contribution of only one kind of charge transfer at higher temperature i.e. $O^{2-} \rightarrow Eu^{3+}$ and the other transitions mentioned above has minimal contribution. Emission characteristics of $La_2Hf_2O_7:Eu^{3+}$ NPs

under various excitation wavelength is shown in Figure 5.8b. All spectra display characteristic peak of europium ion. Red emission output under excitation with near UV or Blue LEDs are very poor relative to excitation with La Porte allowed charge transfer band (CTB). However, all commercial application of phosphor materials needs it to be excited under near UV (~395 nm) or blue light (~464 nm). The $La_2Hf_2O_7:Eu^{3+}$ NPs can be easily excited using UV, Violet, Blue and green LEDs and are highly successful in giving an intense red $^5D_0 \rightarrow {}^7F_2$ emission at 616 nm. Such materials can be used for phosphor converted white LEDs and can be explored for other application such as bioimaging and water disinfection.

The colorimetric performance of synthesized nanoparticles at various excitation wavelength were analyzed based on CIE index diagram shown in Figure 5.9. The emission results obtained after corrections for the $La_2Hf_2O_7:Eu^{3+}$ NPs at room temperature is shown in the CIE diagram, and it is seen that our samples give red-orange emission at all the excitation wavelength ranging from mid UV, near UV, blue and green light.

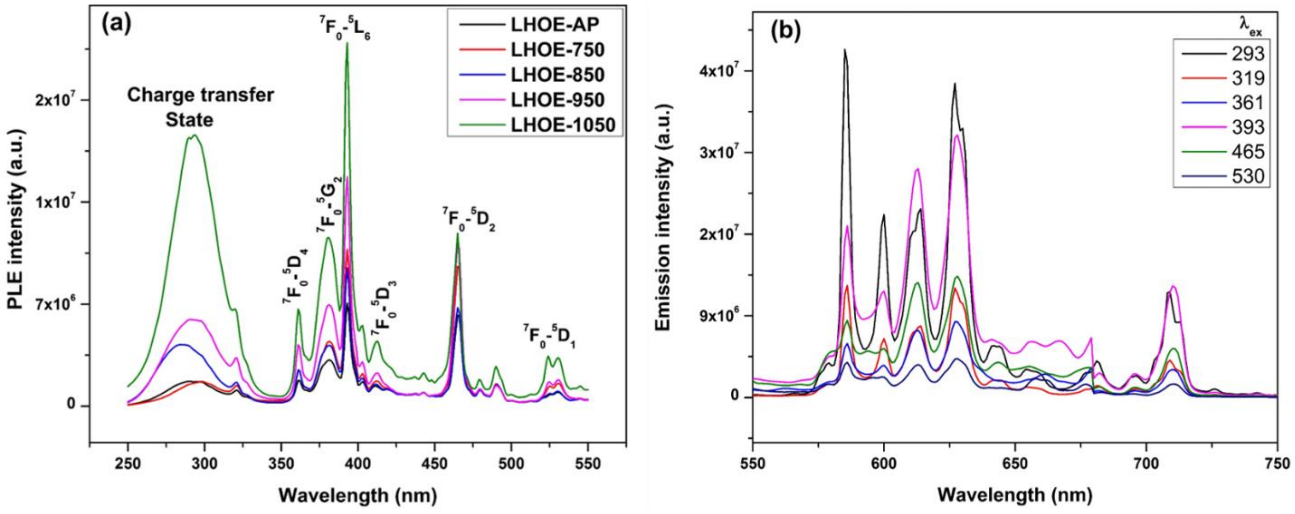

Figure 5.8: (a) Thermal annealing effect on excitation spectra of the $La_2Hf_2O_7:Eu^{3+}$ NPs. (b) Emission spectra of the LHOE-1050 NPs excited by various wavelengths.

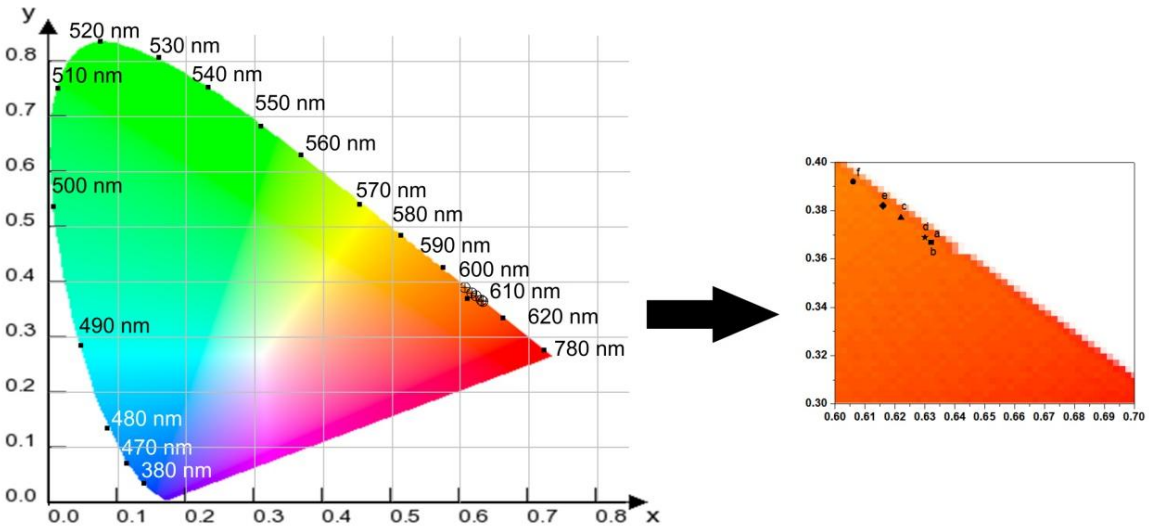

Figure 5.9. CIE chromaticity diagram coordinates of the $La_2Hf_2O_7:Eu^{3+}$ NPs (950^oC annealed) at various excitation wavelength. Right panel presents a detailed view of these coordinates in the red-end wavelengths.

The CIE coordinates of the samples does not change much with excitation wavelength, so the exact coordinates (x, y) are given in Table 5.2. We can see from the CIE index diagram that the doped pyrochlore NPs give stable red color emission with high color purity, which are highly favorable for light emitting diodes applications.(Siqueira et al. 2015) Table 5.2 also presents the correlated color temperature (CCT) of the $La_2Hf_2O_7:Eu^{3+}$ NPs under various excitation wavelength that was calculated based on equation (1) reported by McCamy.(McCamy 1992)

$$T = -437n^3 + 3601n^2 - 6861n + 5514.31 \quad (5.1)$$

where $n = \frac{x - 0.332}{y - 0.186}$

In practice, more is the CCT, emitted light color will be lighter in nature. We can observe that although some coordinates are overlapped the color temperatures are distinct. It is believed

that the CIE coordinate and CCT rare very important photophysical parameter which could be highly useful in designing materials for optical emitters or other luminescent devices.**(Siqueira et al. 2015)**

Table 5.2. CIE chromaticity coordinates and the CCT of the LHOE-1050 NPs excited at various wavelengths

Excitation wavelength (nm)	**CIE chromaticity coordinates (x, y)**	**Color temperature (K)**
293	(0.632, 0.367)	2045
319	(0.632, 0.367)	2045
361	(0.622, 0.377)	1869
393	(0.630, 0.389)	2005
465	(0.616, 0.382)	1804
530	(0.606, 0.392)	1731

In this work, we could successfully synthesize $La_2Hf_2O_7:Eu^{3+}$ NPs using a molten salt synthesis (MSS) method. The synthesized NPs were subjected to annealing at higher temperature up to 1050^{o}C. There was a progressive increase in size and decrease in surface area as the annealing temperature is raised. As a function of annealing temperature (650→1050^{o}C) quantum yield and emission intensity increases progressively up to 950^{o}C and then a slight reduction at 1050^{o}C. The phenomenon has been attributed to decrease in surface defects and -OH and -NH vibration as function of annealing temperature which was corroborated using surface area analysis and FTIR. Additionally, local symmetry around europium ion was found to increase monotonically as a function of annealing temperature and complete symmetric environment around europium ions was observed at highest annealing temperature 1050^{o}C. This was correlated using Raman spectroscopy that suggested that $La_2Hf_2O_7$ structure becomes more and

more ordered (ideal pyrochlore) as the annealing temperature is increased with highest degree of cation and anion ordering in the $La_2Hf_2O_7:Eu^{3+}$ NPs annealed at 1050^oC. The sample annealed at 1050^oC displayed site-specific luminescence wherein mid UV excitation leads to excitation of europium sitting at Hf^{4+} site and displayed intense orange emission compare to red one. On the other hand, excitation with near UV 393 nm excite both Eu^{3+} at La^{3+} site and Hf^{4+} site and displayed intense red emission compare to orange one. Such studies can be useful in designing need based orange or red phosphor. XEL output was found to be best for the 1050^oC annealed sample and in all sample's europium ions were in very low symmetry environment. The synthesized materials show difference emission characteristics in terms of asymmetry and emission output under excitation with highly energetic X-ray beam, which was attributed to different mechanism of NPs excitation under UV and X-ray.

Figure 5.10 shows a mechanism of what was found. At high temperature annealing of $La_2Hf_2O_7:Eu^{3+}$ NPs favors tunneling of dopant ion to highly symmetric site showing orange emission whereas low temperature annealing favors red emission. Distinct effect of annealing temperature on UV and X-ray excited luminescence was found to related to different excitation mechanism. The present highlighted the importance of thermal annealing on designing novel pyrochlore based material for optoelectronic and scintillator material.

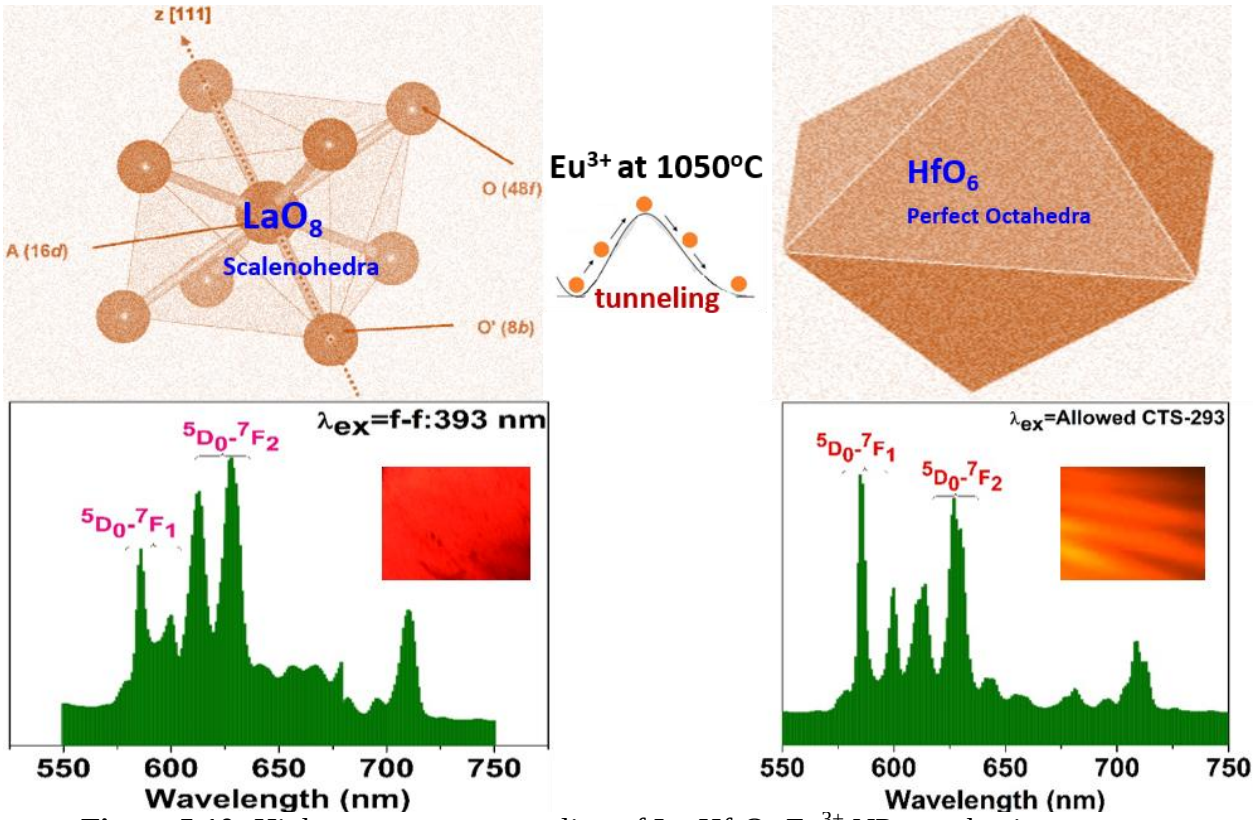

Figure 5.10: High temperature annealing of $La_2Hf_2O_7:Eu^{3+}$ NPs mechanism.

CHAPTER VI

ENGINEERING A WHITE LIGHT NANOPHOSPHOR

6.1.1. Crystal Purity and Phase Determination via X-ray Diffraction:

Figure 6.1 shows the different phase that $A_2B_2O_7$ structures can possibly accommodate. The powder X-ray powder diffraction (XPD) patterns of the LHOE, LHOT and LHOD powder are shown in Figure 6.2a-c respectively. The diffraction Peaks appearing in the pattern can be well indexed to Lanthanum Hafnium Oxide $La_2Hf_2O_7$ (01-073-0445). Typical super-lattice peaks corresponding to ideal pyrochlore structure approximately at 14° (111), 28° (311), 45° (511) and 51° (531) could not be seen in this case which normally requires synchrotron based XRD. So exact structure elucidation requires additional technique such as Raman or Fourier transformed infrared spectroscopy for confirmation. There are no additional diffraction peaks arising from any kind of impurity, even at higher doping concentrations, which confirms the formation of single-phase compounds for the entire samples. The XPD data also indicated the efficient doping of lanthanide into the $La_2Hf_2O_7$ matrix which is attributed to closeness in ionic radii of the Eu^{3+}, Tb^{3+}, Dy^{3+} and La^{3+} metal ions. It is noteworthy to mention that the incorporation of trivalent lanthanide ions into a $La_2Hf_2O_7$ host lattice substitute mostly trivalent La^{3+} ion, so charge balancing is also need required. The crystallite sizes of the LHOE, LHOT and LHOD at different doping level along with the lattice parameter was mentioned in Table 6.1. The average crystallite sizes were estimated from the X-ray diffraction data using well-known Debye-Scherrer equation. From this Table it is clearly seen that all the samples have particle size in range of 17-25 nm confirming the ability of molten salt synthesis to produce nanoparticles at low temperature.

In this work, the [222] reflection was used for crystallite size calculations. There is systematic decrease in the crystallite size from 0.5 to 10.0 mol% for all three (Fig. 6.2d). This is mainly attributed due to the distortion lanthanum hafnate host induced by incorporation of dopant ions which can retard the growth rate of $La_2Hf_2O_7$ nanocrystal(Gao et al. 2016).

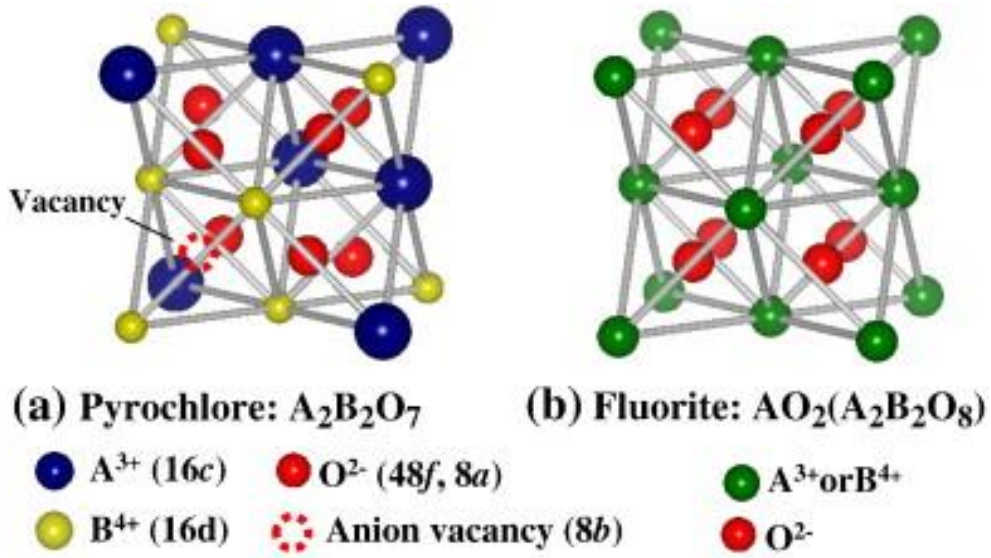

Figure 6.1: Crystal phase for $A_2B_2O_7$ structures.(Arachi and Nabeshima 2014)

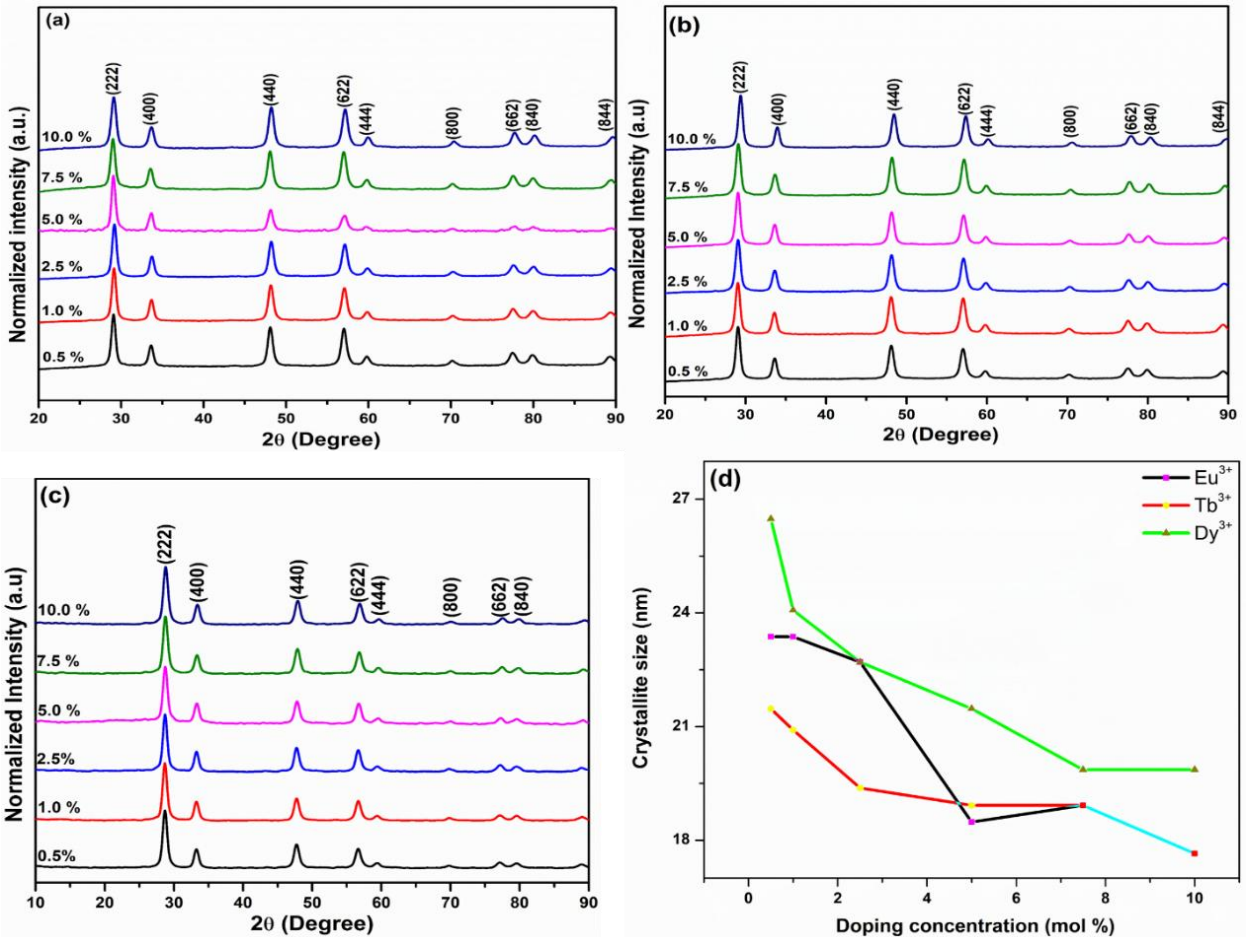

Figure 6.2: XRD pattern of (a) LHOE (b) LHOT, (c) LHOD (d) Variation in crystallite size as a function of dopant concentration. The percentage of dopant ion is varied from 0.5 to 10 %.

Table 6.1. Full Width Half Max (FWHM), Lattice parameter and particle size of LHOE, LHOT and LHOD under various doping levels

Europium ions				
Concentration (mol %)	**2θ(◦)**	**FWHM(β)**	**Lattice parameters(A°)**	**Particle size (nm)**
0.5 %	29.08	0.34	10.63	23.37
1 %	29.14	0.34	10.61	23.37
2.5%	29.19	0.35	10.59	22.70
5%	28.66	0.43	10.78	18.48
7.5%	29.01	0.42	10.65	18.92
10%	29.12	0.45	10.61	17.65
Terbium ions				
0.5 %	29.07	0.37	10.63	21.47
1 %	29.03	0.38	10.65	20.91
2.5%	29.06	0.41	10.64	19.38
5%	29.06	0.42	10.64	18.92
7.5%	29.10	0.42	10.62	18.92
10%	29.38	0.45	10.52	17.65
Dysprosium ions				
0.5 %	28.70	0.30	10.77	26.48
1 %	28.69	0.33	10.77	24.07
2.5%	28.71	0.35	10.76	22.70
5%	28.74	0.37	10.75	21.47
7.5%	28.77	0.40	10.74	19.86
10%	28.81	0.40	10.73	19.86

6.1.2. Raman Spectroscopy of the Activated $A_2B_2O_7$ Showing Pyrochlore Phase:

In order to confirm the structure of MSS synthesize $La_2Hf_2O_7$:Ln^{3+} (Ln=Eu, Tb and Dy) nanoparticles at various doping concentration, Raman spectroscopy was carried out and the obtained spectra is shown in Figure 6.3 a-c. The two variants of $A_2B_2O_7$ type pyrochlores are; ideal pyrochlore (S.G. Fd-3m) and disordered fluorite (S.G. Fm-3m). Based on group theory; disordered fluorite has only one vibrational mode which is Raman active F_{2g} and it involves vibration of O^{2-} ion an AO_4 tetrahedra environment(Gu et al. 2018). On the other hand, ideal pyrochlore phase with Fd-3m space group have six Raman active modes in the range of 200-1000 cm^{-1}. Among them, five Raman modes involve M-O vibration whereas the one at highest wavenumber is related only to the oxygen sublattice (Paul et al. 2016). The Raman peak positions for the other lanthanide ion doped $La_2Hf_2O_7$ NPs are located approximately around 305, 320, 402, 507, 522, and 609 cm^{-1} (see inset of Figure 1-c), which correspond respectively to F_{2g}, E_g, F_{2g}, A_{1g}, F_{2g}, and F_{2g} modes(Zuniga et al. 2018a). The one in wavelength region of 300–400 cm^{-1} originate from vibrations of the metal –oxygen bond (La–O and Hf–O bonds in this case), whereas the one at high wavenumbers (522 and 641 cm^{-1}) arises due to stretching of the Hf–O bonds. There small around 750 cm^{-1} is ascribed to the distortion of HfO_6 octahedra(Garg et al. 2008b). The extent of broadening in Raman peak indicates the level of disordering in the system. The FWHM of 320 cm^{-1} peak follows the trend Dy>Tb>Eu. This may be because of large difference in ionic radii (Δr) between La^{3+} and Dy^{3+} followed by La^{3+}-Tb^{3+} and europium have the closest proximity to La^{3+} ion.

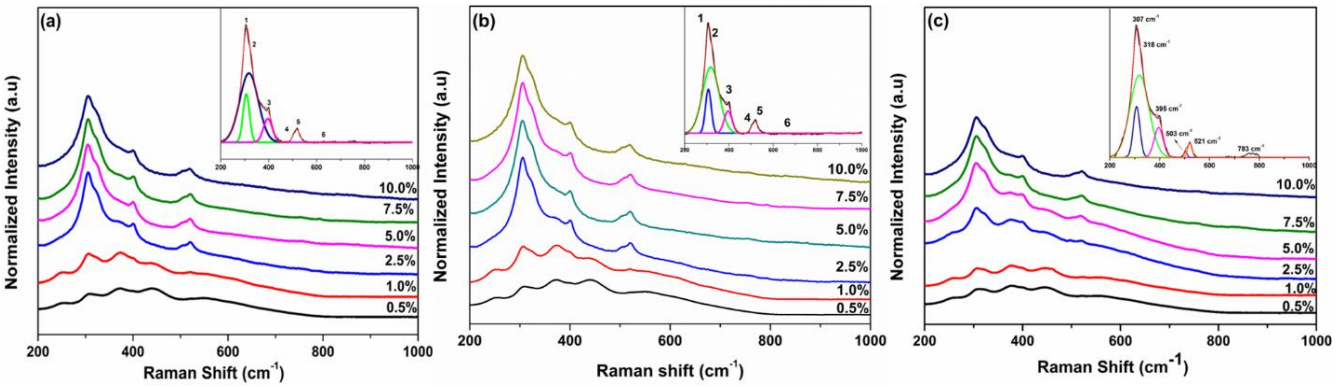

Figure 6.3: Raman spectra of (a) LHOE (b) LHOT and (c) LHOD. The percentage of dopant ion is varied from 0.5 to 10 %.

6.1.3. Scanning Electron Microscopy of the Synthesized NPs for Morphology Determination and Size:

Representative SEM micrographs of the LHOE, LHOT and LHOD NPs (0.5 % doping) are shown in Figure 6.4. The nanoparticles is looks spherical in morphology with the average sizes falling in the range (36-43 nm), with some of them forming agglomerations. The particle morphology and the average particle size of the doped lanthanum hafnate NPs are hardly affected by change in dopant ion. By measuring the diameter of 100 clearly identifiable particles from the SEM images, the average particle diameter was estimated using imageJ software and included in the inset of Figure 6.4a-c, which is in good agreement with XRD data. The powders synthesized by molten salt method were observed to be highly homogeneous, monodisperse and small size. This kind of morphology of particles with narrow size distribution is highly desirable for nanophosphors having good luminescent performances. The spherical nanoparticles are preferable for high brightness because they possess high packing densities and low light scattering(Kumar and Senthilselvan 2017).

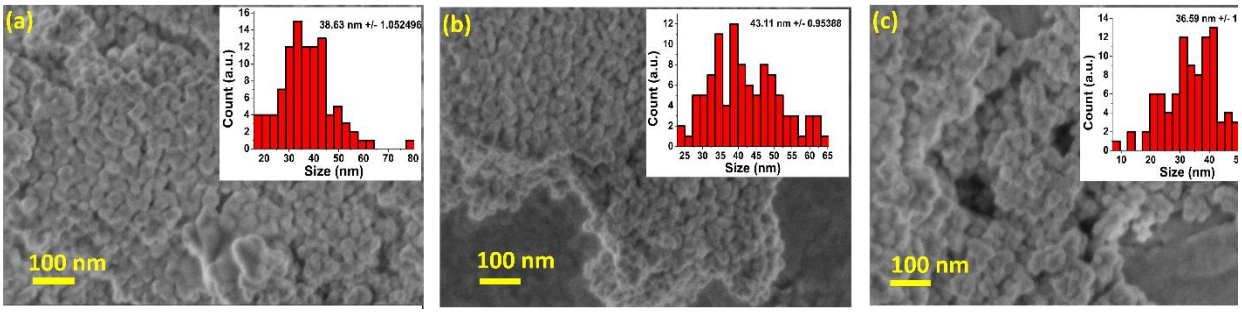

Figure 6.4: SEM images of (a) LHOE (b) LHOT and (c) LHOD NPs.

6.1.4. Photoluminescence Spectroscopy

6.1.4.1 Excitation Spectra of the LHOE, LHOD, LHOT NPs under UV:

Figure 6.5a shows the excitation spectra of LHOE under the excitation wavelength of 612 nm corresponding to $^5D_0$-$^7F_2$ transition of europium ion. The spectra displayed a broad band in the range of 250-315 nm due to $O^{2-} \rightarrow Eu^{3+}$ charge transfer. Other fine features from 320-550 nm is intra f-f band. The interesting features is the very high intensity of 393 and 465 nm due to $^7F_0$-$^5L_6$ and $^7F_0$-$^5D_2$ transition respectively. This makes LHOE an important phosphor that can be efficiently pumped using near UV 393 nm and blue light. The excitation spectra of LHOT for different Tb^{3+} concentrations at Λ_{em} = 543 nm is shown in Figure 6.5b. The excitation spectrum consists of three peaks centered around 220, 285, and 310 nm which are ascribed to transition from $^7F_6$ to the split 5d energy levels of terbium ions. The 4d energy levels have both low spin and high spin states designated by ^7D_j and ^9D_j energy levels (J = 0–5), respectively(Ricci et al. 2011). The most intense peak at 285 nm is attributed to the low spin allowed f–d transition from the $^7F_6 \rightarrow ^7D_5$, while the one at 220 and 310 nm are respectively ascribed to the allowed $^7F_6 \rightarrow ^7D_5$ and f–d forbidden high spin transition $^7F_6 \rightarrow ^7D_4$(Potdevin et al. 2010). The excitation spectra of LHOD for various Dy^{3+} concentration (Figure 6.5c) are recorded by fixing the emission maxima at 577 nm. Very similar to LHOE and LHOT; excitation spectra in this case too consists of a broad band centered at 258 nm which may be ascribed to the charge

transfer transition from $O^{2-} \rightarrow Dy^{3+}$. The excitation spectra of LHOD also has intense peaks located at 294, 323 and 351 nm attributed to $^6H_{15/2} \rightarrow {}^4H_{11/2} + {}^4G_{9/2}$, $^6H_{15/2} \rightarrow {}^4M_{17/2}$ (323 nm) and $^6H_{15/2} \rightarrow {}^6P_{7/2}$ (351 nm) respectively (Chemingui et al. 2015).

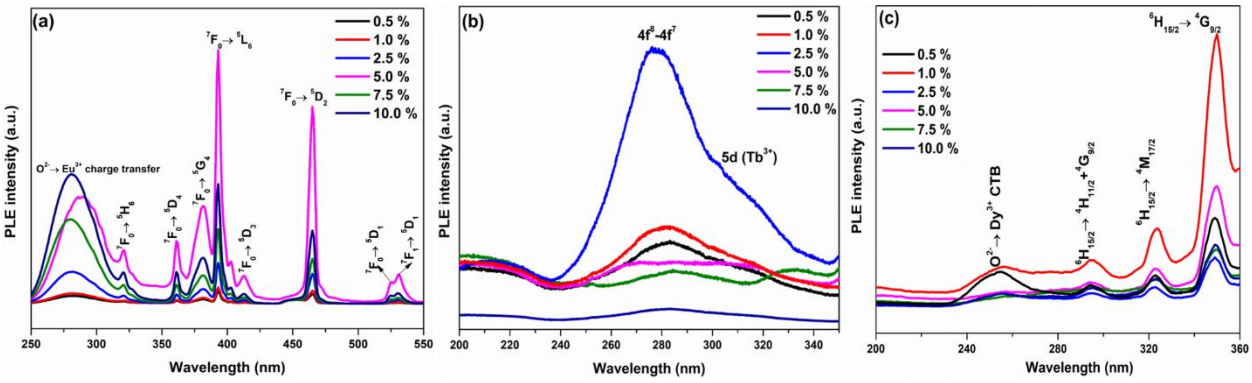

Figure 6.5: Photoluminescence Excitation spectra of (a) LHOE (λ_{em}=612 nm) (b) LHOT (λ_{em}=543 nm) and (c) LHOD (λ_{em}=577 nm). The percentage of dopant ion is varied from 0.5 to 10 %.

6.1.4.2 Emission Spectra in the Red, Blue, Green Region:

Upon excitation at $^7F_0$-$^5L_6$ (393 nm), the emission spectra of LHOE NPs for different europium ion concentration (Figure 6.6a) consists of strong emission bands typical of trivalent europium ion; $^5D_0 \rightarrow {}^7F_1$ (593 nm), $^5D_0 \rightarrow {}^7F_2$ (612 nm), $^5D_0 \rightarrow {}^7F_3$ (655 nm) and $^5D_0 \rightarrow {}^7F_4$ (710 nm). The orange emission band at 593 nm is characterized by magnetic dipole transitions (MDT) of Eu^{3+} and is not affected much by the crystal field strength. On the other hand, red emission peak located at 612 nm arises due to electric dipole transitions (EDT) of $Eu^{3+}$and is highly sensitive (hypersensitive, $\Delta J = \pm 1$) to its local surroundings around and its intensity and splitting strongly depends on the symmetry of the crystal field. The integral intensity ratio of EDT to MDT known as asymmetry ratio (A_{21}) gives information about local structure around the europium ion. For LHOE; the intensity of $^5D_0 \rightarrow {}^7F_2$ peak at 612 nm (EDT) is more intense compare to $^5D_0 \rightarrow {}^7F_1$ peak at 593 nm (MDT) which suggests low symmetry around Eu^{3+} in LHO NPs. Other structural

details about local site symmetry, stark splitting etc. based on emission spectra of LHOE NPs is already reported in our earlier work (Gupta et al. 2018c, Gupta et al. 2018d, Zuniga et al. 2018a). As a function of europium ion concentration there is not much change in the spectral features and peak position but relative intensity changes significantly.

When excited with 285 nm, the emission spectra of LHOT (Figure 6.6b) displayed various peaks at 487, 543, 584, 623, 648, 673 and 688 nm due to transitions of $^5D_4 \rightarrow {}^7F_{J=6, 5, 4, 3, 2, 1 \text{ and } 0}$ respectively of Tb^{3+} . The green emission band at 543 nm has magnetic dipole origin due to $^5D_4 \rightarrow {}^7F_5$ transitions of terbium ions, and it does not vary much with the crystal or ligand field. On the other hand, the blue emission band around 487 nm has electric dipole (ED) origin due to $^5D_4 \rightarrow {}^7F_6$ transitions of $Tb^{3+,}$ which is known to get affected by local structure and symmetry of Tb^{3+} (but is not hypersensitive like Eu^{3+})(Singh et al. 2015) . The $^5D_4 \rightarrow {}^7F_{0\text{-}1}$ emission peaks are in most of the cases are very weak in intensity and among the others the emission intensity mostly follow the pattern $^5D_4 \rightarrow {}^7F_6 > {}^7F_4 > {}^7F_3 > {}^7F_2$(Richardson 1982) which is what we are also observing in the case of LHOT. Although spectral splitting among the $^5D_4$-^7F_J transitions are sensitive to the nature and environment of ligand but elucidating structure related information based on spectral profile of terbium emission is not very straight forward or may not be as reliable as found using hypersensitive ions like Eu^{3+} or Sm^{3+}(Gupta et al. 2016e).

From Figure 6.6b it is clearly seen that the green emission band (I_G) at 543 nm (MD) due to $^5D_4 \rightarrow {}^7F_5$ transition is relatively strong compare to blue band (I_B) at 487 nm due to $^5D_4 \rightarrow {}^7F_6$ transition (ED); it can be postulated that large fraction of Tb^{3+} ions occupy relatively symmetric environment in $La_2Hf_2O_7$ pyrochlore NPs. The presence of both electric dipole and magnetic dipole transitions in the emission spectra of LHOT suggested that Tb^{3+} is distributed between

both La^{3+} and Hf^{4+} site though majority prefers to stabilize at symmetric HfO_6 octahedra in $La_2Hf_2O_7$ pyrochlore NPs.

Figure 6.6c show the emission spectra for LHOD for different Dy^{3+} concentration under 351 nm excitation. The emission spectrum consists of three main band at 481, 577 and 669 nm due to $^4F_{9/2} \rightarrow {}^6H_{15/2}$ (blue), $^4F_{9/2} \rightarrow {}^6H_{13/2}$ (yellow) and $^4F_{9/2} \rightarrow {}^6H_{9/2}$ (red) respectively. It is also known that the Dy^{3+} emission around 481 nm arises due to MDT and the one at 575 nm due to EDT. Generally, when Dy^{3+} is situated at site with relatively low symmetry (absence of centre of inversion), the yellow band is dominant, while the blue band is intense when Dy^{3+} ions occupies symmetric site. However, the fact that yellow emission at 577 nm is much more intense than blue emission at 482 nm suggesting that the local environment around dysprosium lacks inversion symmetry in LHOD. The Commission International del'Eclairage (CIE) chromaticity coordinate was calculated from the corrected emission spectrum and is shown in Figure 6.6d. From this figure red, green and bluish-green emission from LHOE, LHOT and LHOD is clearly seen. The actual image of the red and green luminescence from the LHOE and LHOT phosphor under near UV excitations is shown in the inset of Figure 5a and b.

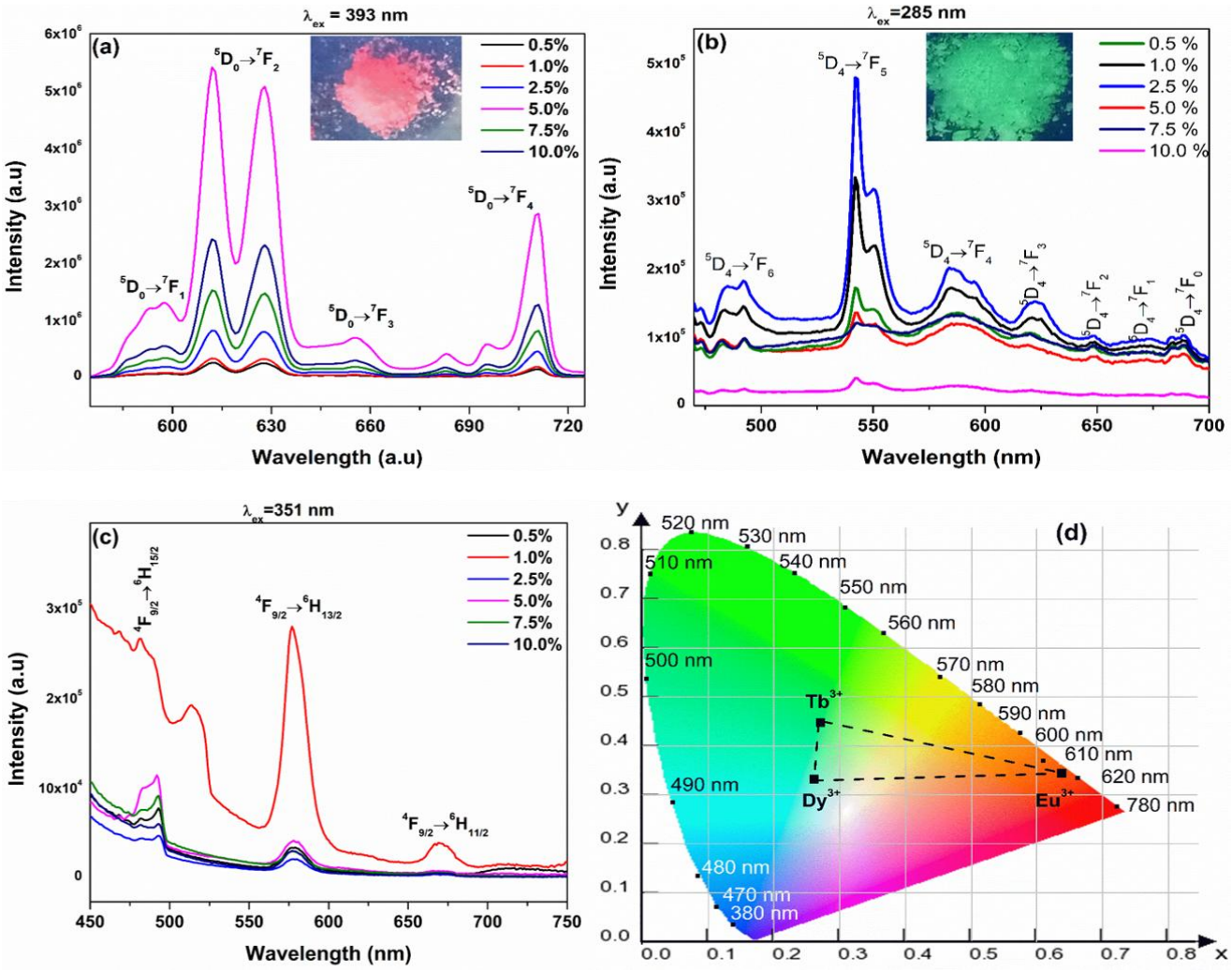

Figure 6.6: Photoluminescence Emission spectra of (a) LHOE (λ_{ex}=393 nm) (b) LHOT (λ_{ex}=285 nm) and (c) LHOD (λ_{ex}=351 nm). The percentage of dopant ion is varied from 0.5 to 10 %. (d) CIE color coordinate diagram depicting emitted color by Eu, Tb and Dy for 5.0. 2.5 and 1.0 % doping respectively. Inset of Figure 4a and 4b shows the digital image of the red and green emission from the powder sample of LHOE and LHOT NPs recorded under near UV lamp.

6.1.5. Concentration Quenching Studies:

The emission spectra of all samples (LHOE, LHOT and LHOD) have similar emission profile under various doping level but different relative emission intensities depending on the relative content of Eu^{3+}, Tb^{3+} and Dy^{3+} ions. Figure 6.7a shows the variation in emission

intensity as a function of dopant concentration. It can be clearly seen from this figure that that as the Eu^{3+}ion concentration increases initially from 0.1 to 5.0 mol %, the red emission at 612 nm ($^5D_0 \rightarrow {}^7F_2$) increased but beyond that the red emission intensity decreased due to the concentration quenching phenomena. It is believed that at the lower europium ion concentration, the distance between the neighboring europium (Eu^{3+} - Eu^{3+}) ions is far apart, whereas this distance decreases significantly at the higher europium concentration, leading to cross-relaxation process in between them. As a result, the concentration quenching phenomena occurred at concentration higher than 5.0 mol %. Thus, the optimum concentration of Eu^{3+} ions in the $La_2Hf_2O_7$ host lattice was evaluated as 0.05 mol. However, concentration quenching happens at relatively lower concentration in case of LHOT and LHOD as can be easily seen from Figure 6.7a. The critical concentration for LHOT and LHOD was respectively found to be 0.025 and 0.01. This can be related to different critical distance value exiting in these three NPs.
To have better insight into exact mechanism responsible for quenching mechanism critical distance (r_c) needs to be evaluated using the equation:

$$r_c = 2\left(\frac{3V}{4\pi X_c N}\right)^{\frac{1}{3}} \quad (6.1)$$

where r_c is the critical distance between the dopant ion and quenching site, V is unit cell volume, X_c is the critical concentration of Ln^{3+} ions, and N is the number of sites that the activator ion can occupy in the host. The critical distance calculated based on above formula for LHOE, LHOT and LHOD is 14.4 Å, 30.9 Å and 24.6 Å respectively. There are two main mechanisms for concentration quenching: exchange interaction (Rc < 5 Å) and multipolar interaction (Rc > 5 Å)(Guan et al. 2017). The critical distance for all three NPs is much larger than the typical critical distance of exchange interaction (5 Å). Thereby, it can be concluded that electric

multipolar interactions would be main mechanism responsible for the energy transfer from one rare earth ion to another. Figure 6.7b shows the value of critical concentration and critical distance for LHOE, LHOT and LHOD NPs. One can easily infer from this figure that there is inverse relation between two.

Now it becomes imperative to know the exact type of electric multipolar interaction responsible for non-radiative energy transfer between RE^{3+} ions. Van Uitert had formulated an equation based on which(Van Uitert 1967), if the energy transfer involved same acceptor and donor, the type of electric multipolar interaction can be deciphered from the variation in emission intensity per unit concentration using the relation (6.2):

$$I/x=K[1+\beta(x)\theta/3]^{-1} \quad (6.2)$$

In the equation, (x) is the concentration of RE^{3+} ion which is not less than the critical concentration. The (I/x) is the emission intensity *(I)* per phosphor *(x)*. The (K) and (β) are constants for the same excitation condition for a given phosphor nanoparticle. The (θ) value indicates the type of electric multipolar character responsible for concentration quenching. When the value of $\theta = 3$ non-radiative energy transfer proceed via exchange interaction, while $\theta = 6$ corresponds to dipole–dipole (d–d), $\theta = 8$ corresponds to dipole–quadrupole (d–p) and $\theta = 10$ corresponds to quadrupole– quadrupole (q–q) interactions(Ilhan et al. 2015). Applying the condition that $\beta(x)\theta/3 \gg 1$, equation (6.2) can be simplified as follows:

$$\log (I/x) = K' - \theta/3 \log x \ (K' = \log K - \log \beta) \quad (6.3)$$

The slope of this equation [plot of log (I/x) and log (x)] gives the value of electric multipolar character (θ). The plot of log (I/x) as a function of log (x) for LHOE, LHOT and

LHOD were shown in Figure 6c-e respectively. From this plot the value of slope (-θ/3*)* we got for LHOE, LHOT and LHOD NPs is -2.53504, -1.74559 and -1.73756 respectively. This gives the value of electric multipolar character (*θ*) on multiplication with 3.0 approximately as 8, 6 and 6 for LHOE, LHOT and LHOD. Therefore, it can be concluded that energy transfer mechanism in LHOE proceed via a dipole−quadrupole interaction whereas in LHOT and LHOD it proceeds via dipole-dipole interaction.

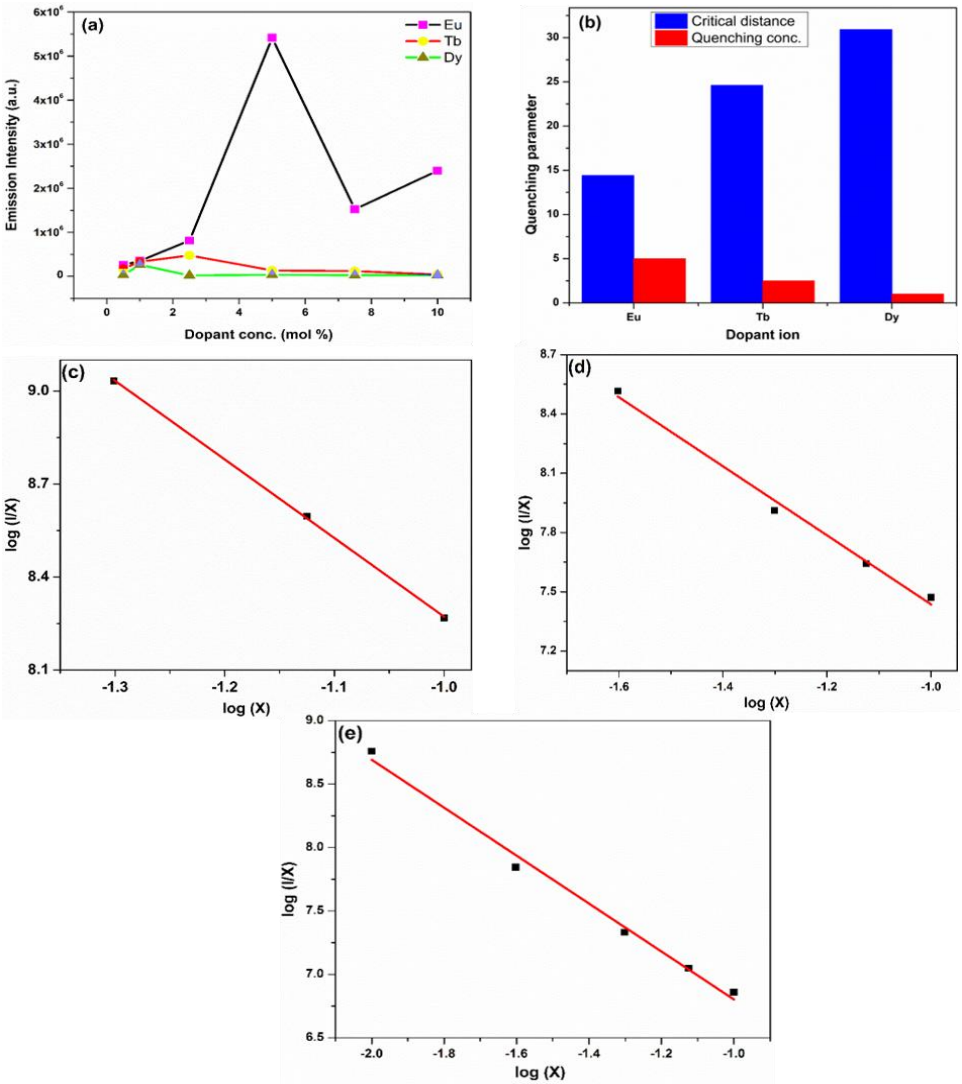

Figure 6.7: (a) Variation of emission intensity with concentration, (b) Comparison of critical concentration and critical distance for LHOE, LHOT and LHOD. Relation between the $\log_{10}(I/x)$ and $\log_{10}(x)$ for (c) Eu^{3+} (d) Tb^{3+} and (e) Dy^{3+} in doped $La_2Hf_2O_7$ NPs.

6.1.6. Determination of the Luminescence Lifetime:

Figure 6.8a displays the luminescence decay profile of LHOE NPs. The curve exhibits biexponential behavior (for concentration > 1.0 %), which can be fitted into an approximate function as

$$I = I_0 + B_1\exp(-t/\tau_1) + B_2\exp(-t/\tau_2) \quad (6.4)$$

where I_0 is the initial emission intensity at time t = 0, and τ_1 and $\tau_1$are the shorter and longer lifetime values. The lifetime values were mentioned in Table 6.2. It can be seen from this table that at lower concentration (0.5 and 1.0 %) decay curve displayed monoexponetial behavior with lifetime value of 2.63 and 3.01 ms. This indicated homogenous distribution of europium ion in LHO NPs at lower doping level. It is possible that at lower concertation europium ion is specifically localized only at asymmetric LaO_8 scalenohedra. At higher concentration more than 1.0 %; minor fraction (22-27 %) of europium ion tunnels to relatively symmetric HfO_6 octahedra of LHO pyrochlore NPs. The shorter lifetime component corresponds to the Eu^{3+} surroundings with more defect states and the longer lifetime component corresponds to the Eu^{3+} surroundings with less defect states(Dai et al. 2008). The stabilization of Eu^{3+} at La^{3+} does not invoke the need for charge compensating defects whereas the one at Hf^{4+} needs to be compensated by oxygen vacancies.

When trivalent lanthanide ion goes to tetravalent hafnium site, charge compensation takes place by formation of oxygen vacancies.

$$2Eu^{\dddot{}} + 3Hf_{Hf}^{\times} \leftrightarrow 2Eu_{Hf}^{'} + V_O^{\cdot\cdot} \quad (6.5)$$

Therefore, the shorter lifetime (0.94-1.19 ms) is attributed to Eu^{3+} sitting at Hf^{4+} site whereas the one at La^{3+} is having longer lifetime (3.26-3.79 ms). As a function of concentration, we could not see any regular trend in τ_1 and τ_1.

Interestingly the luminescence decay profile of LHOT (Figure 6.8b) yield only single lifetime in the range of 0.5 ms = 2.11 ms. As discussed in emission spectra of LHOT that Tb^{3+} stabilizes mostly at symmetric Hf^{4+} site in LHO NPs because of high intensity of MDT than EDT. Such low lifetime value is due to presence of oxygen vacancies as a charge compensating defects that provide non-radiative pathways. From Table 6.2, the lifetime value monotonically decreases with the increasing Tb3+ concentration, which was attributed to increased nonradiative relaxation rates due to cross relaxation processes among Tb^{3+} ions.

For LHOD also at 0.5 %; decay profile exhibits monoexponentially behavior but beyond that biexponential decay is observed. The fast component (0.019-0.34 ms) corresponds to the Dy occupying Hf^{4+} site and the slow component (0.32-1.34 ms) corresponds to the Dy^{3+} localized at La^{3+} site. The population of the shorter component gradually increased with the increasing Dy^{3+} concentration from 24 to 42 %, whereas that of the longer component decreased from 76 to 58 % in LHOD NPs. Like, LHOT and for the same reason; here also as a function of Dy^{3+} concentration both shorter and longer decay constant decreases.

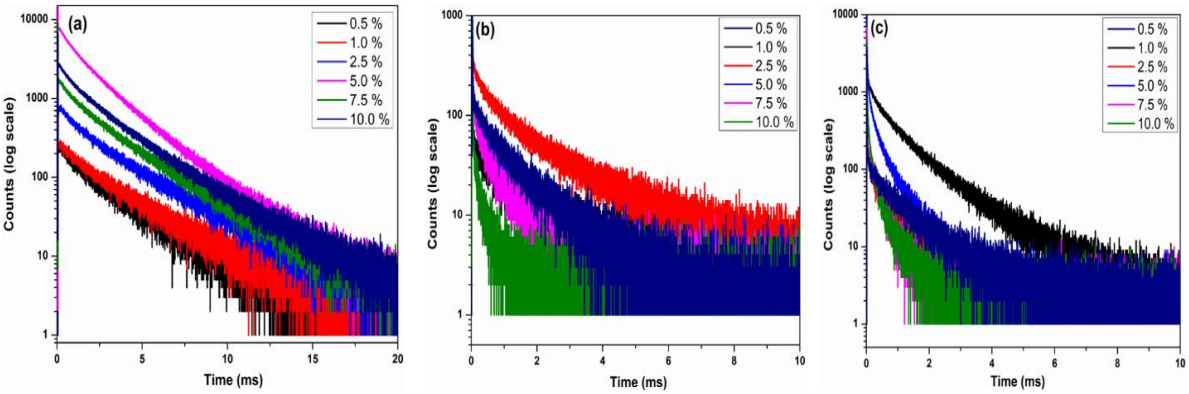

Figure 6.8: Photoluminescence decay profile of (a) $La_2Hf_2O_7:Eu^{3+}$ (λ_{ex}=393 nm/ λ_{em}=612 nm) (b) $La_2Hf_2O_7:Tb^{3+}$ (λ_{ex}=285 nm/ λ_{em}=543 nm) and (c) $La_2Hf_2O_7:Dy^{3+}$ (λ_{ex}=351 nm/ λ_{em}=577 nm).

Table 6.2: Luminescence lifetime for $La_2Hf_2O_7:Eu^{3+}$, $La_2Hf_2O_7:Tb^{3+}$ and $La_2Hf_2O_7:Dy^{3+}$ NPs.

$La_2Hf_2O_7:Eu^{3+}$		
	τ_1 (ms)	**τ_2(ms)**
0.5 %	2.63	-
1.0 %	3.01	-
2.5%	1.19 (23 %)	3.79 (77 %)
5.0 %	0.94 (27 %)	2.57 (73 %)
7.5%	1.03 (22 %)	3.26 (78 %)
10 %	0.97 (22 %)	3.10 (78 %)
$La_2Hf_2O_7:Tb^{3+}$		
0.5 %	2.11	-
1.0 %	1.49	-
2.5%	1.41	-
5.0 %	0.76	-
7.5%	0.67	-
10 %	0.15	-
$La_2Hf_2O_7:Dy^{3+}$		
0.5 %	1.042	-
1.0 %	0.34 (24 %)	1.34 (76 %)
2.5%	0.11 (34 %)	0.82 (66 %)
5.0 %	0.094 (37 %)	0.64 (63 %)
7.5%	0.019 (38 %)	0.345 (62 %)
10 %	0.024 (42%)	0.323 (58 %)

6.1.7. Light Yield under X-Ray Excitation (Scintillation):

The self-explanatory instrumental set up used for carrying out radioluminescence measurement on nanoparticles are depicted schematically in Figure 6.9.

X-ray luminescence optical imaging has been recognized as a powerful technique for medical diagnosis due to its deep penetration and low auto-fluorescence in tissues. With regards to potential application in bioimaging, the light output of the nanophosphors under X-ray irradiation is very important characteristics. Figure 6.10a-c illustrates the X-ray excited optical luminescence

(XEOL) spectra for the various scintillating nanoparticles synthesized in this work viz. LHOE, LHOT and LHOD. The XEOL spectra of LHOE (Figure 6.10a) displayed characteristics like photoluminescence with highest intensity of red band corresponding to $^5D_0$-$^7F_2$ transition. In terms of concentration dependence XEOL; 5.0 % doped sample like PL exhibits maximum intensity and beyond that there is reduction due to concentration quenching. Similarly, under X-ray irradiation LHOT (Figure 6.10b) and LHOD (Figure 6.10c) displayed intense green and yellow emission due to $^5D_4 \rightarrow {}^7F_5$ and $^4F_{9/2} \rightarrow {}^6H_{13/2}$ transition of Tb^{3+} and Dy^{3+} respectively. The concentration dependence XEOL is in complete agreement with photoluminescence results. The schematic showing red, green and yellow color emission by LHOE, LHOT and LHOD under X-ray excitation is shown pictorially in Figure 6.10d.

The radioluminescence emission on x-ray irradiation takes place after various processes that initiates; once large quantity of electron is created in conduction bands (CB) and holes in the valence bands (VB). Figure 6.11 presents a probable mechanism for the observed radioluminescence in the pyrochlore nanocrystals. Initially, when highly energetic X-ray beam falls on the LHO pyrochlore NPs it interacts with the hafnium atom (high Z and high density) of the pyrochlore lattice mainly via the photoelectric effect. This photoelectric interaction generates large quantity of electron and holes, and electronic transport occurs between the LHO pyrochlore nanocrystals. The hot electrons and holes are then thermalized quickly in the edges of CB and VB of pyrochlore. The electrons in the CB decay non-radiatively until the bottom of the CB and then recombine with holes created in the VB. This e^--h^+ recombination energy released can be used to excite Eu^{3+} ions leading to characteristics Eu^{3+} emissions.

The trapping and radiative recombination of e^--h^+ pairs can be precisely controlled which can be used to create tunable luminescence by altering the band gap of material. The mechanism

of intense X-ray scintillation could be attributed in part to the strong X-ray stopping power of LHO NPs due to heavier Hf atom.

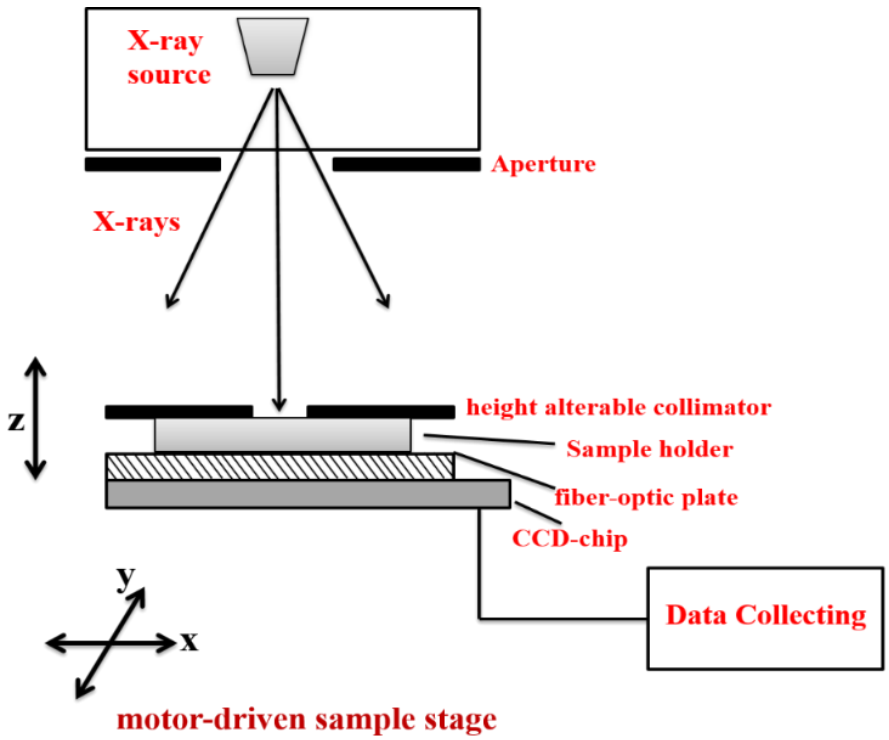

Figure 6.9: Experimental set up for radioluminescence measurement

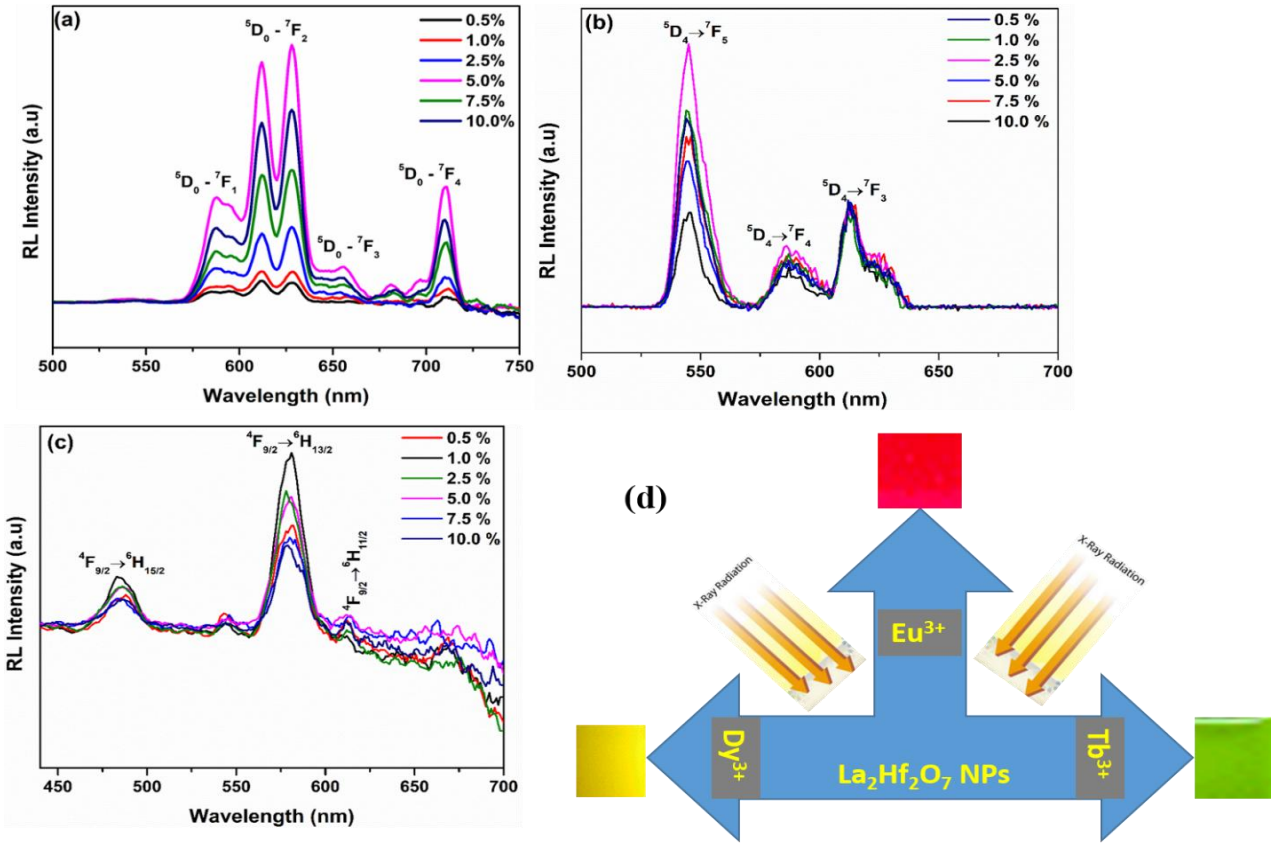

Figure 6.10: Radioluminescence Emission spectra of (a) LHOE (b) LHOT and (c) LHOD. The percentage of dopant ion is varied from 0.5 to 10 %. (d) Schematic diagram depicting emitted color by Eu, Tb and Dy for 5.0. 2.5 and 1.0 % doping respectively under X-ray irradiation.

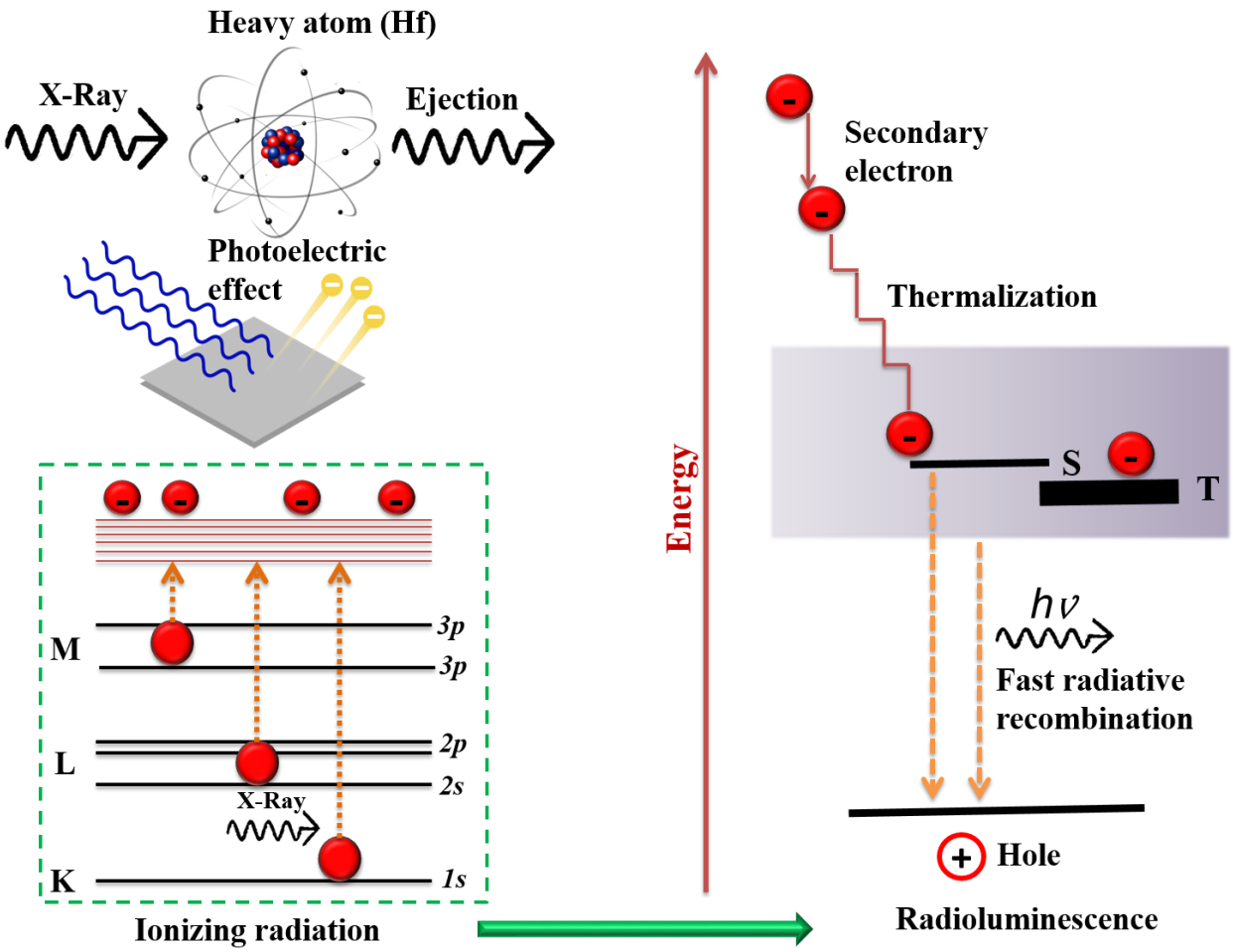

Figure 6.11: Proposed mechanism of X-ray scintillation in a pyrochlore nanocrystals.

6.1.8. Warm White Light Emission from Triply Co-Doped LHO NPs

Because of the fact that the warm white light is highly useful for indoor lighting in house and offices, and exhibits similar advantage as luminescence lamps, with low correlated color temperature (CCT) (CCT ≤ 3500 K), is highly recommended for human eyesight(Li et al. 2014, Gupta et al. 2017d). There is no report in literature exploiting pyrochlore host for warm white light with low CCT. In most of the report's authors have seldom get warm white light with lower CCT for indoor lighting (Li et al. 2014, Wang et al. 2014b, Guo et al. 2012). This cause the problem of glare in the eyes which is not good for retina. Therefore, it becomes imperative to develop a lower CCT single-phased warm white light emitting phosphor. With the aim of

synthesizing warm white light emitting doped LHO NPs, it was co-doped with all the three activators Tb^{3+} (green), Dy^{3+} (yellow/blue) and Eu^{3+} (red). With the aim of exploring lanthanum hafnate pyrochlore NPs for generating warm white, we have tried to optimize the doping concentration of various rare earth ions (Eu^{3+}, Tb^{3+}, Dy^{3+}). The resultant emission spectra and CIE index for tri-doped doped system is shown in Figure 6.12a and b respectively.

Color coordinates are extremely important parameters in deciding the efficient performance of synthesized nanophosphors. As shown in Figure 6.12b and Table 6.3, the CIE color coordinates and CCT of YHO:Eu, Tb, Dy phosphors were plotted and tabulated were measured. While the concentration of Tb^{3+} decreased from 1.5 % to 0.2 %, but that of Dy^{3+} and Eu^{3+} is raised respectively from 0.5 to 5.25 % and 0.05 to 0.35 % respectively. The corresponding color of the phosphor shifted from greenish white to warm white light (yellowish white). In particular, the CCT of white light can be tuned by changing the concentration of the dopant ion from 4930 to 2830 K. Table 6.3 represents chromaticity coordinates for doped LHO NPs for different concentrations of Eu, Tb and Dy. It can be seen from the Table 63 that 0.2 %Tb, 5.25 % Dy, 0.35% Eu doped LHO NPs displayed perfect warm white light with very low CCT value of 2830 K. Here role of red phosphor is very important in decreasing the CCT. In our future work, we will be tried to perform electroluminescence measurement and measure the efficiency of warm white light.

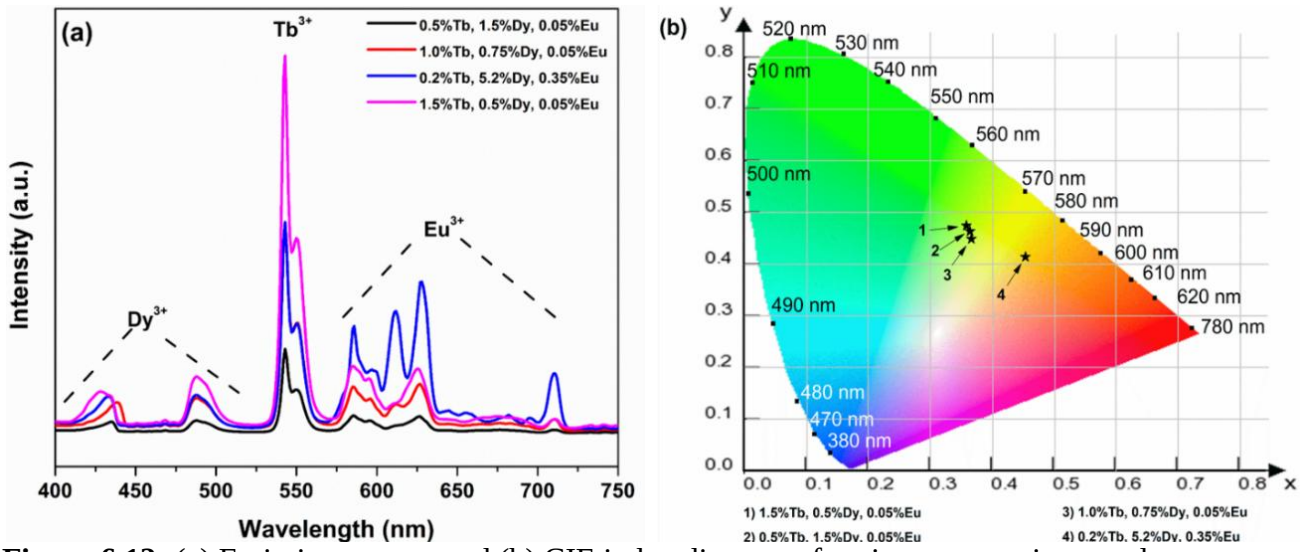

Figure 6.12: (a) Emission spectra and (b) CIE index diagram of various composite samples $La_2Hf_2O_7:Eu^{3+}$, Tb^{3+}, Dy^{3+} under 254 nm excitation.

Table 6.3: Color coordinate and color temperature various composite samples $La_2Hf_2O_7:Eu^{3+}$, Tb^{3+}, Dy^{3+} under 254 nm excitation

Composition	**CIE index**	**CCT**
1.5 %Tb, 0.5 % Dy, 0.05% Eu	(0.357, 0.475)	4930
0.5 %Tb, 1.5 % Dy, 0.05% Eu	(0.363, 0.465)	4780
1.0 %Tb, 0.75 % Dy, 0.05% Eu	(0.366, 0.450)	4690
0.2 %Tb, 5.25 % Dy, 0.35% Eu	(0.415, 0.526)	2830

6.1.9. Exploring White Light Emission from a Co-Doped LHO NPs

Here, we try to reach as close as possible to pure white light using a co-doped system rather than a tri-doped system in the previous section. It was noticed that a co-doped system was much easier to manipulate since it eliminates a variable in play. In this study, we used bismuth as the blue component and europium as the red component to produce an effective white light source. The molar concentration of bismuth was kept constant to a 0.5% in doping while the concentration of europium was changed stoichiometric to higher concentrations. Figure 6.13 (a)

shows the emission spectra excited at 285 nm. Here, it can be admired an effective energy transfer with the increase concentration europium, and it can be appreciated in the (b) CIE index showing a blue emission to red. One of the compositions show very promising results. LHO: Eu1%/ Bi0.5% shoe relatively closed color coordinates to white emission as shown in table 6.4. In Figure 6.14. a plot shows the efficient of transition being as highest as 95% higher than reported values for solid state lighting. The sample was excited at different excitation wavelength ad shoe a magnificent color shift from pink to white when excited with 365 nm wavelength. This is a very interesting feature as in because most of the material needs to be excited in this range for commercial purposes. Figure 6.15 show this investigation where the sample was taken and excited at different excitation and later characterized with it proper color coordinate and temperature. When the sample was excited with the 365 nm wavelength it shows a temperature of 6739 K relatively close to that light emitted by the sun.

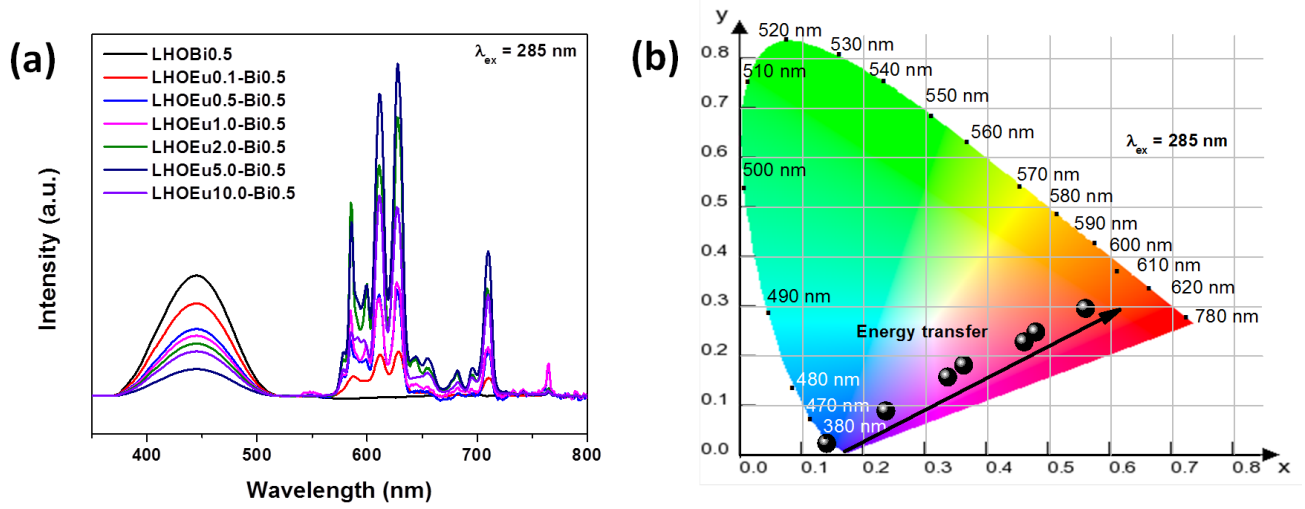

Figure 6.13: (a) Emission spectra (b) CIE index diagram for the LHO: Bi^{3+}/ Eu^{3+} compounds

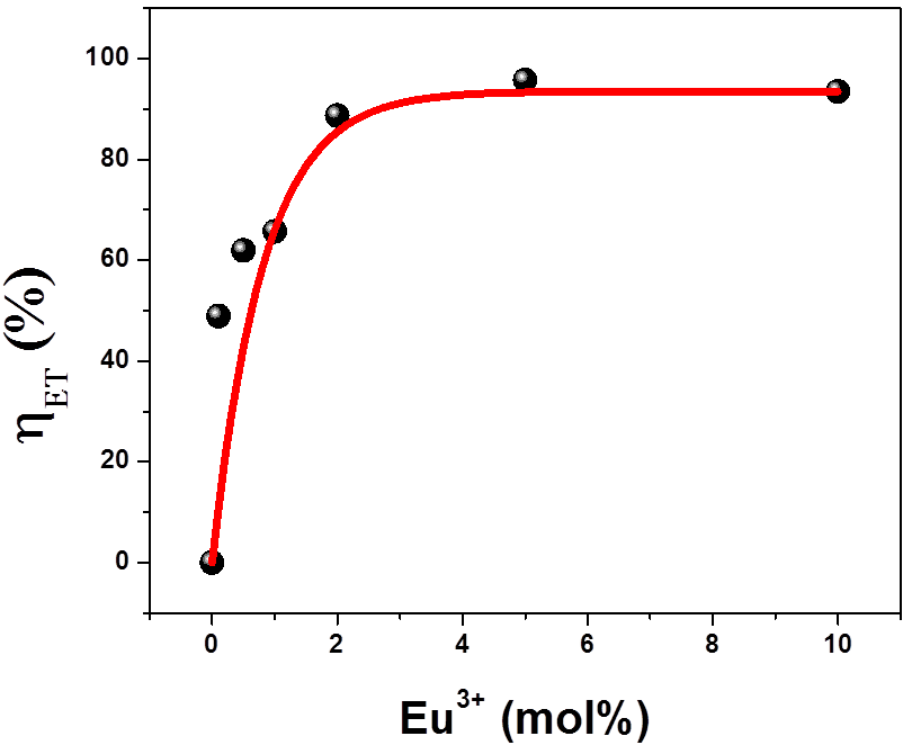

Figure 6.14: Plot of the percent efficient energy transfer as a function of increasing Eu^{3+} concentration.

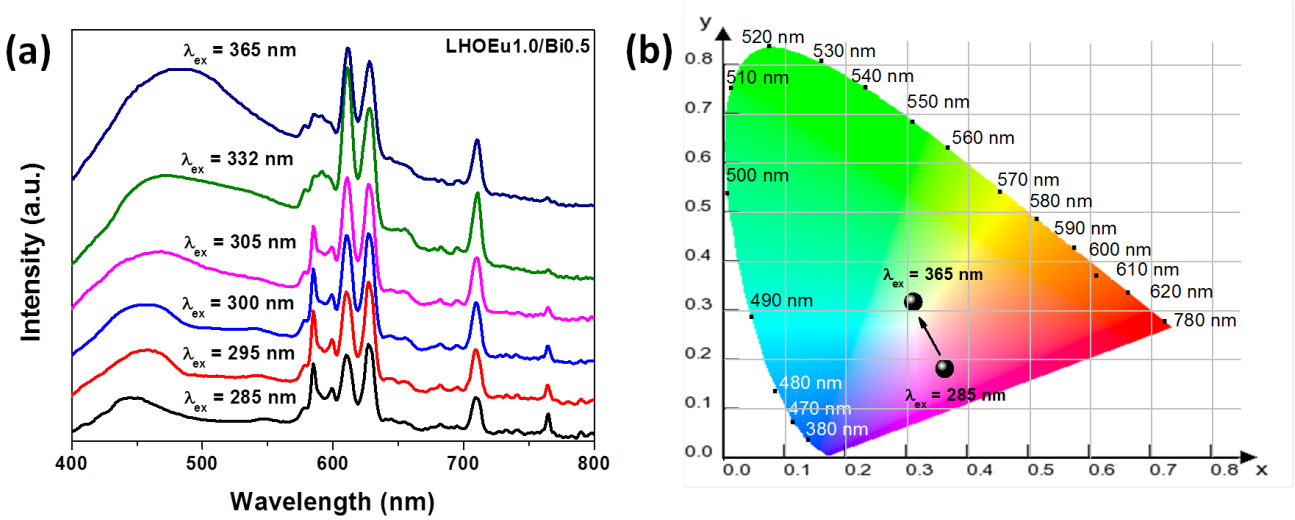

Figure 6.15: (a) Emission spectra (b) CIE index diagram for the LHO:0.5%Bi^{3+}/ 1.0%Eu^{3+} compound at different excitation wavelengths.

Table 6.4: Color coordinates and temperature for the LHO:0.5%Bi^{3+}/ 1.0%Eu^{3+} compound at different wavelengths.

Wavelength (nm)	Coordinate (x, y)	Temperature (K)
285 nm	(0.37, 0.30)	3611.2
295 nm	(0.37, 0.30)	3611.2
300 nm	(0.36, 0.31)	4143.6
305 nm	(0.35, 0.31)	4592.9
332 nm	(0.35, 0.34)	4760.9
365 nm	(0.31, 0.32)	6739.7

6.1.10. Exploring Thermal and Hydrostatic Pressure Effect on Luminescence of the LHOE NPs.

For application in high-power LEDs, the thermal stability of phosphors is one of the important issues to be considered. Therefore, we have explored the thermal stability of the LHOE-S1.5 sample using in situ PL measurements. At room temperature, the material experienced intense red luminescence. However, as the temperature increases systematically, the PL intensity output decreases continuously as seen in Figure 6.16(a). Such PL reduction is due to thermal quenching wherein emissive centers are thermally activated through the crossing point between the ground- and excited-state levels.(Gupta et al. 2016o) At 673 K, the red emission output of our NPs decreases to 53.74% to the original emission, and at 973 K, it is fully suppressed as seen in Figure 6.16(b). This behavior indicates that the LHOE NPs possess

extraordinary thermal stability, and it is suitable for usage as a phosphor in LEDs. In addition, the activation energy of the NPs was extrapolated from the slope of Figure 6.16(c) denoted from the following Arrhenius equation:

$$\ln(\frac{I_o}{I} - 1) = lnA - \frac{\Delta E}{kT} + C \quad (6.6)$$

where I_0 expresses the initial PL intensity, I is the PL emission intensity at a given temperature T and a given constant A, ΔE denotes the activation energy involved, and k is the Boltzmann constant. The relationship of $\ln\left(\frac{I_0}{I} - 1\right)$ and $\frac{1}{kT}$ holds a linear fit. The slope was computed through linear regression to be −0.41, which is proportional to the involved activation energy of the LHOE NPs. Therefore, the activation energy is equal to 0.41 eV for thermal quenching. In this unique case, the activation energy is superior to the usual value for europium-doped silicate-based red phosphors with $\Delta E \sim 0.23$ eV.(Zhang et al. 2017b) The reported activation energies of $La_2Zr_2O_7$:$Eu^{3+}$and Sr_2MgTeO_6:Eu^{3+} phosphors for thermal quenching are 0.16 and 0.27 eV, respectively.(Min et al. 2018, Liang et al. 2018) A very high activation energy value of 0.41 eV supports the fact that other than high QY, good emission and radioluminescent properties, and high lifetime, our LHOE NPs indeed also have excellent thermal stability.

The absolute temperature sensitivity (S_a) is a vital parameter to quantitatively evaluate optical thermometric ability of phosphors. S_a denotes the theoretical variation rate in fluorescence intensity ratio with respect to temperature and can be expressed by the equation below:

$$S_a = C * e^{(\frac{-\Delta E}{K_B T})} * e^{(\frac{\Delta E}{K_B T^2})} \quad (6.7)$$

where ΔE is the energy gap between Eu^{3+} successive energy levels, K_B is Boltzmann constant, and T is absolute temperature. The absolute temperature sensitivity of our LHOE NPs increases with the increasing measurement temperature and reaches a maximum value of 0.98 K^{-1} Figure 6.16(d).

Meanwhile, the relative temperature sensitivity (S_r) is another critical parameter to quantify the temperature sensing properties of thermometric materials. It is expressed by the equation below as the relative change of the integrated PL intensity (I) with respect to temperature (T):

$$S_r = \frac{1}{I}\frac{dI}{dT}\frac{C*e^{(\frac{-\Delta E}{K_B T})}}{B+ C*e^{(\frac{-\Delta E}{K_B T})}} * e^{\left(\frac{\Delta E}{K_B T^2}\right)} * 100\% \quad (6.8)$$

There is a gradual decrease of the S_r value with increasing measurement temperature for $^5D_0 - {}^7F_2$ transition of Eu^{3+} ions, which is similar to the trend observed from $GdVO_4:Sm^{3+}$.(Cai et al. 2017) The S_r value from the LHOE NPs reaches maximum of 3.53 $\%K^{-1}$, which is the highest compared with typical temperature sensors (Table 6.5). The high activation energy and relatively good thermal sensitivity of synthesized LHOE nanophosphors could be attributed to (a) low phonon energy of LHO, (b) high structural stability of LHO, and (c) little lattice strain or charge compensating defects as the majority of Eu^{3+} ions occupy La^{3+} sites due to similar ionic radii and the same charge.

Table 6.5. Relative temperature sensitivity S_r of representative optical thermometric materials

Materials	**Maximum S_r (%K^{-1})**	**Temperature range (K)**	**Ref.**
$Gd_2O_3:Er^{3+}$ /Yb^{3+}	0.39	300-900	(Singh et al. 2009)
$NaLuF_4:Ho^{3+}/Yb^{3+}$	0.12	350-750	(Zhou et al. 2014a)
$Yb_3Al_5O_{12}:Er^{3+}$	0.48	295-973	(Dong et al. 2012)
$NaLuF_4:Gd^{3+}$	0.29	298-523	(Zheng et al. 2013)
$Y_2MgTiO_6:Mn^{4+}$	0.14	10-513	(Cai et al. 2018)
$GdVO_4:Sm^{3+}$	1.41	393-603	(Cai et al. 2017)
$La_2Hf_2O_7:Eu^{3+}$	3.53	298-1073	This work

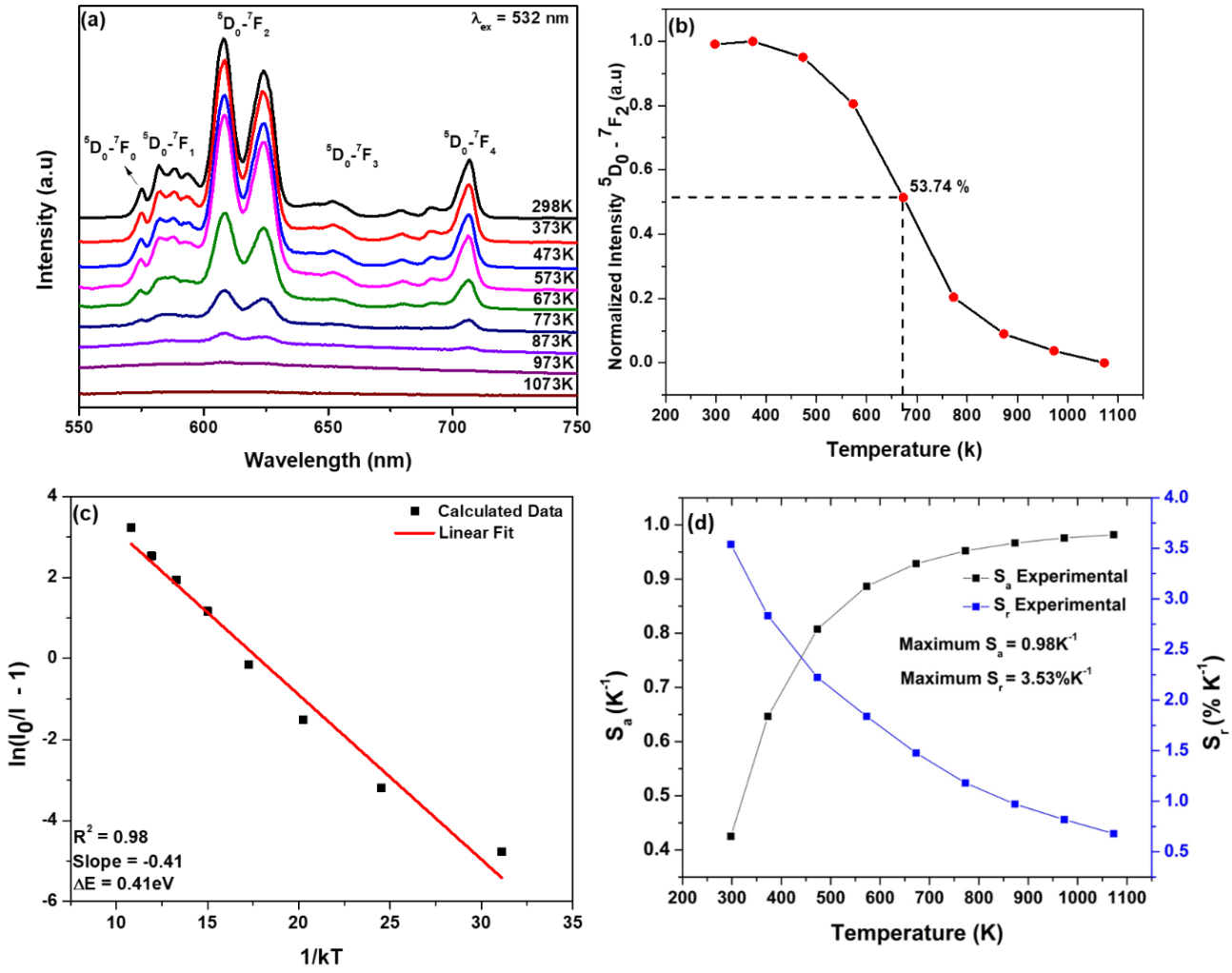

Figure 6.16: Optical Thermometry data (a) PL emission spectra at temperatures ranging from 298 to 1072 K. (b) Corresponding temperature dependence of the PL emission intensity of the $^5D_0 \rightarrow {}^7F_2$ transition. (c) Plot of $\ln(I_0/I - 1)$ versus $1/kT$ (d) Absolute sensitivity Sa and relative sensitivity Sr versus T for the LHOE NPs.

On the other hand, pressure dependence photoluminescence was explored to investigate how the LHOE NPs behave under high pressure. The ruby technique was utilized to deduce the pressure delivered to the sample. It can be seen from Figure 6.17 that at room temperature and no pressure the well-known peaks of europium are detected. As pressure increased the spectral peck corresponding to the electric dipole start to become without shape and loses it pronounce sharp peak characteristics and decrease of intensity compare to its magnetic dipole. At approximate of 22.81 GPa the shape of the europium ions starts to change from the electric dipole. After the pressure was released it can be noticed that the spectra regain some of it shape characteristics and became more pronounce. It's important to understand that the way that a material behaves under pressure it has to do with how much defects the material it has initially or as how was synthesized. All materials behave differently under pressure as seen in Figure 6.17(c) the asymmetric ration of the LHOE NPs starts to decrease as a function of pressure. This means that the Eu^{3+} ion environment becomes more symmetric under pressure and therefore the magnetic dipole of the Eu starts to overcome the electric dipole. Hence, why the material starts to emit orange light with increase in pressure as seen in Figure 6.17(d). These type of behavior under pressure for the LHOE is very important because it insinuates that the material becomes more stable with pressure. In Table 6.6, all the color parameters and temperatures can be found as a function of temperature as a support, with increasing pressure there's a color shift from red to orange because of the electric and magnetic dipole with high pressure indicating a more symmetric chemical environment.

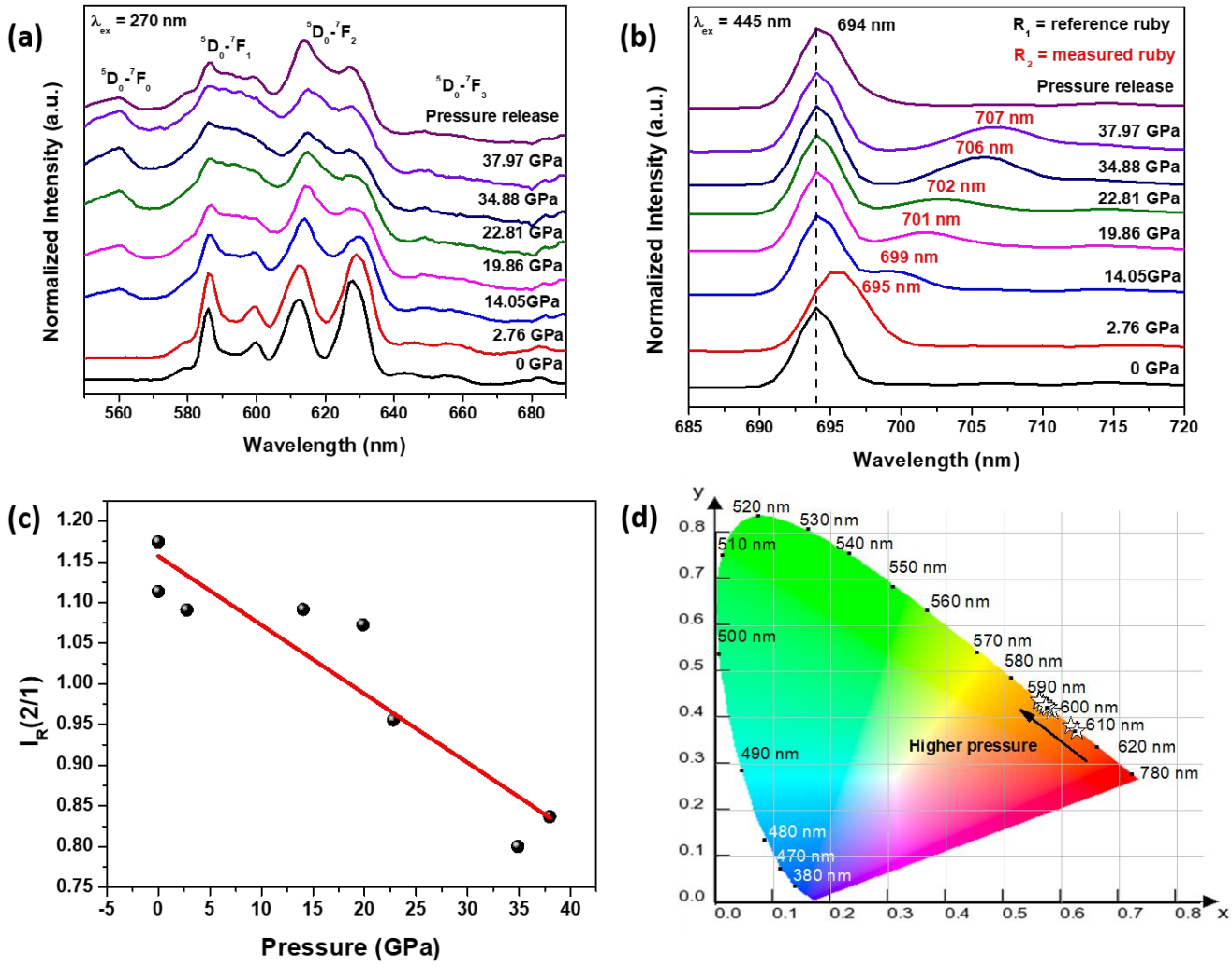

Figure 6.17: Pressure dependence photoluminescence data (a) PL emission spectra with pressures from 0 GPa to 37.97 GPa. (b) Emission spectra of Ruby as a reference to the corresponding pressures. (c) Asymmetric ratio as a function of pressure, (d) CIE index diagram for the LHOE NPs.

Table 6.6. Color parameters and temperatures as a function of pressure

Pressure (GPa)	(x, y)	Color Temp(K)
0	(0.61519, 0.38424)	1788
2.76	(0.62592, 0.37361)	1923
14.05	(0.58299, 0.41619)	1748
19.86	(0.57582, 0.42330)	1792
22.81	(0.56688, 0.43216)	1867
34.88	(0.55997, 0.43902)	1936
37.97	(0.56122, 0.43779)	1923
Pressure released	(0.57203, 0.42706)	1821

CHAPTER VII

STRUCTURAL AND PHASE TRANSFORMATION OF URANIUM DOPED $La_2Hf_2O_7$ NANOPARTICLES FOR NUCLEAR WASTE IMMOBILIZATION APPLICATIONS

7.1.1 Phase Transformation in Respect to Increase Doping of Uranium

It is well known that the ideal pyrochlore phase has six well-resolved Raman active vibrational modes in the range of 200-1000 cm^{-1} which are represented as $\Gamma_P = A_{1g} + E_g + 4F_{2g}$, whereas the fluorite phase has mainly one Raman active mode that is $\Gamma_F = F_{2g}$.(Turner et al. 2017) This is because seven oxygen ions are randomly distributed at eight anion positions, which leads to structural disordering in the fluorite phase, and hence all the fine peaks of pyrochlore collapsed into one broader peak. More specifically, phase transformation from $A_2B_2O_6O'$ pyrochlore (Fd-3m space group) to AO_2 fluorite (Fm3m, Z = 4) structure takes place through the disappearance of A_{1g} and E_g Raman modes and decrease in the number of F_{2g} modes from 4 to 1.

Radius ratio (r_A/r_B) plays an important role in determining which structure of $A_2B_2O_7$ compounds attain.(Subramanian et al. 1983a) It has been reported that fluorite phase is more likely to form if $r_A/r_B < 1.46$ and while ordered pyrochlore phase is more likely to be stabilized if r_A/r_B is greater than 1.46 at room temperature. It was propose that r_A/r_B for different $A_2B_2O_7$ compositions follows this trend: disordered fluorite phase (DFP) $r_A/r_B < 1.21 <$ Δ-phase $r_A/r_B < 1.42 - 1.44 <$ ordered pyrochlore phase (OPP) $r_A/r_B < 1.78 - 1.83 <$ monoclinic pyrochlore $r_A/r_B < 1.92$.(Stanek et al. 2009) $La_2Hf_2O_7$ is the most favorable candidate with radius ratio of 1.45 to be stabilized in pyrochlore phase. Figure 7.1a shows the Raman spectra of the as-

synthesized $La_2Hf_2O_7$:U NPs with different uranium concentrations. Undoped sample has six well-resolved Raman peaks at 306, 324, 402, 501, 521 and 601 cm^{-1} pertaining to the vibrations of La-O and Hf-O bonds. These peaks are assigned to F_{2g}, E_g, F_{2g}, A_{1g} F_{2g} and F_{2g} modes, respectively.(Garg et al. 2008a) The vibrational modes of F_{2g}, E_g, and F_{2g} at low frequency region of 300-400 cm^{-1} arise from vibrations of the La–O and Hf–O bonds. On the other hand, the high frequency band at 501, 522 and 601 cm^{-1} arise from the stretching of the Hf–O bonds.(Garg et al. 2008a) However, the complete pyrochlore phase is preserved only up to 1.0% uranium doping level. After that, the fine OPP structure starts to collapse into broader peaks and disordered fluorite phase or cotunnite phase evolves and coexists with OPP. At 2.5% uranium doping level and above, there is complete disordering of the $La_2Hf_2O_7$ pyrochlore phase and a broad peak around 715 cm^{-1} appears. Its intensity keeps increasing and even overpowers the broad fluorite peak at 7.5% and 10% uranium doping levels. This peak is not a fundamental Raman vibrational mode of pyrochlore-structured $A_2B_2O_7$ type oxides. It is believed to appear due to the distortions of the BO_6 octahedra.(De los Reyes et al. 2013, Garg et al. 2008a) In $La_2Hf_2O_7$, it has been attributed to distortion in HfO_6 octahedra and other kind of structural defects due to doping of uranium at La/Hf site. The average metal-oxygen bond lengths in the fluorite phase is close to those existing in ideal pyrochlore structure, but is relatively much smaller than those in cotunnite-type $A_2B_2O_7$ structure, suggesting that the fluorite phase has more covalent character than the cotunnite-type structure.(Xiao et al. 2010) In the cotunnite-type structure, coordination number of metal ions is generally 8- or 9-fold, whereas in the fluorite-type structures, metal ions coordinate with oxygen ion in 7- or 8-fold coordination. This suggests $La_2Hf_2O_7$ has the tendency to form ionic bonding with higher coordination number at high uranium doping concentration. Furthermore, based on Raman spectroscopy data, the increase of

uranium doping level induces the gradual phase transformation from pyrochlore to fluorite and then cotunnite as observed by the appearance of broad peaks at 307 and 715 cm^{-1}. Zhang *et al.* have also observed such process in U doped $Gd_2Zr_2O_7$ but by applying pressure of 22 GPa, which finally transformed into a disordered fluorite structure on release of pressure.(Zhang et al. 2014)

As a quantitative measure of the extent of anion disordering in the $La_2Hf_2O_7$:U NPs as a function of uranium doping concentration, the ratio of integrated Raman intensity between Raman active vibration mode of the distorted HfO_6 octahedra and the main F_{2g} Raman mode at $\omega_0 \approx 307\ cm^{-1}$ is plotted in Figure 7.1b.(Rittman et al. 2017) Moreover, we annealed our samples at high temperature to enhance cation ordering and reduce strain, but there was little effect on the Raman spectra of our $La_2Hf_2O_7$:U NPs.(Fuentes et al. 2005) Thus, this ratio selectively indicates disorder on the anion sub-lattice.

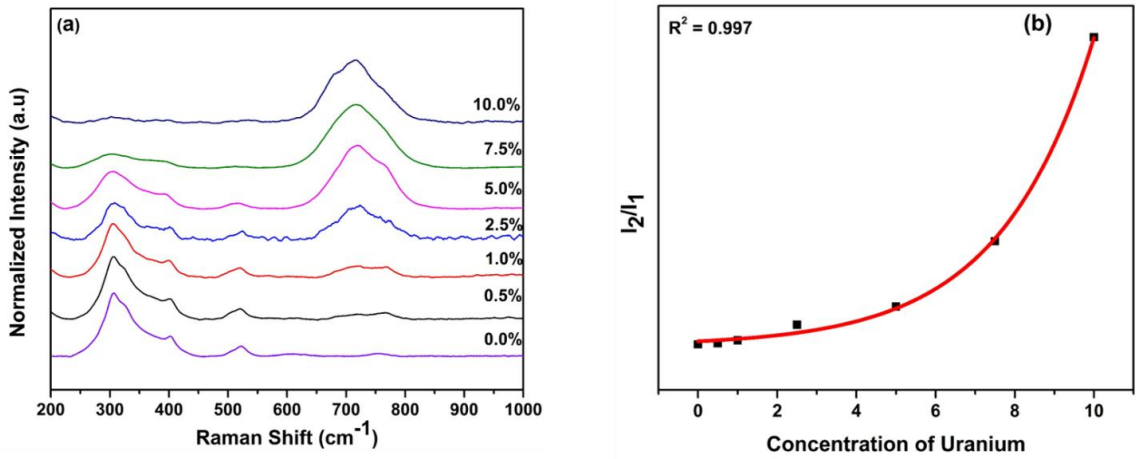

Figure 7.1: (a) Raman spectra of the $La_2Hf_2O_7$:x%U NPs (x = 0, 0.5, 1, 2.5, 5, 7.5, and 10) and (b) corresponding integrated Raman intensity ratio of the distorted HfO_6 octahedra (I_2) and the main F_{2g} Raman mode of the ordered pyrochlore (I_1). This Raman intensity ratio serves as a qualitative indicator of the progression of anion disorder as a function of uranium doping concentration in the $La_2Hf_2O_7$ host.

7.1.2 Investigating the Stabilization of Uranium Using Luminescence as a Structural Probe

Figure 7.2a depicts the emission spectra of the $La_2Hf_2O_7$:U NPs for various uranium concentrations and Figure 7.2b displayed the effect of uranium ion concentration on emission intensity for both U^{4+} emission at 458 nm and UO_6^{6-} emission at 550 nm. The emission intensity increases up to 1.0 % uranium doping, and after that, there is an emission intensity reduction. Such phenomenon is attributed to concentration quenching. At higher doping concentration, the distance between two-activator ions decreased to an extent where non-radiative energy transfer between them is facilitated. That distance in photophysical parlance is called critical distance. To confirm the non-radiative energy transfer mechanism, which leads to concentration quenching, critical distance (R_c) needs to be determined using the following equation:

$$R_c = 2\left(\frac{3V}{4\pi X_c N}\right)^{\frac{1}{3}} \quad (7.1)$$

where R_c is called critical distance and is defined as the minimum possible distance between the dopant ions at which non-radiative energy transfer takes place, V is the volume of the unit cell, X_c is the critical concentration of dopant ion, and N is the number of cations present in one formula unit of host. The values of V and N for $La_2Hf_2O_7$ are 1250.32 $Å^3$ and 16, respectively. Considering X_C = 1.0% (0.01), critical energy transfer distance R_c in the $La_2Hf_2O_7$:1.0%U NPs was estimated to be 24.62 Å. In this case, non-radiative energy transfer takes place at the U-U distance greater than 10 Å via electric multipolar interaction.

In addition, uranium was stabilized as both U^{4+} and UO_6^{6-} ions in all doping concentrations in the $La_2Hf_2O_7$ host, but their relative intensity changes (Figure 7.2a). At low concentrations, the fraction of U^{4+} is more than that of UO_6^{6-} whereas the trends reverses at high doping concentrations as plotted in Figure 7.2c. This in an interesting observation consistent with XPS data, which can be correlated to some kind of structural changes. At low uranium doping

, $A_2B_2O_7$ structure favors the stabilization of U^{4+} over that of UO_6^{6-}. At high doping level, $A_2B_2O_7$ structure favors UO_6^{6-} over U^{4+}. It has been reported that the structure of host materials plays huge roles in stabilizing different oxidation states and coordinations of doping ions. Perovskite structure tends to stabilize the U(VI) oxidation state in UO_6^{6-} coordination(Gupta et al. 2014b) whereas spinel structure tends to favor the same oxidation state but in a different geometry as UO_2^{2+} ion.(Gupta et al. 2017a) On the other hand, fluorite type $A_2B_2O_7$ composition favors the stabilization of both U^{4+} and U^{6+}.(Gupta et al. 2017c) In this case, our Raman spectroscopy results are assimilate our PL observations, supporting the fact that oxidation stabilization of uranium is dependent on the structural and phase evolution of the NPs.

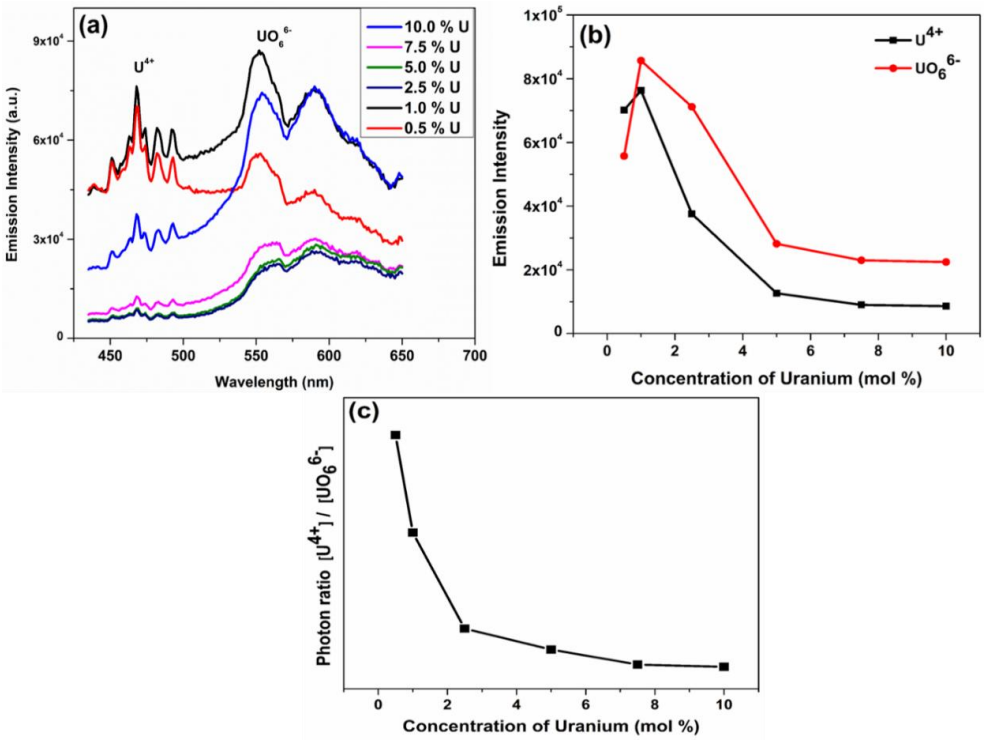

Figure 7.2. (a) Emission spectra of the $La_2Hf_2O_7$:U NPs with various uranium doping concentrations with λ_{ex} = 230 nm, and (b) corresponding plot of emission intensity and (c) ratio of emission intensity from the U^{4+} and UO_6^{6-} ions as a function of the uranium doping concentration.

7.1.3 Discovery of Reversible Phase Change Using In-Situ Raman Spectroscopy

To further investigate the structural evolution of our $La_2Hf_2O_7$:x%U NPs, we took in-situ Raman spectra of $La_2Hf_2O_7$:10%U NPs as an example with our initial effort. From the discussion above, the $La_2Hf_2O_7$:10%U NPs exists in complete cotunnite structure. The average metal-oxygen bond length in the fluorite-phase is much closer to those existing in ideal pyrochlore structures, but is relatively much smaller than that in cotunnite-type $A_2B_2O_7$ structures, suggesting that the fluorite phases have more covalent character than the cotunnite-type(Xiao et al. 2010). In the cotunnite-type structure though, coordination number of metal ion is generally 8 or 9-fold whereas in the fluorite-type structures metal ion coordinates with oxygen ion in 7- or 8-fold coordination. This suggest that at high uranium concentration hafnate pyrochlore has tendency to form ionic bonding with higher coordination number.

With increasing temperature from 25°C to 950°C (Figure 7.3), this particular the $La_2Hf_2O_7$:10%U sample underwent phase transformation from cotunnite phase to ordered pyrochlore phase. At the highest reached measurement temperature, i.e. 950°C, all the Raman modes expected for ordered pyrochlore phase were found from the heated sample with the almost complete disappearance of the 715 cm^{-1} peaks originated from the structurally disorder cotunnite phase (top panel of Figure 7.3a) while the disordered fluorite phase was probably unseen. The complete phase transformation took place around 900^oC. Even more interestingly and for the first time, we found that the phase change is reversible, i.e., the Raman band corresponding to cotunnite phase reappear after the sample was cooled down back to room temperature (Figure 7.3b). With the initial exciting Raman results collected so far, further investigations are undergoing, including in-situ Raman studies of other composition along with in-situ PL, X-ray absorption spectroscopy and neutron diffraction measurements, and will be reported separately soon.

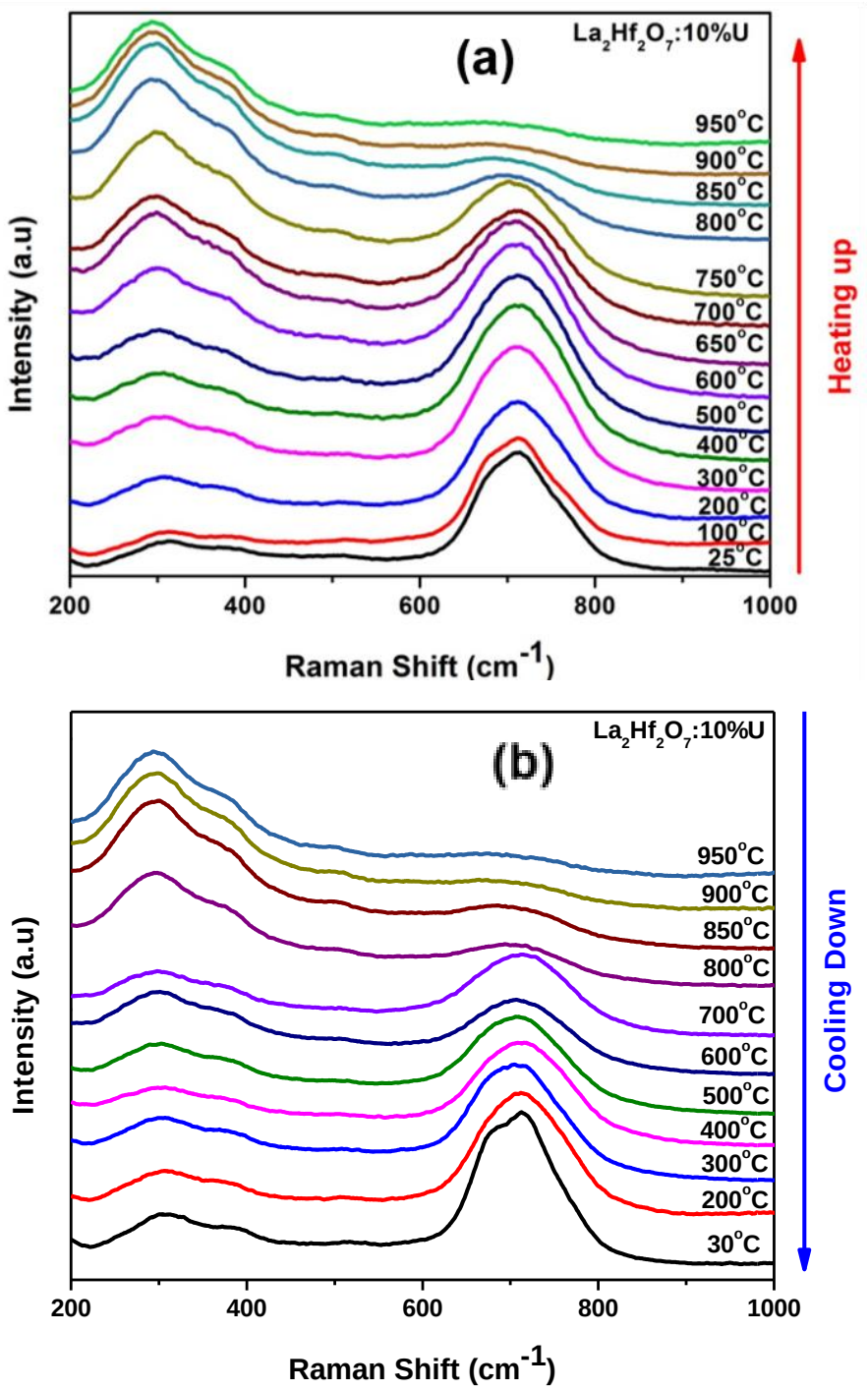

Figure 7.3: In-situ Raman spectra of the $La_2Hf_2O_7$:10%U NPs in consecutive heating and cooling cycle.

CHAPTER VIII

CONCLUSIONS

In order to further investigate the functionality of the $La_2Hf_2O_7$ nanoparticles we first had to optimize the synthesis parameters of the material through molten-salt method. We adjusted the synthesis parameters such as time, temperature and pH of titrant for optimum the structural and optical properties of the give nanomaterial. The molten-salt method has been utilized as a new green chemistry approach to generate simple and complex nanomaterial. By using a low temperature molten salt synthesis approach and its optimum parameters we engineered lanthanide ion doped $La_2Hf_2O_7$ NPs. The synthesized NPs was subjected to intense quality checkup for phase purity, structure and morphology using XRD, Raman spectroscopy and SEM. Single doped systems were taken in consideration before accommodating all three activator ions in the $La_2Hf_2O_7$ host. Europium, terbium and dysprosium were used as the activator ions due to its promising luminescent properties. LHOE, LHOT and LHOD displayed efficient photoluminescence and present red, green, blue-yellow emission under near UV irradiation. These NPs could successfully convert highly energetic X-ray beam into visible light paving its application as X-ray scintillator. Moreover, triply co-doped $La_2Hf_2O_7$:Eu^{3+}, Tb^{3+}, Dy^{3+} samples exhibit warm white luminescence with low CCT which can be highly beneficial for indoor lighting. The non-radiative energy transfer mechanism in case of LHOT and LHOD is a dipole−dipole interaction whereas dipole-quadruple interaction causes concentration quenching in LHOE. Lifetime spectroscopy suggested concentration depending site swapping in case of

LHOE and LHOD whereas in LHOT; Hf^{4+} is specifically occupied site. Moreover, the emission color can be adjusted from greenish white to yellowish white and CCT is also lowered manipulating the doping concentration. In addition, we explored a co-doped system were bismuth and europium were combined with the LHO host to create a composition the generated near to white light emission with color coordinates of (0.31, 0.32) and a color temperature close to the temperature of the light emitted by the sun. In addition, we explored the stability of the LHOE NPs under high temperatures and pressures. Here, it was found that the LHOE material is relatively stable under high temperatures up to 1070 K and high pressures ~40 GPa. The tunable photo-luminescent properties and radioluminescence properties of doped lanthanum hafnate nanoparticles show their great potential application in solid-state lighting, scintillator and multicolor luminescence devices.

In addition, we briefly touch on the exploration of $La_2Hf_2O_7$ as an effective host for nuclear waste. In this work, uranium doped $La_2Hf_2O_7$ nanoparticles were successfully synthesized using a combined co-precipitation and molten salt synthesis method. XRD and FTIR demonstrated the formation of pure $La_2Hf_2O_7$ phase with particle size in the nano-domain as confirmed using electron microscopy. Emission and lifetime spectroscopy further suggested the existence of U^{4+} ions along with U^{6+} ions as UO_6^{6-} species. The same has been further corroborated by more oxidation state sensitive XPS. Luminescence lifetime measurement confirmed the stabilization of fast decaying U^{4+} at Hf^{4+} site whereas slowly decaying U^{6+} tends to stabilize at La^{3+} site. Further concentration dependence studies showed maximum emission output for 1.0 % uranium doped samples and the concentration quenching in these NPs was attributed to non-radiative energy transfer via multipolar interaction. Another interesting phenomenon was observed from the emission spectra as well as XPS: at low uranium doping

concentration, the proportion of U^{4+} ion was more than that of U^{6+}, whereas at high uranium doping concentration, the opposite happened. We successfully explained this phenomenon using Raman spectroscopy, which demonstrated a structural phase transition from order pyrochlore to cotunnite with increasing uranium doping concentration. It was concluded that ordered pyrochlore phase favors uranium stabilization in +4-valence state whereas disordered cotunnite phase energetically favors octahedral uranate ions UO_6^{6-}. To further understand the structural evolution, in-situ Raman measurements were carried out on the $La_2Hf_2O_7$:10%U NPs between room temperature and 950^oC. A reversible structural transition was observed dueling the cooling cycle.

Overall, activated $La_2Hf_2O_7$ NPs has shown extraordinary potential to be used as a phosphor for multiple applications. This has been proven due to the amazing properties of the host such as low phonon count, high density, high dielectric constant, thermo/pressure structural stability, high quantum yield, and ability to dissolve actinides. This material can provide the next revolutionary component for solid state lighting, thermo/pressure sensor, radiation detection and an effective replacement of borosilicate for nuclear waste immobilization.

REFERENCES

A, K., Hull, R., Opila, R., Bawendi, R. L., Steigerwald, M. G., Carroll, M. L., Brus, P. J. & E., L. (1990). 'Nucleation and Growth of CdSe on ZnS Quantum Crystallite seeds, and vice versa; In Inverse Micelle Media.' *J. Am. Chem. Soc.*, 112, 1327-1332.

A, M. A. (1983). 'Positrons and solid state physics.' *Helvetica Physica Acta*, 56, 437-448.

Abd, H. R., Hassan, Z., Ahmed, N. M., Almessiere, M. A., Omar, A., Alsultany, F. H., Sabah, F. A. & Osman, U. S. (2018). 'Effect of Annealing Time of YAG:Ce^{3+} Phosphor on White Light Chromaticity Values.' *Journal of Electronic Materials*, 47, 1638-1646.

Ahmad, T. & Ganguli, A. K. (2004). 'Synthesis of nanometer-sized particles of barium orthotitanate prepared through a modified reverse micellar route: Structural characterization, phase stability and dielectric properties.' *Journal of Materials Research*, 19(10), 2905-2912.

Ahmad, T., Kavitha, G., Narayana, C. & Ganguli, A. K. (2005). 'Nanostructured Barium Titanate Prepared Through a Modified Reverse Micellar Route: Structural Distortion and Dielectric Properties.' *Journal of Materials Research*, 20(6), 1415-1421.

Ahmed, J. & Mao, Y. (2016). 'Synthesis, characterization and electrocatalytic properties of delafossite $CuGaO_2$.' *Journal of Solid State Chemistry*, 242(1), 77-85.

Ahmed, J. & Mao, Y. (2016). 'Ultrafine Iridium Oxide Nanorods Synthesized by Molten Salt Method toward Electrocatalytic Oxygen and Hydrogen Evolution Reactions.' *Electrochimica Acta*, 212, 686-693.

Ali, G., Lee, J. H., Chang, W., Cho, B.-W., Jung, H.-G., Nam, K.-W. & Chung, K. Y. (2017). 'Lithium intercalation mechanism into $FeF_3 \cdot 0.5H_2O$ as a highly stable composite cathode material.' *Scientific Reports*, 7, 42237.

Arachi, Y. & Nabeshima, D. (2014). 'Effect of fluorite phase on the electrical conductivity of $(Sm_{1-x}Dy_x)_2Zr_2O_7$ pyrochlore.' *Solid State Ionics*, 262, 536-539.

Binnemans, K. (2015). 'Interpretation of europium (III) spectra.' *Coordination Chemistry Reviews*, 295, 1-45.

Biswas, A., Maciel, G., Friend, C. & Prasad, P. (2003). 'Upconversion properties of a transparent Er^{3+}–Yb^{3+} co-doped LaF_3–SiO_2 glass-ceramics prepared by sol–gel method.' *Journal of non-crystalline solids*, 316(2-3), 393-397.

Bortolani, F. & Dorey, R. A. (2010). 'Molten salt synthesis of PZT powder for direct write inks.' *Journal of the European Ceramic Society,* 30(10), 2073-2079.

Boukerika, A. & Guerbous, L. (2014). 'Annealing effects on structural and luminescence properties of red Eu^{3+}-doped Y_2O_3 nanophosphors prepared by sol–gel method.' *Journal of Luminescence,* 145, 148-153.

Boutonnet, M., Kizling, J., Stenius, P. & Maire, G. (1982). 'The preparation of monodisperse colloidal metal particles from microemulsions.' *Colloids and Surfaces,* 5(3), 209-225.

Cai, J., Zhao, L., Hu, F., Wei, X., Chen, Y., Yin, M. & Duan, C.-K. (2017). 'Temperature sensing using thermal population of low-lying energy levels with $(Sm_{0.01}Gd_{0.99})$ VO_4.' *Inorganic chemistry,* 56, 4039-4046.

Cai, P., Qin, L., Chen, C., Wang, J., Bi, S., Kim, S. I., Huang, Y. & Seo, H. J. (2018). 'Optical Thermometry Based on Vibration Sidebands in $Y_2MgTiO_6:Mn^{4+}$ Double Perovskite.' *Inorganic chemistry,* 57, 3073-3081.

Cepeda-Sánchez, N., Fuentes, A., López-Cota, F., Rodríguez-Reyes, M. & Díaz-Guillén, J. (2015). 'Mechanochemical synthesis and electrical properties of $Gd_2Hf_{2-x}Zr_xO_7$ solid electrolytes for their use in SOFC's.' *Journal of Applied Electrochemistry,* 45, 1231-1237.

Chan, N.-H., Sharma, R. K. & Smyth, D. M. (1981). 'Nonstoichiometry in $SrTiO_3$.' *Journal of The Electrochemical Society,* 128(8), 1762-1769.

Chang, Y., Wu, J., Zhang, M., Kupp, E. & Messing, C. L. (2017). 'Molten salt synthesis of morphology controlled alpha-alumina platelets ' *Ceramics International,* 43(15), 12684-1288.

Chavan, S. V. & Tyangi, A. K. (2004). 'Preparation and characterization of $Sr_{0.09}Ce_{0.91}O_{1.91}$, $SrCeO_3$, and Sr_2CeO_4 by glycine–nitrate combustion: Crucial role of oxidant-to-fuel ratio.' *Journal of Material Research,* 19(11), 3181-3188.

Chemingui, S., Ferhi, M., Horchani-Naifer, K. & Férid, M. (2015). 'Synthesis and luminescence characteristics of Dy^{3+} doped $KLa(PO_3)_4$.' *J. Lumin,* 166, 82-87.

Cho, U., Riordan, D. P., Ciepla, P., Kocherlakota, K. S., Chen, J. K. & Harbury, P. B. (2018). 'Ultrasensitive optical imaging with lanthanide lumiphores.' *Nature chemical biology,* 14, 15.

Cullity, B. D. (1956). 'Elements of X-ray diffraction.' *Addison-Wesley Pub. Co,* 16.

Cushing, B. L., Kolesnichenko, V. L. & O'Connor, C. J. (2004). 'Recent Advances in the Liquid-Phase Syntheses of Inorganic Nanoparticles.' *Chem. Rev,* 104, 3893-3946.

Dai, Q., Song, H., Wang, M., Bai, X., Dong, B., Qin, R., Qu, X. & Zhang, H. (2008). 'Size and Concentration Effects on the Photoluminescence of $La_2O_2S:Eu^{3+}$ Nanocrystals.' *J. Phys. Chem. C,* 112, 19399-19404.

De los Reyes, M., Whittle, K. R., Zhang, Z., Ashbrook, S. E., Mitchell, M. R., Jang, L.-Y. & Lumpkin, G. R. (2013). 'The pyrochlore to defect fluorite phase transition in $Y_2Sn_{2-x}Zr_xO_7$.' *RSC Advances,* 3, 5090-5099.

Dept. of Chemistry and Biochemitry, U. o. O. (2016). 'X-Ray Generation.'

Dong, B., Cao, B., He, Y., Liu, Z., Li, Z. & Feng, Z. (2012). 'Temperature Sensing and In Vivo Imaging by Molybdenum Sensitized Visible Upconversion Luminescence of Rare-Earth Oxides.' *Advanced Materials,* 24, 1987-1993.

Du, M.-H. (2015a). 'Mn^{4+} emission in pyrochlore oxides.' *Journal of Luminescence,* 157, 69-73.

Eagleman, Y., Weber, M., Chaudhry, A. & Derenzo, S. (2012). 'Luminescence study of cerium-doped $La_2Hf_2O_7$: Effects due to trivalent and tetravalent cerium and oxygen vacancies.' *Journal of Luminescence,* 132, 2889-2896.

Eagleman, Y., Weber, M. & Derenzo, S. (2013). 'Luminescence study of oxygen vacancies in lanthanum hafnium oxide, $La_2Hf_2O_7$.' *Journal of Luminescence,* 137, 93-97.

Fazli, R., Fazli, M., Safaei-Naeini, Y. & F.Golestani-Fard (2013). 'The effects of processing parameters on formation of nano-spinel ($MgAl_2O_4$) from LiCl molten salt.' *Ceramics International,* 39(6), 6265-6270.

Fu, Z., Zhou, S., Pan, T. & Zhang, S. (2007). 'Preparation and luminescent properties of cubic $Eu^{3+}:Y_2O_3$ nanocrystals and comparison to bulk $Eu^{3+}:Y_2O_3$.' *Journal of Luminescence,* 124, 213-216.

Fuentes, A. F., Boulahya, K., Maczka, M., Hanuza, J. & Amador, U. (2005). 'Synthesis of disordered pyrochlores, $A_2Ti_2O_7$ (A= Y, Gd and Dy), by mechanical milling of constituent oxides.' *Solid State Sciences,* 7, 343-353.

Gao, Y., Sun, Y., Zou, H., Sheng, Y., Zhou, X., Zhang, B. & Zhou, B. (2016). 'Effect of Eu^{3+} doping on the structural and photoluminescence properties of cubic $CaCO_3$.' *Mater. Sci. Eng. B,* 203, 52-58.

Garg, N., Pandey, K., Murli, C., Shanavas, K., Mandal, B. P., Tyagi, A. & Sharma, S. M. (2008). 'Decomposition of lanthanum hafnate at high pressures.' *Physical Review B,* 77, 214105.

Gilbert, M. R. (2016). 'Molten salt synthesis of titanate pyrochlore waste-forms.' *Ceramics International,* 42(4), 5263-5270.

Grafutin, V. I. & Prokop'ev, E. P. (2002). 'Positron annihilation spectroscopy in materials structure studies ' *UFN*, 172(1), 67-83.

Gu, S., Zhang, S., Xue, B., Yan, J., Li, W. & Zhang, L. (2018). 'Phase variation and thermophysical properties of $La_2Hf_2O_7$ with alumina addition.' *J. Eur. Ceram. Soc.*, 38, 1938-1945.

Guan, H., Sheng, Y., Song, Y., Xu, C., Zhou, X., Zheng, K., Shi, Z. & Zou, H. (2017). 'YF_3:RE^{3+} (RE = Dy, Tb, Eu) Sub-microstructures: Controllable Morphology, Tunable Multicolor, and Thermal Properties.' *J. Phys. Chem. C*, 121, 23080-23095.

Guo, N., Zheng, Y., Jia, Y., Qiao, H. & You, H. (2012). 'Warm-White-Emitting from Eu^{2+}/Mn^{2+}-Codoped $Sr_3Lu(PO_4)_3$ Phosphor with Tunable Color Tone and Correlated Color Temperature.' *J.Phys. Chem. C*, 116, 1329-1334.

Gupta, S. K., Ghosh, P., Reghukumar, C., Pathak, N. & Kadam, R. (2016). 'Experimental and theoretical approach to account for green luminescence from $Gd_2Zr_2O_7$ pyrochlore: exploring the site occupancy and origin of host-dopant energy transfer in $Gd_2Zr_2O_7$: Eu^{3+}.' *RSC Advances*, 6, 44908-44920.

Gupta, S. K., Ghosh, P. S., Yadav, A. K., Jha, S. N., Bhattacharyya, D. & Kadam, R. M. (2016). 'Origin of Blue-Green Emission in α-$Zn_2P_2O_7$ and Local Structure of Ln^{3+} Ion in α-$Zn_2P_2O_7$: Ln^{3+} (Ln= Sm, Eu): Time-Resolved Photoluminescence, EXAFS, and DFT Measurements.' *Inorganic chemistry*, 56, 167-178.

Gupta, S. K., Ghosh, P. S., Yadav, A. K., Pathak, N., Arya, A., Jha, S. N., Bhattacharyya, D. & Kadam, R. M. (2016). 'Luminescence properties of $SrZrO_3$/Tb^{3+} perovskite: host-dopant energy-transfer dynamics and local structure of Tb3+.' *Inorganic chemistry*, 55(4), 1728-1740.

Gupta, S. K., Grover, V., Shukla, R., Srinivasu, K., Natarajan, V. & Tyagi, A. K. (2016). 'Exploring pure and RE co-doped (Eu^{3+}, Tb^{3+} and Dy^{3+}) gadolinium scandate: Luminescence behaviour and dynamics of energy transfer.' *Chem. Eng. J*, 283, 114-126.

Gupta, S. K., Kadam, R. M., Natarajan, V. & Godbole, S. V. (2014). 'Nanoparticles of $Sr_{0.995}Gd_{0.005}ZrO_3$-gel-combustion synthesis, characterization, fluorescence and EPR spectroscopy.' *Mater. Sci. Eng. B*, 183, 6-11.

Gupta, S. K., Mohapatra, M., Godbole, S. & Natarajan, V. (2013). 'On the unusual photoluminescence of Eu^{3+} in α-$Zn_2P_2O_7$: a time resolved emission spectrometric and Judd–Ofelt study.' *RSC Advances*, 3(43), 20046-20053.

Gupta, S. K., Mohapatra, M., Kaity, S., Natarajan, V. & Godbole, S. (2012). 'Structure and site selective luminescence of sol–gel derived Eu:Sr_2SiO_4.' *Journal of Luminescence*, 132, 1329-1338.

Gupta, S. K., Mohapatra, M., Natarajan, V. & Godbole, S. (2012). 'Site-specific luminescence of Eu^{3+} in gel-combustion-derived strontium zirconate perovskite nanophosphors.' *Journal of Materials Science,* 47, 3504-3515.

Gupta, S. K., Pathak, N., Ghosh, P. & Kadam, R. (2017). 'On the photophysics and speciation of actinide ion in $MgAl_2O_4$ spinel using photoluminescence spectroscopy and first principle calculation: A case study with uranium.' *Journal of Alloys and Compounds,* 695, 337-343.

Gupta, S. K., Pathak, N., Gupta, R., Thulasidas, S. & Natarajan, V. (2014). 'Probing the oxidation state and coordination geometry of uranium ion in $SrZrO_3$ perovskite.' *Journal of Molecular Structure,* 1068, 204-09.

Gupta, S. K., Rajeshwari, B., Achary, S., Patwe, S., Tyagi, A., Natarajan, V. & Kadam, R. (2015). 'Europium Luminescence as a Structural Probe: Structure- Dependent Changes in Eu^{3+}- Substituted $Th(C_2O_4)_2 \cdot xH_2O$ (x= 6, 2, and 0).' *European Journal of Inorganic Chemistry,* 2015, 4429-4436.

Gupta, S. K., Reghukumar, C. & Kadam, R. (2016). 'Eu^{3+} local site analysis and emission characteristics of novel $Nd_2Zr_2O_7$:Eu phosphor: insight into the effect of europium concentration on its photoluminescence properties.' *RSC Advances,* 6, 53614-53624.

Gupta, S. K., Reghukumar, C., Keskar, M. & Kadam, R. (2016). 'Revealing the oxidation number and local coordination of uranium in $Nd_2Zr_2O_7$ pyrochlore: A photoluminescence study.' *Journal of Luminescence,* 177, 166-171.

Gupta, S. K., Reghukumar, C., Pathak, N., Sudarshan, K., Tyagi, D., Mohapatra, M., Pujari, P. & Kadam, R. (2017). 'Speciation of uranium and doping induced defects in $Gd_{1.98}U_{0.02}Zr_2O_7$: Photoluminescence, X-ray photoelectron and positron annihilation lifetime spectroscopy.' *Chemical Physics Letters,* 669, 245-250.

Gupta, S. K., Sahu, M., Ghosh, P., Tyagi, D., Saxena, M. & Kadam, R. (2015). 'Energy transfer dynamics and luminescence properties of Eu^{3+} in $CaMoO_4$ and $SrMoO_4$.' *Dalton Transactions,* 44, 18957-18969.

Gupta, S. K., Sudarshan, K., Ghosh, P., Sanyal, K., Srivastava, A., Arya, A., Pujari, P. & Kadam, R. (2016). 'Luminescence of undoped and Eu^{3+} doped nanocrystalline $SrWO_4$ scheelite: time resolved fluorescence complimented by DFT and positron annihilation spectroscopic studies.' *RSC Advances,* 6, 3792-3805.

Gupta, S. K., Sudarshan, K., Ghosh, P., Srivastava, A., Bevara, S., Pujari, P. & Kadam, R. (2016). 'Role of various defects in the photoluminescence characteristics of nanocrystalline $Nd_2Zr_2O_7$: An introspection through spectroscopic and DFT calculations.' *Journal of Materials Chemistry C,* 4(22), 4988-5000.

Gupta, S. K., Sudarshan, K., Ghosh, P. S., Mukherjee, S. & Kadam, R. M. (2016). 'Doping-induced room temperature stabilization of metastable β-Ag_2WO_4 and origin of visible emission in α-and β-Ag_2WO_4: low temperature photoluminescence studies.' *J. Phys. Chem. C,* 120, 7265-7276.

Gupta, S. K., Sudarshan, K. & Kadam, R. M. (2017). 'Tunable white light emitting $Sr_2V_2O_7$:Bi^{3+}phosphors: Role of bismuth ion.' *Mater. Des.*, 130, 208-214.

Gupta, S. K., Sudarshan, K., Srivastava, A. & Kadam, R. (2017). 'Visible light emission from bulk and nano $SrWO_4$: Possible role of defects in photoluminescence.' *Journal of Luminescence,* 192, 1220-1226.

Gupta, S. K., Sudarshan, K., Yadav, A. K., Gupta, R., Bhattacharyya, D., Jha, S. N. & Kadam, R. M. (2018). 'Deciphering the Role of Charge Compensator in Optical Properties of $SrWO_4$:Eu^{3+}: A (A= Li^+, Na^+, K^+): Spectroscopic Insight Using Photoluminescence, Positron Annihilation, and X-ray Absorption.' *Inorganic Chemistry,* 57, 821-832.

Gupta, S. K., Zuniga, J. P., Abdou, M. & Mao, Y. (2018). 'Thermal annealing effects on $La_2Hf_2O_7$:Eu^{3+} nanoparticles: A curious case study of structural evolution and site-specific photo- and radio-luminescence.' *Inorganic Chemistry Frontiers*.

Gupta, S. K., Zuniga, J. P., Ghosh, P. S., Abdou, M. & Mao, Y. (2018). 'Correlating Structure and Luminescence Properties of Undoped and $La_2Hf_2O_7$:Eu^{3+}NPs Prepared with Different Coprecipitating pH Values through experimental and theoretical studies.' *Inorganic Chemistry*.

H, H. & R, H. (1997). 'Microemulsion mediated synthesis of ternary and quaternary nanoscale mixed oxide ceramic powders.' *Nanostructured materials,* 9, 241-244.

H.H, R. (2008). 'Optics of high-perfonance electron Micorscopes.' *Science and Technology of Advanced Materials,* 9(1), 014107.

Hailili, R., Wang, C. & Lichtfouse, E. (2018). 'Perovskite nanostructures assembled in molten salt based on halogen anions KX (X = F, Cl and Br): Regulated morphology and defect-mediated photocatalytic activity.' *Applied Catalysis B: Enviromental,* 232, 531-543.

Han, S., Qin, X., An, Z., Zhu, Y., Liang, L., Han, Y., Huang, W. & Liu, X. (2016). 'Multicolour synthesis in lanthanide-doped nanocrystals through cation exchange in water.' *Nature Communications,* 7.

Hashem, E., Platts, J. A., Hartl, F. e., Lorusso, G., Evangelisti, M., Schulzke, C. & Baker, R. J. (2014). 'Thiocyanate complexes of uranium in multiple oxidation states: A combined structural, magnetic, spectroscopic, spectroelectrochemical, and theoretical study.' *Inorganic Chemistry,* 53, 8624-8637.

Hench, L. L. & West, J. K. (1990). 'The sol-gel process.' *Chemical Reviews,* 90(1), 33-72.

Hirayama, M., Sonoyama, N., Yamada, A. & Kanno, R. (2008). 'Relationship between structural characteristics and photoluminescent properties of $(La_{1-x}Eu_x)_2M_2O_7$ (M=Zr, Hf, Sn) pyrochlores.' *J. Lumin,* 128, 1819-1825.

Huang, Z., Duan, H., Liu, J. & zhang, H. (2016). 'Preparation of lanthanum cerate powders via a simple molten salt route.' *Ceramics International,* 42(8), 10482-10486.

Huang, Z., Li, B. & Liu, J. 2010. ' Molten-Salt Synthesis of Oxyapatite $La_{9.33}Si_6O_{26}$ Powders as Electrolytes for Intermediate Temperature Solid Oxide Fuel Cells.' *Physica status solidi A - Applicationand Materials science,* 207(10), 2247-2251.

Huang, Z., Li, F., Jiao, C., Liu, J., Huang, J., Lu, L., Zhang, H. & Zhang, S. (2016). 'Molten salt synthesis of $La_2Zr_2O_7$ ultrafine powders.' *Ceramics International,* 42(5), 6221-6227.

Ilhan, M., Samur, R., Demirer, H. & Mindivan, F. (2015). 'Photoluminescence and concentration quenching of Pr^{3+} doped $BaTa_2O_6$ phosphor.' *Metalurgija,* 54, 407-410.

Im, H. J., Saengkerdsub, S., Stephan, A. C., Pawel, M. D., Holcomb, D. E. & Dai, S. (2004). 'Transparent Solid- State Lithiated Neutron Scintillators Based on Self- Assembly of Polystyrene- block- poly (ethylene oxide) Copolymer Architectures.' *Advanced materials,* 16(19), 1757-1761.

Ji, Y.-M., Jiang, D.-y. & Shi, J.-l. (2005). 'Preparation and spectroscopic properties of $La_2Hf_2O_7$/Tb.' *Materials Letters,* 59, 868-71.

Ji, Y., Jiang, D. & Shi, J. (2005). '$La_2Hf_2O_7$:Ti^{4+} ceramic scintillator for x-ray imaging.' *Journal of materials research,* 20, 567-570.

Jung, K. Y., Lee, C. H. & Kang, Y. C. (2005). 'Effect of surface area and crystallite size on luminescent intensity of Y_2O_3:Eu phosphor prepared by spray pyrolysis.' *Mater. Lett.,* 59, 2451-2456.

Kahouadji, B., Guerbous, L., Boukerika, A., Dolić, S. D., Jovanović, D. J. & Dramićanin, M. D. (2017). 'Sol gel synthesis and pH effect on the luminescent and structural properties of YPO_4:Pr^{3+} nanophosphors.' *Opt. Mater.,* 70, 138-143.

Kakihana, M. (1996). 'Invited review “sol-gel” preparation of high temperature superconducting oxides.' *Journal of Sol-Gel Science and Technology,* 6(1), 7-55.

Kakihana, M. & Arima, M. (1999(. 'Spectroscopic Characterization of Precursors Used in the Pechini-Type Polymerizable Complex Processing of Barium Titanate.' *Chemistry of Materials,* 11(2), 438-450.

Kelly, T. M. & Quick, N. R. (2008). 'Positron annihilation in AgBr microcrystals.' *Journal of Applied Physics,* 46(8), 3278.

Kesanli, B., Hong, K., Meyer, K., Im, H.-J. & Dai, S. (2006). 'Highly efficient solid-state neutron scintillators based on hybrid sol-gel nanocomposite materials.' *Applied physics letters*, 89(21), 214104.

Kim, J., Shih, P.-C., Tsao, K.-C., Pan, Y.-T., Yin, X., Sun, C.-J. & Yang, H. (2017). 'High-performance pyrochlore-type yttrium ruthenate electrocatalyst for oxygen evolution reaction in acidic media.' *Journal of the American Chemical Society*, 139, 12076-12083.

Kim, Y. H., Arunkumar, P., Kim, B. Y., Unithrattil, S., Kim, E., Moon, S.-H., Hyun, J. Y., Kim, K. H., Lee, D. & Lee, J.-S. (2017). 'A zero-thermal-quenching phosphor.' *Nature materials*, 16, 543.

Kimura, T. 2011. 'Molten Salt Synthesis of Ceramic Powders ' *InTech*, Chapter 4, 75-100.

Kimura, T., Machida, M., Yamaguchi, T. & Newnham, R. E. (1983). ' Products of Reaction Between PbO and Nb_2O_5 in Molten KCl or NaCl.' *Journal of the American Ceramic Society*, 66(10), 195-197.

Kong, L., Zhang, Z., de los Reyes, M., Karatchevtseva, I., Lumpkin, G. R., Triani, G. & Aughterson, R. D. (2015). 'Soft chemical synthesis and structural characterization of $Y_2Hf_xTi_{2-x}O_7$.' *Ceramics International*, 41, 5309-5317.

Kumar, S. A. & Senthilselvan, J. (2017). 'Effect of calcination temperatures on Green luminescence of Ce:YAG nanophosphor prepared by modified co-precipitation method.' Paper presented at AIP Conference Proceedings.

Kumar, V., Ntwaeaborwa, O. M., Soga, T., Dutta, V. & Swart, H. C. (2017). 'Rare Earth Doped Zinc Oxide Nanophosphor Powder: A Future Material for Solid State Lighting and Solar Cells.' *ACS Photonics*, 4, 2613-2637.

Kutty, K. G., Asuvathraman, R., Madhavan, R. R. & Jena, H. (2005). 'Actinide immobilization in crystalline matrix: a study of uranium incorporation in gadolinium zirconate.' *Journal of Physics and Chemistry of Solids*, 66, 596-601.

Li, G., Yu, M., Wang, Z., Lin, J., Wang, R. & Fang, J. (2006). 'Sol–gel fabrication and photoluminescence properties of SiO_2@ Gd_2O_3:Eu^{3+} core–shell particles.' *Journal of nanoscience and nanotechnology*, 6(5), 1416-1422.

Li, P., Wang, Z., Yang, Z. & Guo, Q. (2014). 'A novel, warm, white light-emitting phosphor Ca_2PO_4Cl:Eu^{2+}, Mn^{2+} for white LEDs.' *J. Mater. Chem. C*, 2, 7823-7829.

Liang, J., Zhao, S., Yuan, X. & Li, Z. (2018). 'A novel double perovskite tellurate Eu^{3+}-doped Sr_2MgTeO_6 red-emitting phosphor with high thermal stability.' *Opt. Laser. Tech.*, 101, 451-456.

Liao, Y. K., Jiang, D. Y., Ji, Y. M. & Shi, J. L. (2005). 'Combustion synthesis of nanosized $Y_2Hf_2O_7$ and $Lu_2Hf_2O_7$ powders.' Paper presented at Key Engineering Materials.

Lisiecki, I. & Pileni, M. P. (1993). 'Synthesis of copper metallic clusters using reverse micelles as microreactors.' *Journal of the American Chemical Society,* 115(10), 3887-3896.

Liu, J. R., Hong, R. Y., Feng, W. G., D.Badami & Wang, Y. Q. (2014). 'Large scale production of strontium ferrite by molten salt assited coprecipitation.' *Powder Technology,* 262, 142-149.

Liu, S., Han, W., Cui, B., Liu, X., Zhao, F., Stuart, J. & Licht, S. (2017). 'A novel rechargeable zinc-air battery with molten salt electrolyte.' *Journal of Power Sources,* 342, 435-441.

Liu, X., Fechler, N. & Antonietti, M. (2013). 'Salt melt synthesis of ceramics, semiconductors and carbon nanostructures.' *Chemical Society Reviews,* 42(21), 8237-8265.

Livage, J., Henry, M. & Sanchez, C. (1988). 'Sol-gel chemistry of transition metal oxides.' *Progress in Solid State Chemistry,* 18:4, 259-341.

Lu, C., Lu, Z., Wang, X., Xie, R., Li, Z., Higgins, M., Liu, C., Gao, F. & Wang, L. (2017). 'Enhanced Radiation-tolerant Oxide Dispersion Strengthened Steel and its Microstructure Evolution under Helium-implantation and Heavy-ion Irradiation.' *Scientific Reports,* 7, 40343.

Lu, X., Hou, C., Xie, Y., Shu, X., Ding, Y., Ma, D., Ren, W. & Bian, L. (2017). 'High capacity immobilization of U_3O_8 in $Gd_2Zr_2O_7$ ceramics via appropriate occupation designs.' *Ceramics International,* 43, 3015-3024.

Luwang, M. N., Ningthoujam, R., Srivastava, S. & Vatsa, R. (2010). 'Effects of Ce^{3+} codoping and annealing on phase transformation and luminescence of Eu^{3+}-doped YPO_4 nanorods: D_2O solvent effect.' *Journal of the American Chemical Society,* 132, 2759-2768.

Mani, R., Jiang, H., Gupta, S. K., Li, Z. & Duan, X. (2018). 'Role of Synthesis Method on Luminescence Properties of Europium (II, III) Ions in β-Ca_2SiO_4: Probing Local Site and Structure.' *Inorganic Chemistry,* 57, 935-950.

Mao, Y. (2012). 'Facile synthesis of ferromagnetic double perovskite oxide La_2BMnO_6 nanoparticles.' *RSC Advances,* 2(33), 12675-12678.

Mao, Y., Guo, X., Huang, J. Y., Wang, K. L. & Chang, J. P. (2009). 'Luminescent Nanocrystals with $A_2B_2O_7$ Composition Synthesized by a Kinetically Modified Molten Salt Method.' *The Journal of Physical Chemistry C,* 113(4), 1204-1208.

Mao, Y., Park, T.-J. & Wong, S. S. (2005). 'Synthesis of classes of ternary metal oxide nanostructures.' *Chemical Communications,* 0(46), 5721-5735.

Mao, Y., Park, T.-J., Zhang, F., Zhou, H. & Wong, S. S. (2007). 'Environmentally friendly methodologies for nanostructure synthesis.' *Small,* 3(7), 1122-1139.

Mao, Y. & Wong, S. S. (2005). 'Reproducible composition and shape control of crystalline $Ca_{1-x}Sr_xTiO_3$ perovskite nanoparticles.' *Advanced Materials,* 17(18), 2194-2199.

Mao, Y., Zhou, H. & Wong, S. S. (2010). 'Perovskite-phase metal oxide nanostructures: synthesis, properties, and applications.' *Material Matters,* 5, 50-53.

Martel, L., Naji, M., Popa, K., Vigier, J.-F. & Somers, J. (2017). 'Fingerprint of local disorder in long range ordered isometric pyrochlores.' *Scientific Reports,* 7, 12269.

Martirosyan, K., Avakyan, P. & Nersesyan, M. (2001). 'Synthesis of lead ferrite in a combustion mode.' *Int. J. SHS.,* 10:2, 193-199.

Martirosyan, K., Avakyan, P. & Nersesyan, M. (2002). 'Phase-formation during self-propagating high-temperature synthesis of ferrites.' *Inorgan.Mater.,* 38(4), 489-492.

Martirosyan, K., Wang, L., Luss, D. & Vicent, A. (2009). 'Fabrication of bismuth trioxide nanoparticles for gas-generators applications.' *NanoTech.,* 2, 82-85.

McCamy, C. S. (1992). 'Correlated color temperature as an explicit function of chromaticity coordinates.' *Color Research & Application,* 17, 142-144.

Mehlenbacher, R. D., Kolbl, R., Lay, A. & Dionne, J. A. (2017). 'Nanomaterials for in vivo imaging of mechanical forces and electrical fields.' *Nature Reviews Materials,* 3, 17080.

Mehrotra, R. C. & Singh, A. (1997). 'Recent Trends in Metal Alkoxide Chemistry.' *Progress in Inorganic Chemistry,* 92(46), 239-274.

Melato, L., Motaung, T., Ntwaeaborwa, O. & Motloung, S. (2017). 'Effect of annealing at different time intervals on the structure, morphology and luminescent properties of $MgAl_2O_4$:0.3%In^{3+} nanophosphor prepared by citrate sol-gel method.' *Optical Materials,* 66, 319-326.

Meltzer, R., Feofilov, S., Tissue, B. & Yuan, H. (1999). 'Dependence of fluorescence lifetimes of Y_2O_3:Eu^{3+} nanoparticles on the surrounding medium.' *Physical Review B,* 60, R14012.

Menon, S. G., Choudhari, K., Shivashankar, S., Santhosh, C. & Kulkarni, S. D. (2017). 'Rapid annealing: A novel processing technique for Cr:$ZnAl_2O_4$ nanoparticles.' *Journal of Alloys and Compounds,* 728, 484-489.

Min, X., Sun, Y., Kong, L., Guan, M., Fang, M., Liu, Y. g., Wu, X. & Huang, Z. (2018). 'Novel pyrochlore-type $La_2Zr_2O_7$:Eu^{3+} red phosphors: Synthesis, structural, luminescence properties and theoretical calculation.' *Dyes and Pigments,* 157, 47-54.

MindTouch (2017). 'Powder X-ray Diffraction ' *Chemistry LibreTexts*.

Mohapatra, M., Rajeswari, B., Hon, N. & Kadam, R. (2016). 'Uranium luminescence in $La_2Zr_2O_7$: effect of concentration and annealing temperature.' *Luminescence,* 31, 1519-1523.

Motloung, S., Motloung, S., Swart, H. & Hlatshwayo, T. T. (2018). 'The Effect of Annealing Time on the Structural and Optical Properties of $ZnAl_2O_4$:0.01%Cr^{3+} Nanophosphor Prepared via the Sol–Gel Method.' *Journal of Electronic Materials,* 47, 521-529.

Motloung, S. V., Kumari, P., Koao, L. F., Motaung, T. E., Hlatshwayo, T. T. & Mochane, M. J. (2018). 'Effects of annealing time on the structure and optical properties of $ZnAl_2O_4$/ZnO prepared via citrate sol-gel process.' *Materials Today Communications,* 14, 294-301.

Natrajan, L. S. (2012). 'Developments in the photophysics and photochemistry of actinide ions and their coordination compounds.' *Coordination Chemistry Reviews,* 256, 1583-1603.

Nguyen, T. M. H., Sandilands, L. J., Sohn, C., Kim, C., Wysocki, A. L., Yang, I.-S., Moon, S., Ko, J.-H., Yamaura, J. & Hiroi, Z. (2017). 'Two-magnon scattering in the 5d all-in-all-out pyrochlore magnet $Cd_2Os_2O_7$.' *Nature Communications,* 8, 251.

Osseo-Asare, K. & Arriagada, F. J. (1999). 'Growth Kinetics of Nanosize Silica in a Nonionic Water-in-Oil Microemulsion: A Reverse Micellar Pseudophase Reaction Model.' *Journal of colloid and interface science,* 218(1), 68-76.

Ozen, M., Mertens, M., Snikers, F., D'Hondt, H. & Cool, P. (2017). 'Molten-salt synthesis of tetragonal micron-sized barium titanate from a peroxo-hydroxide precursor.' *Advanced Powder Technology,* 28(1), 146-154.

Papan, J., Jovanović, D. J., Vuković, K., Smits, K., Đorđević, V. & Dramićanin, M. (2016). 'Europium(III)-doped $A_2Hf_2O_7$ (A= Y, Gd, Lu) nanoparticles: Influence of annealing temperature, europium(III) concentration and host cation on the luminescent properties.' *Optical Materials,* 61, 68-76.

Park, T.-J., Papaefthymiou, G. C., Moodenbaugh, A. R., Mao, Y. & Wong, S. S. (2005). 'Synthesis and characterization of submicron single-crystalline $Bi_2Fe_4O_9$ cubes.' *Journal of Materials Chemistry,* 15(21), 2099-2105.

Paul, B., Singh, K., Jaroń, T., Roy, A. & Chowdhury, A. (2016). 'Structural properties and the fluorite–pyrochlore phase transition in $La_2Zr_2O_7$: The role of oxygen to induce local disordered states.' *J. Alloys Compd.,* 686, 130-136.

Pechini, M. P. (1967). 'Method of Preparing Lead and Alkaline Earth Titanates and Niobates and Coating Method Using the Same to Form a Capacitor.' *US Patent No. 3330697*.

Phatak, R., Gupta, S. K., Maheshwari, P., Das, A. & Sali, S. K. (2017). 'Crystal structure of $Ba_2(La_{0.727}Ba_{0.182}M_{0.091})MO_6$ (M= Nb, Sb, Bi): symmetry nuance identified in photoluminescence and IR spectroscopy studies.' *Dalton Transactions,* 46, 1694-1703.

Phillips, M. C., Brumfield, B. E., LaHaye, N., Harilal, S. S., Hartig, K. C. & Jovanovic, I. (2017). 'Two-dimensional fluorescence spectroscopy of uranium isotopes in femtosecond laser ablation plumes.' *Scientific Reports,* 7, 3784.

Pileni, M. p., Motte, L. & Petit, C. (1992). 'Synthesis of cadmium sulfide in situ in reverse micelles: influence of the preparation modes on size, polydispersity, and photochemical reactions.' *Chemistry of Materials,* 4(2), 338-345.

Pokhrel, M., Burger, A., Groza, M. & Mao, Y. (20170. 'Enhance the photoluminescence and radioluminescence of $La_2Zr_2O_7$:Eu^{3+} core nanoparticles by coating with a thin Y_2O_3 shell.' *Optical Materials,* 68, 35-41.

Pokhrel, M., Wahid, K. & Mao, Y. (2016). 'Systematic studies on $RE_2Hf_2O_7$:5% Eu^{3+} (RE= Y, La, Pr, Gd, Er, and Lu) nanoparticles: effects of the A-site RE^{3+} cation and calcination on structure and photoluminescence.' *The Journal of Physical Chemistry C,* 120, 14828-14839.

Potdevin, A., Chadeyron, G., Briois, V., Leroux, F. & Mahiou, R. (2010). 'Modifications involved by acetylacetone in properties of sol–gel derived $Y_3Al_5O_{12}$:Tb^{3+} – II: optical features.' *Dalton Trans.,* 39, 8718-8724.

Purohit, R. D. & Tyagi, A. K. (2002). 'Auto-ignition synthesis of nanocrystalline $BaTi_4O_9$ powder.' *Journal of Materials Chemistry,* 12(2), 312-316.

Puska, M. J. & Nieminen, R. M. (1994). 'Theory of positrons in solids and on solid surfaces.' *Reviews of Modern Physics,* 66(3), 841.

Qi, Z., Cheng, X., Liu, B., Zhang, G., Chen, Y., Li, C. & Yin, M. (2011). 'Vibrational and dielectric properties of $La_2Hf_2O_7$: Experiment and theory.' *Solid State Communications,* 151, 1288-1292.

Ramesh, G., Subramanian, V. & Sivasubramanian, V. (2010). 'Dielectric properties of lead indium niobate ceramics synthesized by conventional solid state reaction method.' *Materials Research Bulletin,* 45(12), 1871-1874.

Reddy, M. V., Xu, Y., Rajarajan, V., Ouyang, T. & Chowdari, B. V. R. (2015). 'Template Free Facile Molten Synthesis and Energy Storage Studies on MCo_2O_4 (M = Mg, Mn) as Anode for Li-Ion Batteries ' *ACS Sustainable Chemistry and Engineering,* 3(12), 3035-3042.

Renju, U. A., Rao, P. P. & Thampi, D. S. V. (2017). 'Influence of phase transition from order to disorder and Philip's ionicity on the thermal expansion coefficient of pyrochlore type compositions with a multivalent environment.' *New Journal of Chemistry,* 41, 245-255.

Ricci, P. C., Carbonaro, C. M., Corpino, R., Cannas, C. & Salis, M. (2011). 'Optical and Structural Characterization of Terbium-Doped Y_2SiO_5 Phosphor Particles.' *J.Phys. Chem. C,* 115, 16630-16636.

Richardson, F. S. (1982). 'Terbium(III) and europium(III) ions as luminescent probes and stains for biomolecular systems.' *Chem. Rev.,* 82, 541-52.

Richardson, R. P. (2016). 'The thermoresponsive behaviour of selected rare-earth hafnate, zirconate, and titanate compounds.'

Rittman, D. R., Turner, K. M., Park, S., Fuentes, A. F., Park, C., Ewing, R. C. & Mao, W. L. (2017). 'Strain engineered pyrochlore at high pressure.' *Scientific reports,* 7, 2236.

Rojas-Hernandez, R. E., Rubio-Marcos, F., Gonçalves, R. H., Rodriguez, M. A. n., Véron, E., Allix, M., Bessada, C. & Fernandez, J. F. (2015). 'Original Synthetic Route To Obtain a $SrAl_2O_4$ Phosphor by the Molten Salt Method: Insights into the Reaction Mechanism and Enhancement of the Persistent Luminescence ' *Inorganic Chemistry,* 54(20), 9896-9907.

Sahu, M., Gupta, S. K., Jain, D., Saxena, M. & Kadam, R. (2018). 'Solid state speciation of uranium and its local structure in Sr_2CeO_4 using photoluminescence spectroscopy.' *Spectrochimica Acta Part A: Molecular and Biomolecular Spectroscopy,* 195, 113-119.

Scully, L. (2016). 'Cell-Diamond Anvil Almost Compresses Hydrogen to Metallic Phase.' *Machine Design*.

Shea, L., McKittrick, J. & Phillips, M. (1998). 'Predicting and modeling the low- voltage cathodoluminescent efficiency of oxide phosphors.' *J. Electrochem. Soc.,* 145(9), 3165-3170.

Shea, L. E., McKittrick, J., Lopez, O. A. & Sluzky, E. (1996). 'Synthesis of red- emitting, small particle size luminescent oxides using an optimized combustion process.' *J. Am. Chem. Soc.,* 79, 3257-3265.

Shinde, K. N., Dhoble, S. J., Swart, H. C. & Park, K. (2012). 'Methods of Measurements (Instrumentation).' *Phosphate Phosphors for Solid-Sate Lighting,* 174, 79-100.

Shu, X., Fan, L., Xie, Y., Zhu, W., Pan, S., Ding, Y., Chi, F., Wu, Y. & Lu, X. (2017). 'Alpha-particle irradiation effects on uranium-bearing $Gd_2Zr_2O_7$ ceramics for nuclear waste forms.' *Journal of the European Ceramic Society,* 37, 779-785.

Shu, X., Lu, X., Fan, L., Yang, R., Ding, Y., Pan, S., Zhou, P. & Wu, Y. (2016). 'Design and fabrication of $Gd_2Zr_2O_7$-based waste forms for U_3O_8 immobilization in high capacity.' *Journal of materials science,* 51, 5281-5289.

Siegel, R. W. (1980). 'Positron Annihilation Spectroscopy.' *Annual review of materials science,* 10, 393-425.

Singh, L. P., Singh, N. P. & Srivastava, S. K. (2015). 'Terbium doped SnO_2 nanoparticles as white emitters and SnO_2:5Tb/Fe_3O_4 magnetic luminescent nanohybrids for hyperthermia application and biocompatibility with HeLa cancer cells.' *Dalton Trans.,* 44, 6457-6465.

Singh, N. S., Sahu, N. K. & Bahadur, D. (2014). 'Multicolor tuning and white light emission from lanthanide doped $YPVO_4$ nanorods: energy transfer studies.' *J. Mater. Chem. C,* 2:3, 548-555.

Singh, S. K., Kumar, K. & Rai, S. B. (2009). 'Er^{3+}/Yb^{3+} codoped Gd_2O_3 nano-phosphor for optical thermometry.' *Sensors and Actuators A: Physical,* 149, 16-20.

Siqueira, K. P., Lima, P. P., Ferreira, R. A., Carlos, L. D., Bittar, E. M., Matinaga, F. M., Paniago, R., Krambrock, K., Moreira, R. L. & Dias, A. 2015. 'Influence of the matrix on the red emission in europium self-activated orthoceramics.' *The Journal of Physical Chemistry C,* 119, 17825-17835.

Sobczyk, M., Drożdżyński, J., Lisiecki, R. & Ryba-Romanowski, W. (2008). 'Near infrared and visible luminescence of U^{3+}-doped $PbCl_2$ single crystals.' *Journal of Luminescence,* 128, 185-189.

Stanek, C., Jiang, C., Uberuaga, B., Sickafus, K., Cleave, A. & Grimes, R. (2009). 'Predicted structure and stability of $A_4B_3O_{12}\delta$-phase compositions.' *Physical Review B,* 80, 174101.

Steudtner, R., Arnold, T., Großmann, K., Geipel, G. & Brendler, V. (2006). 'Luminescence spectrum of uranyl (V) in 2-propanol perchlorate solution.' *Inorganic Chemistry Communications,* 9, 939-941.

Subramanian, M., Aravamudan, G. & Rao, G. S. (1983). 'Oxide pyrochlores—a review.' *Prog. Solid State Chem.,* 15, 55-143.

Subramanian, M., Aravamudan, G. & Subbarao, G. (1983). 'Prog. Solid State.' *Chemistry, Ed. Rosenblatt and Worrell,* 15, 55.

Sun, M. & Huang, B. (2017). '"Energy Selection Channels" for High-Performance Electrolyte: Anion-Frenkel Defect Pair as Dominant Source for O Ion Conductions in Pyrochlore-type Lanthanide Hafnium Oxides SOFC.' *Inorganic Chemistry,* 56, 7975-7984.

Tong, S., Zhao, J. & Wen, X. (2016). 'Preparation and properties of Pr^{3+}/Ce^{3+}:YAG phosphors using triethanolamine as dispersant and pH regulator.' *Bull. Mater. Sci.,* 39, 1515-1519.

Trojan-Piegza, J., Gierlotka, S., Zych, E. & Lojkowski, W. (2014). 'Spectroscopic studies of nanopowder and nanoceramics $La_2Hf_2O_7$:Pr scintillator.' *J. Am. Ceram. Soc.,* 97, 1595-1601.

Turner, K. M., Rittman, D. R., Heymach, R. A., Tracy, C. L., Turner, M. L., Fuentes, A. F., Mao, W. L. & Ewing, R. C. (2017). 'Pressure-induced structural modifications of rare-earth hafnate pyrochlore.' *J. Phys.: Condens. Matter,* 29, 255401.

Van Uitert, L. (1967). 'Characterization of energy transfer interactions between rare earth ions.' *J. Electrochem. Soc.,* 114, 1048-1053.

Vecht, A., Gibbons, C., Davies, D., Jing, X., Marsh, P., Ireland, T., Silver, J., Newport, A. & Barber, D. (1999). 'Engineering phosphors for field emission displays.' *J. Vac. Sci. Technol., B,* 17, 750-757.

Wahid, K., Pokhrel, M. & Mao, Y. (2017). 'Structural, photoluminescence and radioluminescence properties of Eu^{3+} doped $La_2Hf_2O_7$ nanoparticles.' *Journal of Solid State Chemistry,* 245, 89-97.

Wang, C., Zhou, T., Jiang, J., Geng, H., Ning, Z., Lai, X., Bi, J. & Gao, D. (2017). 'Multicolor tunable luminescence based on Tb^{3+}/Eu^{3+} doping through a facile hydrothermal route.' *ACS applied materials & interfaces,* 9, 26184-26190.

Wang, G., Liu, Y., Ye, J., Qiu, W., Ma, S. & An, X. (2017). 'Fabrication of rod-like Ti_4O_7 with high conductivity by molten salt synthesis.' *Materials Letters,* 186, 361-363.

Wang, J., Ewing, R. C. & Becker, U. (2014). 'Defect formation energy in pyrochlore: the effect of crystal size.' *Materials Research Express,* 1, 035501.

Wang, W.-N., Widiyastuti, W., Lenggoro, I. W., Kim, T. O. & Okuyama, K. (2007). 'Photoluminescence optimization of luminescent nanocomposites fabricated by spray pyrolysis of a colloid-solution precursor.' *J. Electrochem. Soc.,* 154, J121-J28.

Wang, W.-N., Widiyastuti, W., Ogi, T., Lenggoro, I. W. & Okuyama, K. (2007). 'Correlations between crystallite/particle size and photoluminescence properties of submicrometer phosphors.' *Chemistry of Materials,* 19, 1723-1730.

Wang, Z., Li, P., Guo, Q. & Yang, Z. (2014). 'A single-phased warm white-light-emitting phosphor $BaMg_2(PO_4)_2$:Eu^{2+}, Mn^{2+}, Tb^{3+} for white light emitting diodes.' *Materials Research Bulletin,* 52, 30-36.

Wang, Z., Zhou, G., Zhang, J., Qin, X. & Wang, S. (2017). 'Luminescence properties of Eu^{3+}-doped Lanthanum gadolinium hafnates transparent ceramics.' *Optical Materials,* 71, 5-8.

Wang, Z., Zhu, H., Ai, L., Liu, X., Lv, M., Wang, L., Ma, Z. & Zhang, Z. (2016). 'Catalytic combustion of soot particulates over rare-earth substituted $Ln_2Sn_2O_7$ pyrochlores (Ln= La, Nd and Sm).' *J. Colloid Interface Sci. ,* 478, 209-216.

Whittle, K. R., Cranswick, L. M., Redfern, S. A., Swainson, I. P. & Lumpkin, G. R. (2009). 'Lanthanum pyrochlores and the effect of yttrium addition in the systems $La_{2-x}Y_xZr_2O_7$ and $La_{2-x}Y_xHf_2O_7$.' *Journal of Solid State Chemistry,* 182, 442-450.

Wilcoxon, J. P., Williamson, R. L. & Baughman, R. (1993). 'Optical properties of gold colloids formed in inverse micelles.' *The Journal of Chemical Physics,* 98(12), 9933.

Xiao, H. Y., Zhang, F., Gao, F., Lang, M., Ewing, R. C. & Weber, W. J. (2010). 'Zirconate pyrochlores under high pressure.' *Physical Chemistry Chemical Physics,* 12, 12472-12477.

Yanagida, T. & Okada, G. (2016). 'Characterizations of optical properties and radiation induced luminescence of Bi-doped $La_2Zr_2O_7$ transparent ceramics.' *Journal of the Ceramic Society of Japan,* 124, 564-568.

Yu, M., Wang, H., Lin, C., Li, G. & Lin, J. (2006). 'Sol–gel synthesis and photoluminescence properties of spherical SiO_2@LaPO4:Ce^{3+}/Tb^{3+} particles with a core–shell structure.' *Nanotechnology,* 17(13), 3245.

Yu, Y., Wang, S., Li, W. & Chen, Z. (2018). 'Low temperature synthesis of LaB_6 nanoparticles by a molten salt route ' *Powder Technology,* 323, 203-207.

Yuanbing Mao, Sarbajit Banerjee & Stanislaus S. Wong (2003). 'Large-scale synthesis of single-crystalline perovskite nanostructures.' *Journal of the American Chemical Society,* 125(51), 15718-15719.

Yuanbing Mao, J. P., John S. McCloy (2013). 'Magnetic properties of double perovskite oxide La2BMnO6 nanocrystals.' *Nanoscale,* 5,:11, 4720-4728.

Zhang, B., Dewasurendra, S. & Zhang, F. (2016). 'Blue and red up-conversion light emission in TM-doped $A_2B_2O_7$ oxides.' *Materials Letters,* 170, 53-57.

Zhang, F., Lang, M., Tracy, C., Ewing, R. C., Gregg, D. J. & Lumpkin, G. (2014). 'Incorporation of uranium in pyrochlore oxides and pressure-induced phase transitions.' *Journal of Solid State Chemistry,* 219, 49-54.

Zhang, K., Liu, H.-Z., Wu, Y.-T. & Hu, W.-B. (2008). 'Co-precipitation synthesis and luminescence behavior of Ce-doped yttrium aluminum garnet (YAG: Ce) phosphor: The effect of precipitant.' *Journal of Alloys and Compounds,* 453, 265-270.

Zhang, Y., Kong, L., Aughterson, R. D., Karatchevtseva, I. & Zheng, R. (2017). 'Phase evolution from $Ln_2Ti_2O_7$ (Ln= Y and Gd) pyrochlores to brannerites in glass with uranium incorporation.' *Journal of the American Ceramic Society,* 100, 5335-5346.

Zhang, Y., Xu, J., Cui, Q. & Yang, B. (2017). 'Eu^{3+}-doped $Bi_4Si_3O_{12}$ red phosphor for solid state lighting: microwave synthesis, characterization, photoluminescence properties and thermal quenching mechanisms.' *Sci. Rep.,* 7, 42464.

Zheng, K., Liu, Z., Lv, C. & Qin, W. (2013). 'Temperature sensor based on the UV upconversion luminescence of Gd^{3+} in Yb^{3+}–Tm^{3+}–Gd^{3+} codoped $NaLuF_4$ microcrystals.' *Journal of Materials Chemistry C,* 1, 5502-5507.

Zhong, F., Zhao, J., Shi, L., Xiao, Y., Cai, G., Zheng, Y. & Long, J. (2017). 'Alkaline-Earth Metals-Doped Pyrochlore $Gd_2Zr_2O_7$ as Oxygen Conductors for Improved NO_2 Sensing Performance.' *Scientific Reports*, 7, 4684.

Zhou, H., Mao, Y. & Wong, S. S. (2007). 'Probing structure-parameter correlations in the molten synthesis of $BaZrO_3$ perovskite submicron-sized particles.' *Chemistry of Materials*, 19(22), 5238-5249.

Zhou, S., Jiang, S., Wei, X., Chen, Y., Duan, C. & Yin, M. (2014). 'Optical thermometry based on upconversion luminescence in Yb^{3+}/Ho^{3+} co-doped $NaLuF_4$.' *Journal of Alloys and Compounds*, 588, 654-657.

Zhou, Y., Han, S. T., Chen, X., Wang, F., Tang, Y. B. & Roy, V. A. L. (2014). 'An upconverted photonic nonvolatile memory.' *Nature Communications*, 5.

Zuniga, J. P., Gupta, S. K., Abdou, M. & Mao, Y. (2018). 'Effect of molten salt synthesis processing duration on the photo- and radioluminescence of UV-, Visible-, and X-ray-excitable $La_2Hf_2O_7:Eu^{3+}$ nanoparticles.' *ACS Omega*, 3, 7757-7770.

Zuniga, J. P., Gupta, S. K., Pokhrel, M. & Mao, Y. (2018). 'Exploring optical properties of $La_2Hf_2O_7:Pr^{3+}$ nanoparticles under UV and X-ray excitations for potential lighting and scintillating applications ' *New Journal of Chemistry*, 42(12), 9381-9392.

Zuniga, J. P., Abdou, M., Gupta, S.K. & Mao, Y. (2018). 'Molten-Salt Synthesis of Complex Metal Oxide Nanoparticles' *Journal of Visualized Experiments*, 140, e58482.

BIOGRAPHICAL SKETCH

Mr. Jose P. Zuniga was born in 1994 in Matamoros, Mexico. He received his BS (June 2017) in chemistry from the University of Texas Rio Grande Valley. Currently, he obtain his MS in chemistry (May 2019) and is planning to pursue a PhD degree in Chemistry at Iowa State University under Dr. Javier Vela. He is a raising scientist, early in his career with multiple publications in Peer review Journals and several awards from J. Lell Elliot, Welch's Foundation, USDA, and HSF. Recently, he has been awarded the Hispanic Scholarship Fund and was named one of the brightest Latino students in the country (USA). He has worked as a user scientist at the Center for Nanophase Material Science at Oak Ridge National Laboratory. His focus in research involves nano-phosphor engineering for radiation detection, nuclear waste immobilization, lighting applications, scintillator applications and nano-material with up-conversion properties for water disinfection and bio-imaging.

Jose P. Zuniga

Master of Science in Chemistry

josezuniga6@gmail.com

P.O. Box 793

Pharr, TX, 78577